SCUOLA DI SCIENZE

Dipartimento di Chimica Industriale "Toso Montanari"

Corso di Laurea Magistrale in

Chimica Industriale

Curriculum: Advanced Spectroscopy in Chemistry

Classe LM-71 - Scienze e Tecnologie per la Chimica Industriale

Synthesis and Characterization of Double Metal Hexacyanoferrates

Candidate:

Mariam Maisuradze

Supervisor:

Professor Marco Giorgetti

Co-supervisor:

Dr. Dino Tonti

Min Li

Session I

Academic Year 2019 - 2020

Table of contents

Abstract

Manganese Hexacyanoferrate (MnHCF) and nickel doped manganese hexacyanoferrate were synthesized by simple co-precipitation method. The water content and chemical formula was obtained by TGA and MP-AES measurements, functional groups by FT-IR analysis, the crystal structure by PXRD and a local geometry by XAS. Elemental species of cycled samples were further investigated by TXM and 2D XRF. Electrochemical tests were performed in the glass cell. With addition of nickel, vacancies and water content increased in the sample. Crystal structure changed from monoclinic to cubic. Ni disturbed the local structure of Mn, site, however, almost no change was observed in Fe site.

After charge/discharge cycling of MnHCF intercalation was already found in the peripheries of charged species after 20 cycle in 2D XRF analysis and randomly distributed intercalated regions after 50 cycles in TXM analysis.

Cyclic voltammetry showed that peak-to-peak separation is increasing in case of the addition of Ni to MnHCF.

Introduction

World population is rising, technological progress is advancing and reaching almost every part of the earth and consequently, energy consumption is increasing rapidly. Searching and trying to implement the new sources of energy is not a new topic, but with time the environmental impact got more and more significant, endanger not only the nature, but possibly affecting human health. People start to think about the avoidance of the harmful effects on environment and, generally, about maintenance of the sustainable future.

The studies about energy production and its storage is very complicated and delicate topic. Many scientists and large scale companies are working in the research field about the alternative energy sources, such as solar or wind energy. But quite often this type of sources have seasonal character and for their effective use, they should be coupled with the efficient energy storage devices.

Another step towards the sustainability is quite often considered to be the substitution of the conventional fuel in the light vehicles, such as in cars, with electricity. Here again, the powerful energy storage devices are needed for the large distance coverage without necessity of interruption for recharging. But also, limited dimensions must be considered as a necessary criteria before the actual implementation in the everyday life.

It also worth to mention, that nowadays, almost everyone has some kind of the portable device, such as laptop, cellular phone, tablet, camera and so on. Each of them are able to work, because they are equipped with small size, but powerful energy storage device (quite often Li-ion or Li-polymer batteries). But people still want to be able to use their belongings for longer without the necessity for recharging, for them to have a higher maintenance time, of course to be safe and at the same time, to be affordable. Because of all that, this field is growing rapidly, however, not without problems, which are essential to be solved and the new discoveries are necessary to be made for its further progress in the future.

Batteries have a long history of development. But one of the most important recent invention is lithium-ion battery. In 2019 Nobel Prize in Chemistry are awarded to John Goodenough, M. Stanley Whittingham and Akira Yoshino “for the development of lithium-ion batteries”. As the official website of Nobel Prize writes: “They created a rechargeable world. Through their work, they have created the right conditions for a wireless and fossil fuel-free society, and so brought the greatest benefit to humankind.” [1]

I. Literature review

1. Battery materials

1.1. Lithium-ion Batteries (LIBs)

Lithium-ion batteries (LIBs), compared with other commonly used batteries, are have high energy density, high power density, long service life and environmental friendliness. These features have led to its usage in wide range of application [2], not only in power portable devices including cellular phones, notebooks, video and digital cameras and so on, but also large-scale lithium-ion batteries have been considered as one of the most promising power sources for electric vehicles (EVs) and stationary power sources for storing wind and solar energy [3, 4]. Lithium is the most electropositive metals with the standard potential of -3.045 vs. SHE. The first published interest about lithium batteries was the work of Harris in 1958 [5]. Eventually, it led to the development and commercialization of a variety of primary lithium cells during the 1970s. The more prominent systems were lithium/sulfurdioxide Li/SO_2, lithium-thionylchloride $Li/SOCl_2$, lithium-sulfurylchloride Li/SO_2Cl_2, lithium-polycarbon monofluoride $Li/(CF_x)_n$ lithium-manganese dioxide Li/MnO_2 and lithium-iodine $Li/(poly\text{-}2\text{-}vynil\ pyridine)I_n$.

In the 1980s scientists had difficulties recharging the metallic lithium anode. Occasionally unfortunate events about safety were occurring, such as flame. It was often caused at first by the reactivity of metallic lithium, especially electrodeposited one with electrolyte solutions and later, when Li metal was not involved, by the flammable organic solvents. Lithium electrode reactions were studied, including different strategies about the improvement of its utility and safety by the modification of the reactivity of the Li-solution interface [6]. Fast ion conduction studies in solids demonstrated (acting as a host) that alkali metal ions could move rapidly in an electronically conducting lattice containing transition metal atoms in a mixed valence state. When the structure of the host is fully lithiated (populated with lithium ions), the transition metal atom is in the reduced state. When lithium ions are removed from the host, the transition metal and host structure is oxidized. . This is the principle of the ion technology, such as Li-ion of Na-ion. Good candidate of a host structure for an electrode is a mixed ionic-electronic conductor, which does not change the structure over a large range of the solid solution upon the removal of lithium; also the lithiated (reduced) structure and partially lithiated (partially oxidized) should have suitable potential difference versus lithium; the host lattice dimension should not changes too much with the insertion/removal of lithium and its operational voltage range be compatible with the redox range of stability for the electrolyte.

Lithium insertion compounds as positive electrodes were used during the late 1970s and 1980s. The first cells of this type appeared when Exxon tried to commercialize Li/TiS_2 and Moli Energy – the Li/MoS_2 system. These systems were operating near 2 volts, which is quite low voltage. Whittingham, in his early research [7], reviewed the properties and preparation of many insertion compounds and discussed the intercalation reaction. Some of them were implemented in batteries, such as V_2O_5, V_6O_{13} and MnO_2. All of these systems continued to use metallic lithium anodes and because of the safety problems, it had limited use in the commercial application.

Afterwards Steele suggested graphite and the layered sulfide as potential candidates for electrodes of a lithium-ion battery based on a non-aqueous liquid electrolyte [8]. Next candidates became transition metal chalcogenides: Li_xMO_2 (where M = Ni, Co, or Mn) [9, 10]. These materials are the starting point for the most commonly used cathodes in commercial lithium-ion cells. Lithium-ion cell was working with two insertion electrodes cycling lithium ions between them, without the usage of a metallic lithium anode [11, 12].

Next development was battery system, where the insertion and removal of lithium ions into host compounds was occurring through both electrodes. Eventually, in 1991, Sony introduced the first commercial lithium-ion cell based on carbon anode and a $LiCoO_2$ cathode [13].

Since its commercialization, the energy density of LIBs has continuously increased by about 7–8 $Wh\,kg^{-1}$ per year, and cell costs decreased much faster than expected from around 1000 $€\,kWh^{-1}$ (mid 1990s) to below 200 $€\,kWh^{-1}$ (2017) [14].

Despite the remarkable performance of organic-electrolite systems, they suffer from the use of highly toxic and flammable solvents, which can be dangerous during overcharging or short-circuiting. Also, nonaqueous electrolytes generally have two orders of magnitude lower ion conductivities than aqueous electrolytes. In addition, fabrication costs of organic electrolytes are high. The aqueous lithium-ion battery was first developed by Sony Dahn's group in 1994 [15]. VO_2 was used as a negative electrode and $LiMn_2O_4$ as a positive electrode in 5 M $LiNO_3$ solution.

However, LIBs have some limitations. One of the main issues is resource problem related to the abundance and geographical distribution of lithium.

1.2. Sodium-Ion Batteries

At present, rechargeable batteries composed of sodium, potassium, magnesium and aluminum are gaining attention as potentially less toxic and more economical alternatives to lithium-ion batteries. However, replacing Li-ions with Na-, K-, Mg-, or Al-ions requires deep revision and re-exploration of the cathode and electrolyte materials and electrochemistry of such batteries [16].

One of the main reasons why SIBs are perspective is based on the wide availability and low cost of sodium, which is the 4th most abundant element in the Earth crust.

SIBs have the most similarities with LIBs in terms of their typical electrode materials and electrolyte formulations. However, despite their position in the periodic table, the electrochemistry of Na- and Li-ions are often very different. There are fundamental differences, for example, the mass of Na is ~3x larger, it has 0.3 Å larger ionic radius than Li and various thermodynamic parameters, which lead to ~300 mV higher standard reduction potential of Na. Sodium is less reducing than lithium: –2.71V compared to –3.04 V and the gravimetric capacity is lower: 1165 mAh g^{-1} compared to 3829 mAh g^{-1}. Consequently, hosts must possess channels and interstitial sites large-enough to accept the larger Na^+ cation [17]. Nevertheless, new efficient Na-ion cathode materials have been successfully developed, such as $Na_{1.5}VPO_{4.8}F_{0.7}$ [18] and $Na_4Co_3(PO_4)_2P_2O_7$ [19], which show electrochemical performance comparable with Li-ion cathodes. The issue with the development of high-performance anode materials also exists. Similar to metallic Li, the use of elemental Na as an anode is not possible because of Na dendrite formation. Graphite, which is used as an anode material for LIBs, shows negligible capacities of 30–35 mA h g^{-1} for Na-ion storage [20]. Other carbonaceous materials such as hard carbon exhibit capacities of less than 300 mA h g^{-1}. Alloying-type anodes composed of elements such as tin (Sn), antimony (Sb), or phosphorus (P) have also been studied [21, 22, 23]. However, such anodes often suffer from poor cycling stability because of their massive volume changes upon discharge/charge (alloying/dealloying), which leads to rapid mechanical deterioration of the electrodes. Some anode materials, which show high capacities, suffer from relatively high desodiation voltages, some anodes have issues in terms of safety. For instance, P offers a high specific capacity and relatively low desodiation potential, making it a compelling anode material, but in the charged state, P is converted into Na_3P, which reacts with water in the case of cell breakage forming highly toxic and flammable PH_3 [16].

1.3. Cathode Materials For Aqueous Batteries

When choosing of electrode active material for aqueous lithium-ion batteries it must be considered that stable potential window of the aqueous electrolyte is narrow (**Error! Reference source not found.**).

The electrodes with an intercalation potential between 3 and 4 V before oxygen evolution can be used as cathode materials for aqueous lithium-ion batteries. For example $LiCoO_2$, $LiMn_2O_4$, $LiNi_xCo_{1-x}O_2$, $LiFePO_4$. Therefore, for anode material intercalation potential between about 2∼3 V regarding the working voltage and the hydrogen evolution reaction [4].

As for SIBs, perspective cathode materials are:

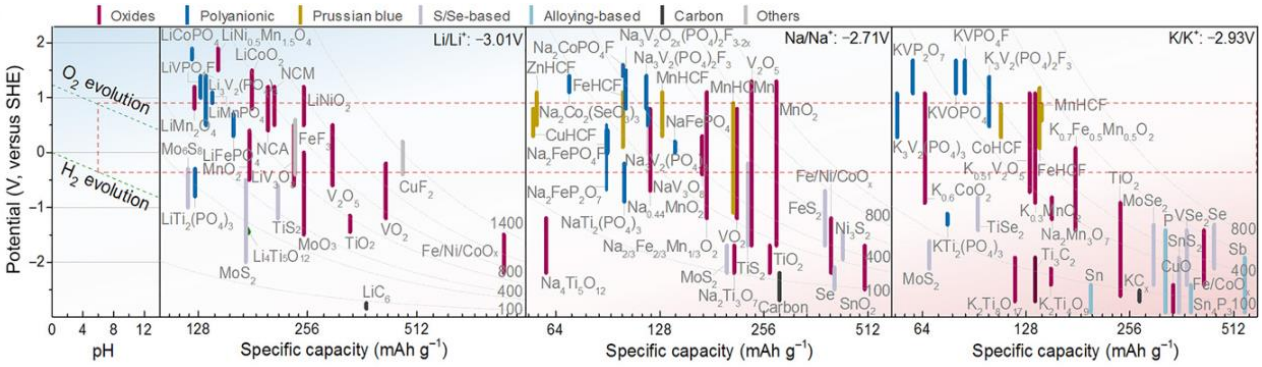

Figure 1. Comparison of Reported Cathode Materials for Lithium, Sodium and Potassium Ion Batteries [24]

Figure shows the summary of narrow electrochemical stability window of water and redox potentials of various electrode materials in organic LIBs, NIBs, and KIBs. Water has thermodynamic oxidation potential [oxygen evolution reaction (OER)] and reduction potential [hydrogen evolution reaction (HER)], which differ by a narrow voltage window of 1.23 V. On the left side O_2/H_2 evolution potential versus normal hydrogen electrode (NHE) for different pH is shown; ion intercalation potential of various electrode materials versus NHE and Li/Li^+, Na/Na^+, K/K^+ is shown the right side of the image.

1.4. Prussian Blue (PB) and Prussian Blue Analogs (PBA)

Prussian Blue (PB) and its analogs (PBAs) are large family of transition metal hexacyanoferrates. They have face centered cubic structures. Space group is *Fm3-m*, general formula $A_xM[Fe(CN)_6]_\gamma\square_{1-\gamma}\cdot zH_2O$, where A is an alkali metal such as Li^+, Na^+, K^+, etc.; M is transition metal ions: Fe, Co, Mn, Ni, Cu etc.; □ is a vacancy; $0<x<2$; $0<y<1$ [25]. Generally, vacancies will be generated due to the excessive growth of PBA crystals when compared with the nucleation process [26].

In a cubic lattice, the M^{2+} ions are sixfold coordinated to the nitrogen atoms of the CN ligands, and Fe ions are octahedrally neighbored with the carbon atoms of the CN ligands, forming a 3D rigid framework containing open ionic channels, about 3.2 Å diameter in ⟨100⟩ and spacious interstitial spaces, around 4.6Å in diameter [27], which leads to the higher diffusion coefficient of 10^{-9} to 10^{-8} cm^2s^{-1} [28, 29] and consequently much higher ionic conduction than in the conventional insertion cathodes of oxides and phosphates [25].

PBAs have open framework structure, redox-active sites and strong structural stability [30]. Because of large ionic sites, they can reversible accommodate and easily transport large cations such as Na^+ and K^+. Generally, both redox centers $M^{+2/+3}$ and $Fe^{+2/+3}$, of PBs should be electroactive (it has to be proven experimentally by techniques such as XAS), which means two electron redox capacity and consequently two sodium ion storage per molecular unit [25].

In addition of variety of M metals, Fe can be partially or fully substituted by Co, Ni, Mn, Cu Zn and etc. Substitution with redox-active transition metals does not damage the crystal structure [31, 32]. This makes PBAs electrochemically tunable cathode materials. It also worth to mention, that PBA lattice, due to its robust and large 3D channel frameworks, is structurally and dimensionally stable, with almost zero lattice strain [33] towards the insertion and extraction processes [25].

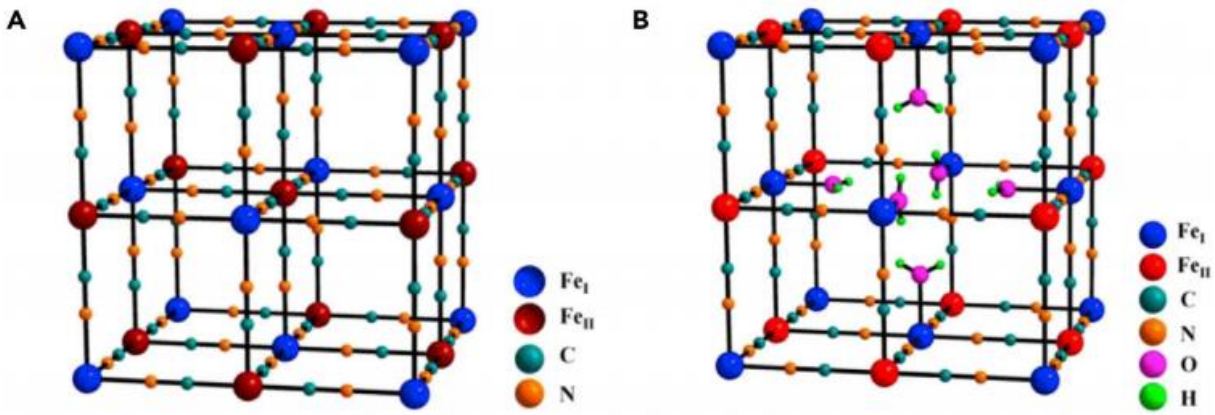

Figure 2. Schematic Diagram of Unit Cell: Unit cell of (A) perfect PB and (B) PB with coordinated water [34]

Although M and Fe or the metal which is substituting the iron can be the same element, often they are distinguishable according to their valence states: the intrinsic difference between them is their spin states determined by the strength of ligands around the central ion. High-spin (HS) M is located in MN_6 octahedra and low-spin (LS) metal located in MC_6. These two kinds of octahedra are interconnected by C≡N bridges, forming a cubic open framework. On the basis of precursors and preparation conditions, there can be a variety of combination of valence states of these two transition metals *[26]*.

Table 1. Typical Crystal Structures and Space Groups of PBAs (HCF=Hexacyanoferrate = $Fe(CN)_6$)

	MnHCF	FeHCF	CoHCF	NiHCF	CuHCF	ZnHCF
Cubic ($Fm\bar{3}m$)	✓	✓	✓	✓	✓	✓
Rhombohedral ($R\bar{3}$, $R\bar{3}c$)	✓	✓	✓	✓		✓
Monoclinic ($P21/n$)	✓	✓				

Among simple PBAs, manganese hexacyanoferrate has a high specific capacity and redox plateaus at high voltage. However, its severe crystal Jahn-Teller distortion effect, which affects the longterm cycling capability. Replacing potassium in $KMn[Fe(CN)_6]$ by sodium greatly improved the sodium storage capacity, which reached 134 mAh g^{-1} [35]. Interstitial H_2O can be removed either thermally or electrochemically, which induced a structural transition inside the MnHCF framework from monoclinic to rhombohedral, with improved electrochemical performances [36].

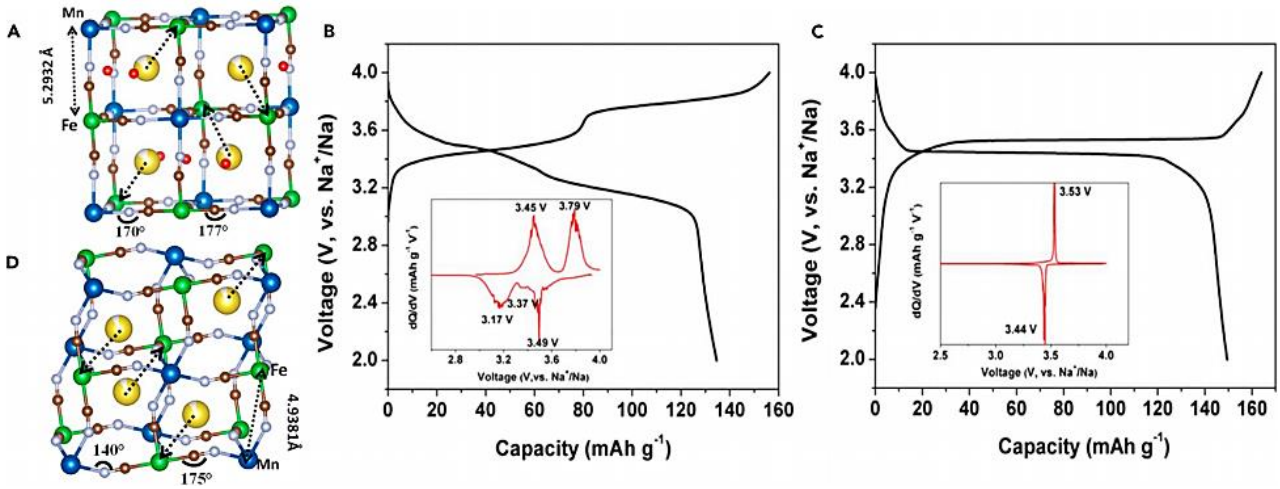

Figure 3. Local structures of M-Na_2-dMnHCF (A) and R-Na_2-dMnHCF (D). Initial charge and discharge profiles of M-Na_2-dMnHCF (B) and R-Na_2-dMnHCF (D) at 0.1 C [36].

The content of coordinated and zeolitic water in the as-prepared material causes volume changes between the sodiated and desodiated phases may as well, which also contribute to capacity degradation [37].

The properties of PBAs can be changed by heteroatom doping or partial substitution of the high spin ions in MN_6 octahedra (M = Mn, Fe, Co, Ni), which provides an additional degree of freedom for the adjustment of the electrochemical properties. For this purpose, nickel is used quite often to promote PBAs' [38]. Nickel doping can activate C-coordinated Fe ions (Fe^{LS}) and facilitate Na+ diffusion within the lattice.

Nickel was also one of the elements used to relax the Jahn-Teller distortion in MnHCF [39, 40]. The atomic radius of Mn is almost equal to the atomic radius of Ni, so, when the Ni element replaces the Mn element in the Prussian blue structure, the cubic framework remains in the good order, but from the literature it is known that, during insertion/extraction of Na^+, the Ni sites are unreactive and they are just balancing the tiny structural disturbances caused by the redox reactions of Mn sites [41].

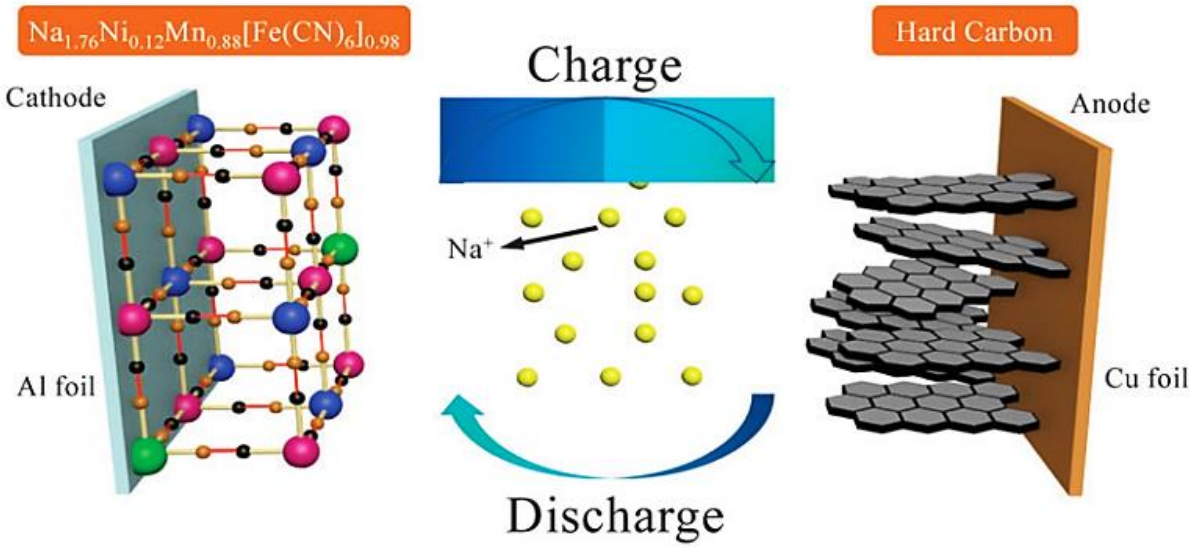

Figure 4. The scheme of advanced sodium ion battery, cathode material $Na_{1.76}Ni_{0.12}Mn_{0.88}[Fe(CN)_6]_{0.98}$ [41]

2. Characterization Techniques

2.1. Synchrotron Facility: “Elettra”

Synchrotron radiation is produced when electrons travelling at relativistic speeds are deflected in magnetic fields. The storage ring is made up of four types of magnets: bending magnets that deflect the circulating electron beam into a closed circular path, quadrupoles that focus the beam, sextupoles that compensate chromatic and non-linear effects and steerer magnets that perform small adjustments to the circular trajectory. Insertion devices are of many types (electromagnets or permanent magnets) and depending on the magnetic configuration can be made to produce linear to circular polarised light. The wavelength of the light is tuneable by changing the magnetic field acting on the electron beam [42].

This injection chain consists of a 100 MeV linear accelerator and a 2.5 GeV booster that sends the beam into the storage ring at a rate of up to 3 Hz.

The electrons are generated in a small linac. They start off from a ceramic disc which is heated to very high temperature. An electric field of up to 100 kV draws out the electrons that are then accelerated through two radio-frequency structures that make up the linac. The linac is composed of the Gun (that houses the ceramic disc), a low energy bunching section and two high-energy sections. The overall length of the linac is 12 m and contains two high-energy sections each 5m long. Between accelerating sections quadrupole magnets keep the beam focused. The linac operates at 3 GHz and generates a pulse of electron bunches that are accelerated to the final energy of 100 MeV. In order not to lose electrons as they are accelerated the entire linac is under vacuum, as is the transfer lines the booster and storage ring. In this way collisions with gas molecules, that would otherwise cause the loss of electrons, are avoided.

The electrons exiting the linac are then transported to the booster by a transfer line (a series of deflection and focussing magnets). The booster is a simple synchrotron of 118 m of circumference that can accelerate a maximum of 6 mA current from 100 MeV up to 2.5 GeV with a repetition rate of 3 Hz. It operates always at full cycle (100 MeV to 2.5 GeV) and the electrons are extracted at the needed energy by adjusting the extraction kicker time. The booster is using the on-axis injection scheme therefore cannot accumulate. Once the electrons arrive at the requested energy are extracted to a long transfer line that arrives to the storage ring.

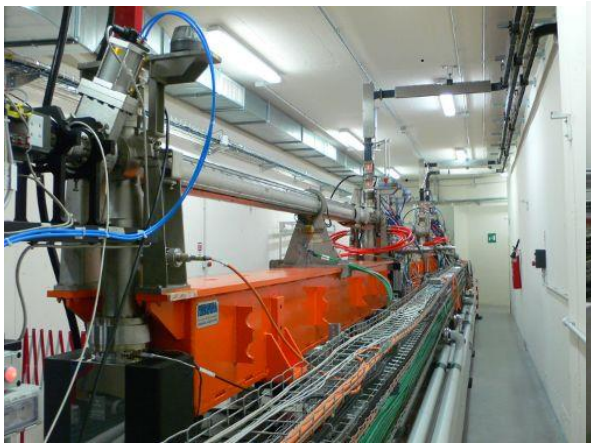

Figure 5. The small Linac

Figure 6. Part of the Booster

The storage ring is filled by a multi-turn injection process by pulses of electrons from the booster. Electrons are gradually fed into the ring three times a second until the desired current is achieved using special magnets. The maximum intensity is limited by the thermal load in the vacuum chamber due to synchrotron radiation and the radiofrequency power. The electrons circulating in the ring in a metal vacuum chamber. The vacuum that is maintained in the ring must be of very high quality, since electrons are travelling close to the speed of light, traverse a given point more than a million times in one second. To maintain a long beam lifetime we must therefore reduce the chance of electrons colliding with gas molecules. The unused radiation must be absorbed in special places otherwise chamber deformation and photo-electron release of surface gasses will occur. The beam is strongly focused by the ring quadrupoles, the bending magnets have a gradient to provide additional focusing. Sextupole magnets, placed at points in the ring where electrons with different energies are used to compensate unwanted chromatic effect. The energy lost by the electrons when emitting synchrotron radiation is compensated by radio-frequency cavities. Electron bunches are separated by 2 ns. The lifetime is essentially determined by the quality of the vacuum and the quality of the emittance.

All systems are controlled from the Elettra control room, whereas the equipments are in special service areas [43].

The storage ring beam current at 2 GeV is set by the users to 310 mA and top-up occurs every 6 min by injecting 1 mA in 4 seconds, keeping thus the current level constant to 3‰. At 2.4 GeV

the stored beam current is set to 140 mA, top-up occurs every 20 minutes injecting 1 mA in 4 seconds keeping the current level constant to 7‰ [44].

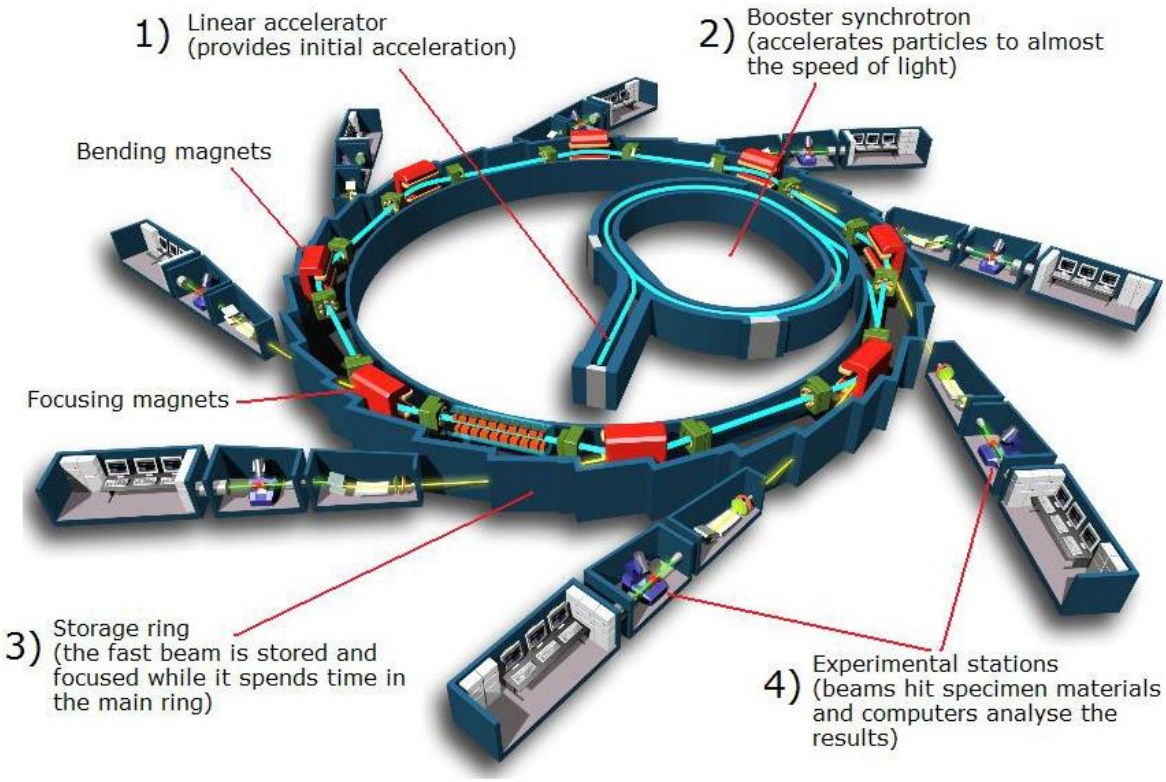

Figure 7. General scheme of synchrotron facility [45]

Important techniques, which are conducted in the synchrotron facilities are spectroscopic techniques, such as soft or hard X-ray absorption spectroscopy, X-ray fluorescence Spectroscopy, sometimes infrared spectroscopy… Also imaging techniques, microscopy, X-ray diffraction. There can be done not only experiments with high accuracy and high resolution, but conduct in situ and operando studies, which can be really useful in several different study fields, such as batteries, heterogeneous catalysis and etc.

2.1.1. X-ray Absorption Spectroscopy (XAS)

The two interactions are possible between electromagnetic radiation below 1 MeV and matter: photoelectric absorption and scattering, giving origin to three basic groups of experimental techniques: spectroscopy, diffraction and imaging. Spectroscopy is due to the absorption mechanism, and gives mainly information on the electronic structure of matter.

X-ray absorption spectroscopy (XAS) the absorption of X-rays is studied as a function of energy. X-ray energies used in XAS are from about 1 keV to about 100 keV, corresponding to wavelengths from about 0.12 to about 12 Å, respectively. In this energy range, the dominant attenuation mechanism is photoelectric absorption. When the energy of the absorbed X-ray photons increases, the absorption coefficient $\mu(\omega)$ progressively decreases (harder X-rays are more penetrating); the absorption also depends on the atomic species - heavier atoms are more absorbing. The absorption edges originate when the photon energy becomes high enough to extract an electron from a deeper level, they are labelled by the consecutive alphabetical letters K, L, M ..., which correspond to the principal quantum numbers 1, 2, 3, ..., respectively. The energy of absorption edges increases monotonically with the atomic number Z.

In correspondence of an edge, the absorption coefficient exhibits fine structure, so-called X-ray Absorption Fine Structure (XAFS). For isolated atoms the XAFS is limited to a few eV around the edge, and reflects the transitions of the core electron to unoccupied bound levels (Rydberg levels). In molecular gases and condensed systems, the XAFS, strongly influenced by the presence of the atoms surrounding the absorber one, can extend up to and beyond one thousand eV above the edge.

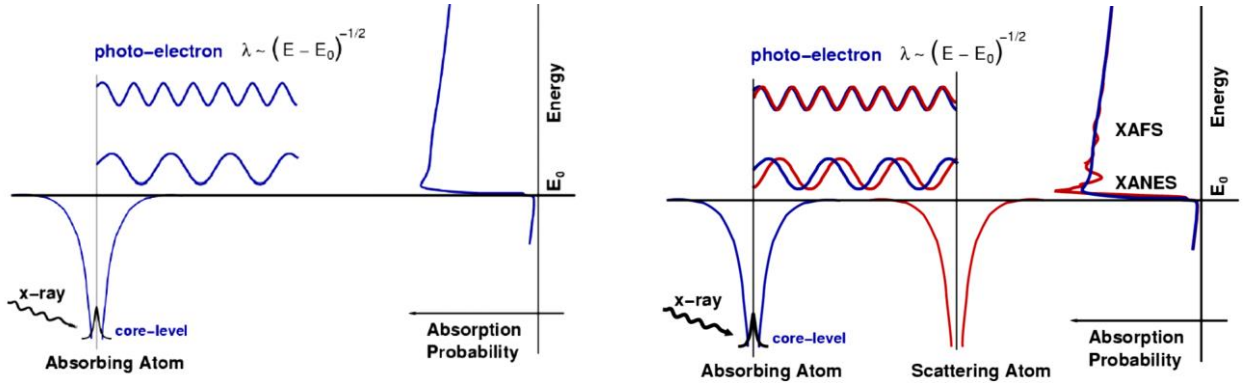

Figure 8. X-ray absorption spectra for isolated absorbing atom (left) and coordinated absorbing atom (right) [46]

XAFS is customarily divided into two regions: the structure within 30 - 50 eV above the edge, which is called XANES (X-ray Absorption Near Edge Structure) or NEXAFS (Near Edge X-ray Absorption Fine Structure) and the fine structure extending from the XANES region to up to typically one thousand eV, which is called EXAFS (Extended X-ray Absorption Fine Structure). From the XANES information about the local electronic and geometric structure can be obtained.

Sometimes, the structure within a few eV around the edge are distinguished as pre-edge structure and edge structure; EXAFS carries information on the local geometric structure surrounding a given atomic species [47].

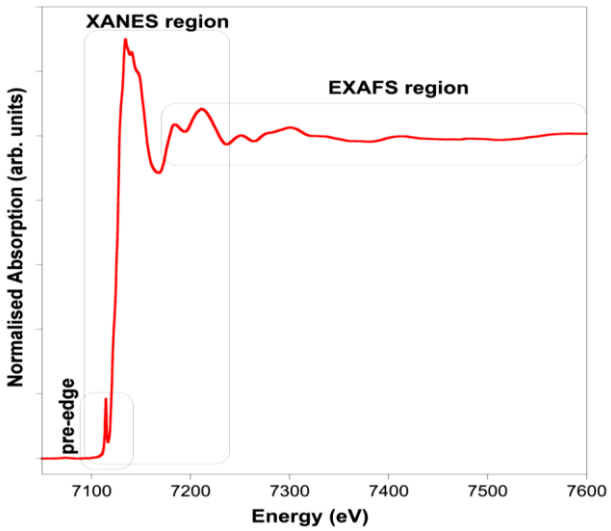

Figure 9. General scheme of X-ray absorption spectrum [46]

In XANES part of the spectra information about electronic transitions and photo-electron multiple scattering can be retrieved. Some the conclusions can be made by investigation of the pre-edge region of XAS spectrum. It arises from transitions of electrons to bound excited electronic states, which are strongly modulated by the surrounding atoms in the short and medium range environment. From the pre-edge region, based on the peak energy versus height information about coordination number, can be obtained. For example, in case of pure octahedron in transition metals, because of centro symmetry p-d mixing is not allowed, only weak quadrupolar transitions occur, so no, or very low intensity peak in the pre-edge region is observed. If octahedron is distorted, it means that centro symmetry is broken: p-d mixing is allowed, dipole transition occur in the edge and moderate intensity pre-peak is generated. In tetrahedron there is no centro symmetry and high intensity peak in the pre-edge is observed [48]. From pre-edge the estimation of the distortion is also possible using the intensity ratio between pre-edge peaks.

XANES spectra can described as a “digit fingerprint” of the chemical environment surrounding the photo-absorber atom. The emitted photo-electron has low energy. It is possible to obtain: the information about the oxidation state of the element. With the increase of the oxidation state, chemical shifts are observed towards the higher energy.

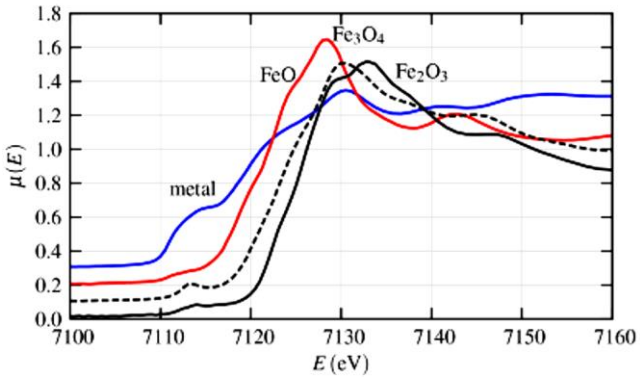

Figure 10. XANES spectra of Fe edge in different oxidation states [46]

EXAFS contains the information about photo-electron single scattering and multiple scattering. Much can be understood from the analysis of EXAFS spectra about the surrounding of the absorbing atom, about 10Å, which means a few coordination shells. For each coordination shell, can be obtained: the average inter-atomic distance ⟨ r ⟩; the coordination number N, and Debye-Waller parameter σ^2 that measures the degree of thermal and structural disorder [47]. The amplitude of the EXAFS signal depends on the number and nature of the first neighbors, the phase on the other hand, depends on distance between the photoabsorber and scatterer. The EXAS equation was first introduced by Lytle, Sayers, Stern in 1970 [49] for a Single Scattering (SS) event, one electron approximation, and by considering a plane wave.

$$\chi(k) = \sum_{j-1}^{shells} \frac{N_j}{kR_j^2} \cdot F_j(k) \cdot S_0^2 \cdot e^{-2R_j/\lambda(k)} \cdot e^{-2\sigma_j^2 k^2} \cdot \sin\left[2kR_j + \varphi_j(k)\right]$$

Where, *Nj* is number of *j*-atom neighbors; *Rj* - distance; *Fj(k)* - backscattering amplitude; *φj(k)* - phase shift due to central and scatterer atom; *σj* - Debye-Waller like factor, which shows structural and thermal disorder and *λ(k)* - photoelectron mean free path.

Atoms in condensed matter vibrates around their equilibrium position depending on temperature. And this displacements reduce the EXAFS amplitude. It is damped by a Debye Waller Factor: $e^{-2\sigma_j^2 k^2}$. The EXAFS Debye-Waller Factor is therefore the mean square average of the difference of the displacement of the backscatterer relative to the displacement of the absorber:

$$\sigma_j^2 = \langle \left[r_j (u_j - u_0) \right]^2 \rangle$$

For interpreting EXAFS, it is necessary to consider several approximations. Key approximations are: plane wave approximation, K threshold, single scattering, one electron approximation, "sudden" approximation and electric dipole approximation. The EXAFS takes place on a time scale much shorter than that of atomic motion including vibrations, which means that the measurement is a sum of instantaneous spectra of the atomic configuration [46].

2.1.2. X-ray diffraction (XRD)

The diffraction technique originates from the discovery of William Lawrence and William Henry Bragg in 1912 [50]. A crystalline material generates unique patterns of diffracted X-ray, distributed according to Bragg's law: Bragg peaks are observed when the scattered X-ray beams constructively interfere. Bragg's law can be described by the equation.

$$2d \sin \theta = n\lambda$$

Where d is the inter-planar distance, θ is the scattering angle, n is an integer, and λ is the wavelength of the incident X-ray.

Irradiated X-rays are scattered by the electrons surrounding an atom. At low 2θ angles, the scattering factor for an atom is nearly proportional to the number of electrons, which means that light atoms are weak and heavy atoms are strong X-ray scatterers. On the other hand, at high 2θ angles, rapid decrease of scattering factor is observed, because of the partial interference of X-rays away from the incident angle of the beam. This leads to a general decrease over the Bragg peak intensity [51].

Powder X-ray diffraction (XRD) is a common material characterization technique. It provides important information that is complementary to various microscopic and spectroscopic methods, such as phase identification, sample purity, crystallite size, and, in some cases, morphology [52]. PXRD is well established for structure refinements, especially when sufficiently large single crystals are not available. Compare to single-crystal XRD, in PXRD the overlap of Bragg peaks is observed, but using synchrotron facility as X-ray source, because of high resolution can partly solve this problem [51].

Synchrotron X-ray powder diffraction (SXRD) is much more powerful in comparison with the laboratory analogs because of the unique properties of synchrotron X-ray beams [53], such as higher brilliance which leads to smaller angular divergence of the beam (high-angular resolution data can be obtained) and deep probing of structural details with high contrast (high signal-to-noise ratio) data for the detection of small features; horizontal polarization, which reduces the fall in intensity as a function of 2θ; tunable X-ray wavelength, which avoids X-ray absorption problems of individual atoms and reduces sample fluorescence that causes high background; a large or spacious instrument for different sample environments; faster data acquisition [51].

Today very high-brilliance beamlines have been constructed for hard X-ray (typically at energy >30 keV) measurements, with possibility of the dynamic studies. Main advantages to perform in

situ and in operando PXRD studies are [54] higher penetration depths and lower radiation damage as a result of a reduction of ionizing electrons from photoelectric effects [51].

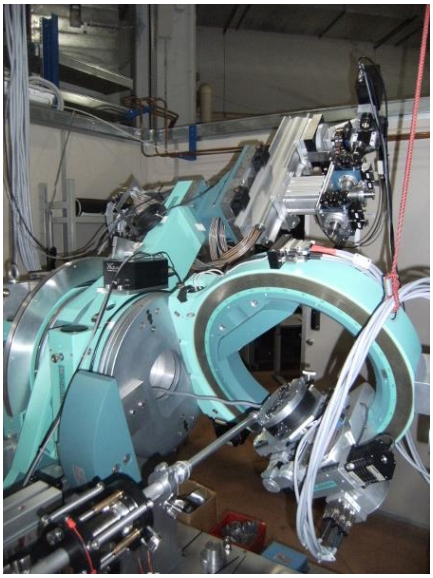

Figure 11. Diffractometer at MCX beamline in "Elettra" synchrotron facility

Any peak on the diffraction pattern can be characterized with position, intensity, width, shape and asymmetry [55]. Positions of the diffraction peaks on 2θ axis shows the geometry of the crystal lattice i. e. the size and the shape of the unit cell. It can be used for qualitative analysis. In PXRD a Bragg peak position corresponds to the interplanar distance, so all the families of planes with the same interplanar distance will appear at the same position. Peak intensity is used in quantitative analysis. From intensity, it is possible to retrieve some information about crystalline structure.

$$I_{hkl} = SLp_{hkl} \cdot M_{hkl} \cdot A(\theta) \cdot |F_{hkl}|^2$$

Where, *F* is structure factor, also in *F* temperature factor is included, *M* – multiplicity factor, *p* – polarization factor, *L* – Lorentzian factor, *A* – absorbance factor [56].

The width can be affected by the size and strain. Reflection broadening by reduced crystallite size is described by the Scherrer equation:

$$\beta_s = k \cdot \lambda \cdot (L_{vol} \cos\theta)^{-1}$$

Strain can be produced by point defect, because of missing atom, wrong atom or atom in interstitial, which leads to variation of d values. Reflection broadening by strain can be described as [55]:

$$\beta_v = 4\varepsilon_0 \tan\theta = 4\varepsilon \sin\theta / \cos\theta\,, \qquad where \quad \varepsilon = \Delta d/d$$

Even from background some information can be retrieved, such as if the compound is amorphous, about local order and fluorescence [56].

2.1.3. X-ray Fluorescence Spectroscopy

XRF (X-ray fluorescence) analysis is a powerful analytical tool for the spectrochemical determination of almost all the elements. XRF radiation is induced when photons emitted from an X-ray source of sufficiently high energy impinge on a material and eject a core electron of one of the elements inside the sample. Part of this energy can be absorbed as photoelectric absorption and the same time the electron can be ejected from its position. Atom is in unstable, ionized state as long as the vacancy exists in the shell. There are two processes, which may occur after vacancy is created: outer shell electron is filling the vacancy and because of the excess of the energy, second electron from outer shells is emitted as a photoelectron. Auger electron spectroscopy is based on this phenomena. Second option is for electron from outer shell to fill the vacancy and because of the difference in energy between initial and final state, this excess of energy is given off as an X-ray photon [57].

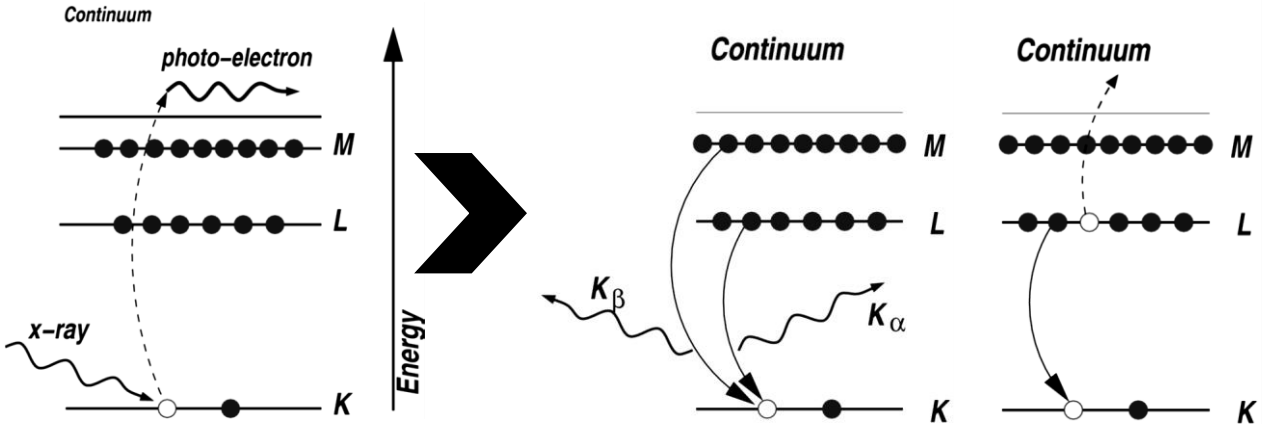

Figure 12. X-ray absorption and photoelectron ejection (left) and processes afterwards: Auger electron formation (middle) or X-ray Fluorescence (right) [46]

The working principle of XRF analysis is the measurement of wavelength or energy and intensity of the characteristic photons emitted from the sample. This allows the identification of the elements present in the analyte and the determination of their mass or concentration [58]. However the fluorescence yield has much higher value for the high atomic number elements, compare to light ones, so sensitivity is poor in low atomic mass elements. It is possible to identify Z>8 elements [57]. For the fluorescence yield, Moseley's law in applied:

$$1/\lambda = K(Z - \sigma)^2$$

Where, K and σ are constants, which have specific values for the energy distribution levels and sublevels involved in the given transition [57].

Generally, there are two types of XRF instrumentation: energy dispersive (ED) and wavelength dispersive (WD) spectrometers.

2.1.4. Transmission X-ray microscopy (TXM)

Energy-dependent full-field transmission soft X-ray microscopy is a powerful spectromicroscopical technique based on synchrotron radiation, which provides chemical information with spatial resolution at the nanoscale. X-ray absorption imaging technique consists in detecting the photons transmitted through the observed object. Experimentally, the number of photons N after the transmission through the sample, along z, obeys to the Beer-Lambert's law:

$$N(x,y) = N_0(x,y)\exp\left[-\int_{sample} \mu(x,y,z)dz\right]$$

Where N and N_0 are the emerging and incident number of photons, respectively, and the integral is extended through all the sample thickness, in case of not oriented samples (neglecting the polarization) μ is constant along z. The measured transmission $T=I/I_0$ (with I and I_0 proportional to N and N_0, respectively) depends exponentially on the linear absorption coefficient μ, integrated along the X-ray path in the sample. The contrast will therefore depend on the sample thickness, the elemental composition, their density, and the energy and polarization of the incident radiation. In the resulted images some parts will suddenly become darker (or brighter in case of using the absorbance) when the radiation is triggering some electronic transitions. As the exact energy is dependent on the atom environment, it is also possible to detect chemical states of the same element. In a synchrotron-based transmission X-ray microscope the spatial resolution for chemical information is few tens of nanometers. By using X-rays of the "soft" energy region (<3 KeV), it is possible to access transitions from core levels of light elements, such as the K-edge of nitrogen, oxygen, fluorine, as well as L – and M - edges of heavier elements [59, 60].

Two types of microscope geometries are used at synchrotron radiation sources: the full-field transmission X-ray microscope (TXM) and the scanning transmission X-ray microscope (STXM).

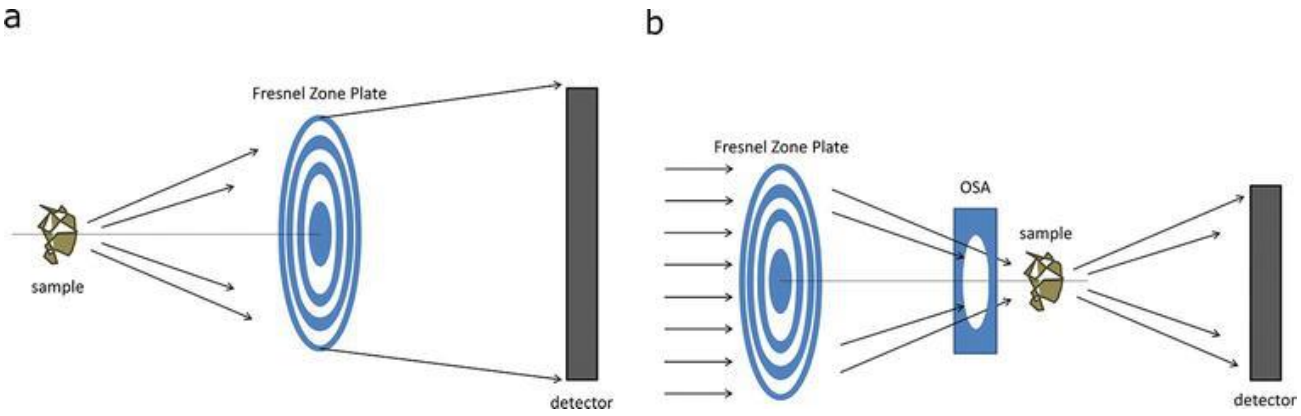

Figure 13. The full-field transmission X-ray microscope (a) and the scanning transmission X-ray microscope (b)

Both of them are lens microscopes based on the application of Fresnel Zone Plate diffractive lenses (ZP). As for a detection, typically a CCD-based detector is used. In a STXM system, the sample is scanned through the ZP focal spot and the full image of the sample is reconstructed electronically, step by step. The spatial resolution will be limited by the dimension of this focal spot. For the TXM case there is a typical scheme of a common visible light microscope: a sample is placed at the focal plane of two lenses, a full magnified image of the sample is produced on to the detector plane. The spatial resolution is limited by the numerical aperture of the objective lens. To sum up:

Table 2. The main differences between TXM and STXM

TXM	**STXM**
Best spatial resolution	Good spatial resolution
Shortest exposure time	Longer exposure time
Higher radiation dose	Least radiation dose
	Requires spatially coherent radiation

The main advantage of the STXM over the TXM system is smaller radiation dose, on the other hand the main advantage of the TXM over the STXM system is in terms of the exposure time: in one “snapshot” the full image of the sample is obtained [59, 61]. At the Mistral beamline of the ALBA Light source, there is a soft X-ray full-field transmission microscope. It can work in the energy range between the C–K edge and the Ni L edge excluded, i.e., 290–850 eV. Microscope works in in ultra-high vacuum chambers (working p $\sim 1\times10^{-9}$ mbar) to minimize absorption and scattering of the X-ray beam [62].

2.2. Other Characterization Techniques

2.2.1. Microwave Plasma-Atomic Emission Spectroscopy (MP-AES)

The basic aim of atomic spectroscopy technique is to identify elements and quantify their concentrations in different materials. The principle of Microwave Plasma-Atomic Emission Spectroscopy is similar to other emission technique: the intensity of each emitted line is directly proportional to the concentration of a particular element [63]. Instead of flammable and oxidizing gases in this technique, there is a magnetic excitation microwave plasma source. Plasma gas is typically nitrogen. In MP-AES as another advantage can be considered the fact, that there are not used hollow cathode lamps [64].

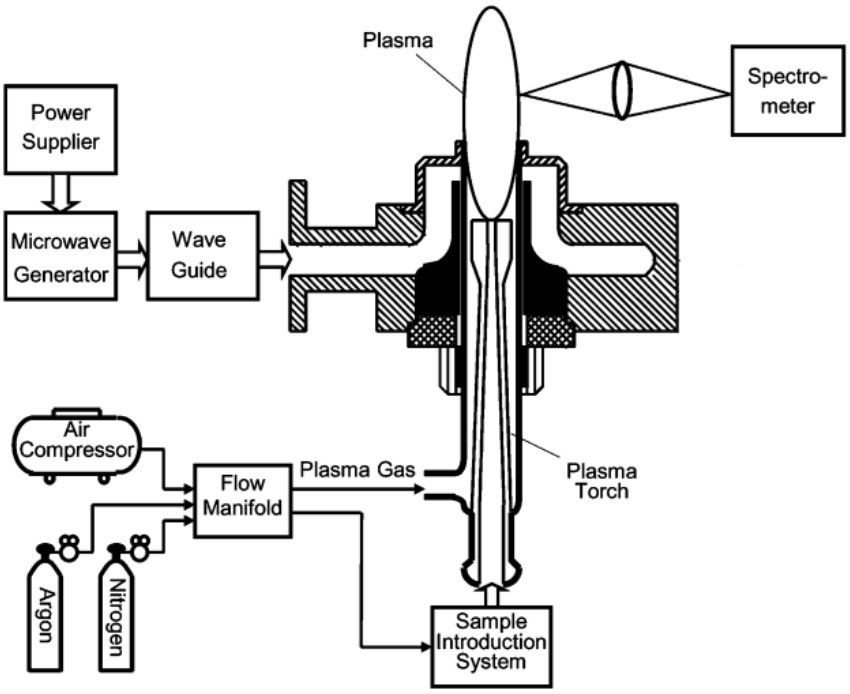

Figure 14. General schematic diagram of the high-powered MIP system [65]

2.2.2. Thermogravimetric Analysis (TGA)

Thermogravimetric Analysis is a technique in which the mass of a substance is monitored as a function of temperature or time as the sample is subjected to a controlled temperature program in a controlled atmosphere, which means that with the heating of a material, its weight increases or decreases and TGA measures a sample's weight as it is heated or cooled in a furnace.

A TGA consists of a sample pan which is supported by a precision balance. That pan is heated or cooled during the experiment, while the mass of the sample is monitored. The sample environment is controlled by the sample purge gas, which might be inert or reactive. It flows over the sample and exits through an exhaust. Commonly, TGA instruments can quantify loss of water, solvent or plasticizer, decarboxylation, pyrolysis, oxidation, decomposition, weight % of the filler, amount of metallic catalytic residue remaining on carbon nanotubes, etc.

On the TGA graph the abscissa (X-axis) can be displayed as time or temperature and the ordinate (Y-axis) can be displayed as weight (mg) or weight percent (%). Curve is displayed from left to right. The descending nature of TGA thermal curve indicates the occurrence of the weight loss. For the starting point the extrapolated onset temperature should be taken, which indicates the beginning of the specific compound loss. The peak of the first derivative, also known as the inflection point indicates the point of greatest rate of change on the weight loss curve [66].

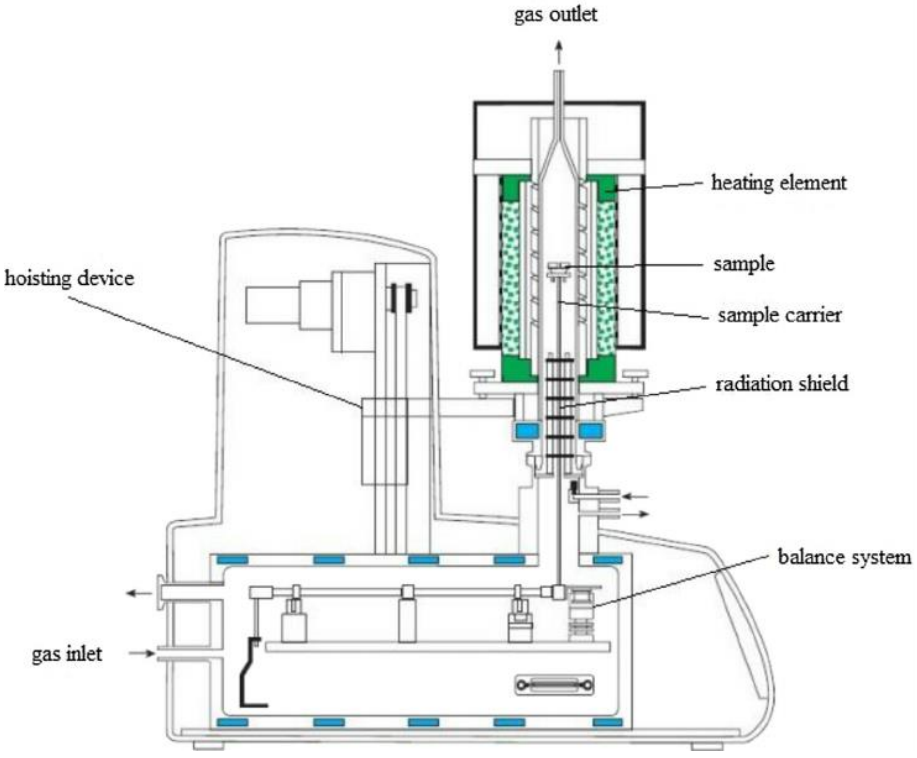

Figure 15. General scheme of TGA apparatus [67]

2.2.3. Infrared Spectroscopy (IR)

Infrared spectroscopy can be used to detect the functional groups inside the material. Sometimes information about the proximity of on group to another can be obtained. In some cases it is also possible to give data about the amount of sample present.

Infrared spectroscopy is based on vibrations inside the molecule. The atoms in molecules are not static, but vibrate around their equilibrium positions, even in the solid state. Each atom vibrates with a specific frequency, which depends on its mass and the length and strength of the bonds that it is forming. The natural frequency of vibration of the bond is in the infrared region of the electromagnetic spectrum [68]. So the radiation in infrared region can be used in spectroscopy as it can excite vibrational states of the molecule.

The infrared spectroscopic study of organic compounds has been much before the application to inorganic compounds. Most of the early work on the spectra of inorganic compounds were obtained by Raman spectroscopy. Some reflection infrared methods [69] were used as early as 1930. The Iack of high-resolution spectrophotometers and difficulty of sample preparation delayed progress in this field. Because of the large particle size in inorganic samples, considerable scattering losses were observed and consequently most early infrared spectra of inorganic compounds gave broad, indeterminate absorptions compared to the sharp spectra obtained with organic compounds. With the introduction of commercial high-resolution spectrophotometers and new methods of sample preparation [70, 71, 72, 73] , obtaining high quality spectra became possible. In this filed important work has been done by Lecompte and his co-workers, who examined numerous inorganic compounds, in 1951 [74, 75]. Also Miller and Wilkins [76], in 1952, they examined the spectra of over 150 salts [77].

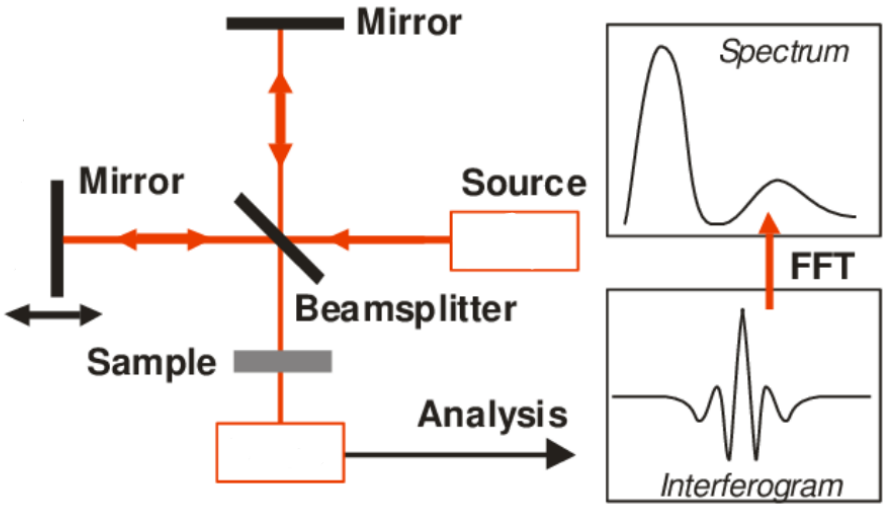

Figure 16. General scheme of FT-IR spectrometer [78]

2.3. Electrochemical techniques

2.3.1. Cyclic Voltammetry (CV)

Cyclic voltammetry (CV) is a powerful and popular electrochemical technique commonly used for investigation of redox processes, in the analyses of electrochemical reactions between ions and surface atoms of electrodes, for understanding reaction intermediates for obtaining stability of reaction products, for qualitative information on electrode reaction mechanisms, qualitative properties of the charge transfer reactions between electrolyte ions and electrons from the electrode surface [79, 80, 81].

Cyclic voltammetry uses a three electrode electrochemical cell and it is based on changing the applied potential at a working electrode in both forward and reverse directions while observing the current. This technique involves a linear and a cyclic variation of electrode potential between the working and reference electrodes within a potential window, by measuring the current that flows between working and counter electrodes. These cycles may be repeated many times. CV is a potentiodynamic electrochemical measurement [82]. In voltammograms, or cyclic voltammograms, the *x*-axis represents the applied potential, while the *y*-axis is the, resulting current passed.

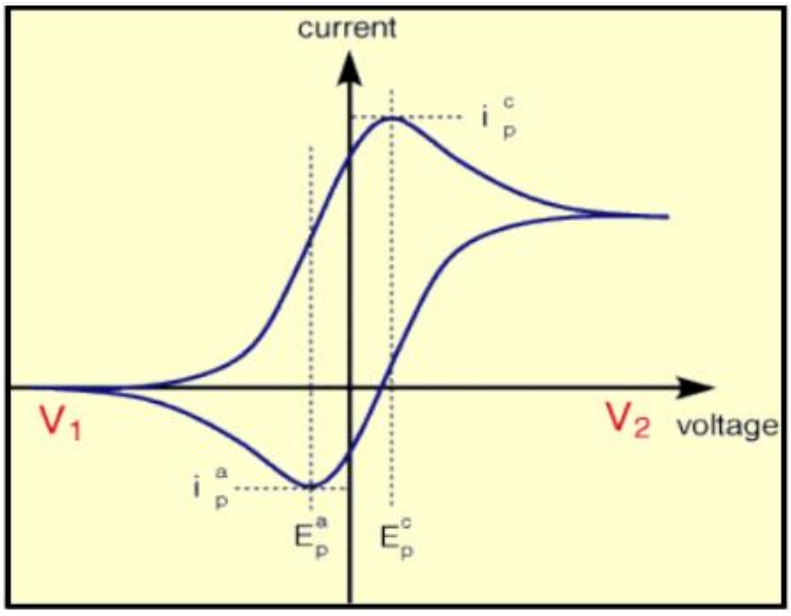

Figure 17. Cyclic Voltammogram, Peak potentials (E_p^c, E_p^a) and peak currents (i_p^c and i_p^a) of cathodic and anodic peaks [82]

The equilibrium between oxidized and reduced species is described by the Nernst equation:

$$E = E^0 + \frac{RT}{nF}\ln\frac{(Ox)}{(Red)} = E^0 + 2.3026\frac{RT}{nF}\log_{10}\frac{(Ox)}{(Red)}$$

The Nernst equation relates the potential of an electrochemical cell (E) to the standard potential of a species (E^0) and the relative activities of the oxidized (Ox) and reduced (Red) analyte in the system at equilibrium. F is Faraday's constant, R is the universal gas constant, n is the number of electrons, and T is the temperature [83].

In application of the Nernst Equation to the one-electron reduction, the activities are replaced with their concentrations, which are more experimentally accessible, the standard potential E^0 is replaced with the formal potential $E^{0\prime}$, and n is set to equal to 1. This equation provides a powerful way to predict how a system will respond to a change of concentration of species in solution or a change in the electrode potential. During the potential scanned in the CV experiment, the concentration of the species in solution near the electrode changes over time and equilibrate in accordance with the Nernst equation [83].

If the reduction process is chemically and electrochemically reversible, the difference between the anodic and cathodic peak potentials is called peak-to-peak separation (ΔE_p). This peak separation of 59mV per electron, theoretically for one electron process. Electrochemical reversibility refers to the kinetics of the electron transfer between the electrode and the analyte. When there is a low barrier to electron transfer (electrochemical reversibility), the equilibrium is reached immediately after any change in applied potential is applied. On the other hand, when there is a high barrier to electron transfer (electrochemical irreversibility), electron transfer reactions need more negative (positive) potentials to observe reduction (oxidation) reactions and consequently ΔE_p is larger [83].

In CV the potential can be scanned in negative mode (cathodically) or positive mode (anodically). The scan rate of the experiment controls how fast the applied potential will be scanned. Faster scan rates lead to a decrease in the size of the diffusion layer; as a consequence, higher currents are observed [84, 85].

When the cell is assembled, and the analyte has been added, a potential develops at the electrodes, the potential of the electrode equilibrates with the solution which is called the open circuit potential (OCP) [83]. So, prior to measurement, it is important to check the OCP.

II. Experimental Part

1. Synthesis

For the synthesis of manganese hexacyanoferrate 0.1 M solutions of $Na_4Fe(CN)_6$, $MnSO_4$ and Na_2SO_4. At 41˚C temperature (approximately), under magnetic stirrer and nitrogen flow in sodium sulfate solution slowly was added (3.3mn/min) manganese sulfate and sodium hexacianoferrate (also under N_2 flow). After reagents were fully added, stirring continued additional 2 minutes.

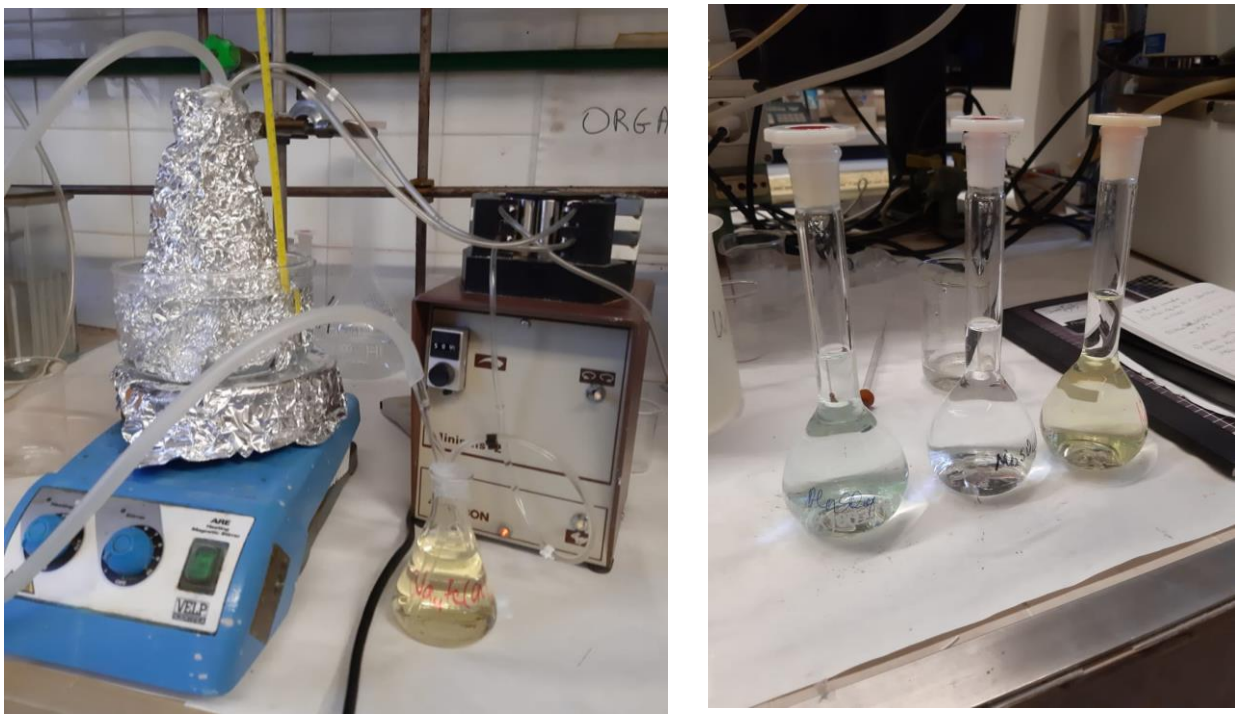

Figure 18. The synthesis of MnHCF (left); Reagent flaks with (from left to right): $MnSO_4$, Na_2SO_4 and $Na_4[Fe(CN)_6]$ (right)

The mixture was aged for 5 days, on the room temperature, in the dark place. Following centrifugation was done as well as washing with distilled water three times. Samples were dried at 60˚C for two days and after grinded in mortar.

Procedure was similar in case of nickel addition. $NiSO_4$ was preliminary mixed with $MnSO_4$ 10/90 or 30/70 for 10% and 30% concentrations of nickel, respectively.

Table 3. Obtained products

Products	$Na_xMn_y[Fe(CN)_6]$	$Na_xNi_zMn_y[Fe(CN)_6]$ (Ni 10%)	$Na_xNi_zMn_y[Fe(CN)_6]$ (Ni 30%)
Weight (g)	3.00	2.40	2.30

2. Electrode Preparation For Electrochemical Tests

75 mg of dried sample was preliminary mixed with 25 mg carbon black preliminary mixed in mortar. Afterwards 5 mg of polytetrafluoroethylene (PTFE) as binder was added and continually mixed/pressed in mortar for approximately one hour. Than pellets with 5 mm and 8 mm diameter was made with mass range of 1-2 mg for 5 mm diameter samples and 2-4 mg for 8 mm samples. Pellets were pressed between aluminum mesh and dried in the oven. Before analysis the sample was put inside electrolyte solution under vacuum for at least 2 hours.

Figure 19. Pellet preparation in mortar

Table 4. Mass of Prepared Samples

MnHCF	MnHCF + Ni 10%	MnHCF + Ni 30%
1.40	1.46	1.54
1.70	1.47	1.57
1.90	1.38	1.31
1.39	2.58 (8 mm)	1.10
3.1 (8 mm)	1.8	1.00
3.34 (8 mm)	1.6	1.50
	1.5	

As electrolyte $NaNO_3$ aqueous solution was used. The concentration of sodium nitrate was 0.1M 1M and 5M.

Prior to the electrochemical test, to assemble the three electrode glass cell, the sample (already inside the aluminum mesh) was cut to “T” shape, and silver paste was put on the place of the contact with the clip.

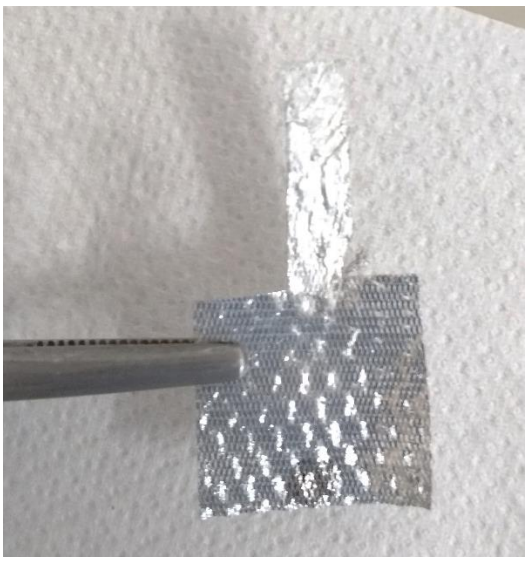

Figure 20. Sample electrode fixed inside the aluminum mesh

3. Methods and equipment

3.1. Synchrotron techniques

XAS - X-ray absorption spectroscopy (XAS) experiments were conducted at "Elettra" Synchrotron Trieste, Basovizza (Italy), at XAFS beamline. On this beamline K-edges from sulfur to silver and L-edges from yttrium to bismuth are accessible [86]. Photon flux is 10^9 - 10^{10}.

The monochromator is placed at 21.7 m from the source. It is a double flat crystal double cam Kohzu apparatus. The energy range 2.4 - 27 keV can be covered by interchanging the pairs of Si(111) and Si(311) crystals under vacuum. $\Delta E/E$ is 10^{-4} for Si 111 and $5x10^{-5}$ for Si 311 [87, 88]. In the experimental station there are three ionization chambers by Oxford Instruments for measurements in transmission mode. These are filled with optimal He, N_2, Ar, Kr gas mixture at a total pressure of 2 bars and are operated at a field of 2 kV per 30 cm of length. The ionization chambers signals are amplified by Keithley picoamperomers and the digitalized by a voltage to frequency converters for the data collection on PC. There is a total electron yield detector to collect x-ray absorption fine structure spectra at l-N_2 and room temperature, and a silicon drift detector for measurements in fluorescence mode [89].

Generally, the acquisition can be made in three modes: transmission, fluorescence and total electron yield. In this analysis transition mode was used. The K-edges of Mn, Fe and Ni were collected. For Mn the energy range was 6345-7100 eV; for Fe 6916 – 8101eV (8348eV for pure MnHCF), for Ni 8138 – 9567 eV. XAS spectra were calibrated using the Athena software.

PXRD - data were recorded at the MCX beamline in "Elettra" synchrotron Trieste, Basovizza (Italy). The optics of the line consist of two mirrors and the monochromator: a first Pt-coated cylindrical mirror collimates the beam on the horizontally focusing Si (111) double crystal monochromator in 1:1 configuration; the second mirror is for the vertical focusing, it is platinum coated, flat and bendable. The double crystal monochromator (DCM) consists of two Si crystals (active area 50×50 mm^2, manufactured cut along the [111] direction, which can be precisely positioned and oriented in the X-ray beam. One will direct photons of the desired energy parallel to the incoming beam direction, the second crystal provides sagittal focusing [90]. 2θ precision better than 0.0001° flat sample-holder plate (Ø 100 mm) controlled by a precision (1 m) x-y-z motor system, 360° phi-rotation and -90 ÷ +90° chi-tilting [91]. Beamline energy range is 6 - 20 eV, max flux $10 \cdot 10^{11}$ ph/s (9 keV), spot size on the sample is 300-2000 μm and 300-1000 μm for horizontal and vertical respectively [92]. Monochromator energy range 6-20 keV [93]. A monochromatic X-ray beam with a wavelength of 1 Å was used. Data were collected on the sample in a capillary geometry, setting the spinner at 300 rpm. The X-ray diffraction (XRD) pattern was

collected consecutively in the range 5º<2θ<70 º, with steps of 0.01 º and an acquisition time of 1s/step. Additionally, on samples, containing nickel, longer acquisition times were also used: 3s/step. The crystal structure was refined using Fullprof Suite.

2D XRF - The data was collected in XRF beamline in "Elettra" synchrotron Trieste, Basovizza (Italy). This beamline is dedicated to spectrometry, spectroscopy, microscopy, and reflectometry. Double crystal monochromator with resolving power $1.4 \cdot 10^{-4}$ enables the access to the energy range of 2-14 keV. The source is re-imaged to a 450 x 300 μm beamsize at exit slits (~ 23 m from the source), with an angular divergence of 0.15 mrad and a transmitted flux of about 5 109 ph/s (at 5500 eV, machine mode 2GeV). The experimental flux curves for the 2 storage ring operation energies and are normalized to the beam. Also 2 ionization chambers are available, behind a 0.3mm thick Beryllium window [94]. The sample environment is an Ultra-High-Vacuum Chamber [95].

The fluorescence measurements are performed using a Silicon Drift Detector (SDD) (XFlash 5030, Bruker Nano GmbH, Germany). It has a 30 mm^2 nominal crystal area, a thickness of 450 μm and resolution equal to 131 eV. It is equipped with a Super Light Element Window (SLEW). A Zr collimator is placed in front of the detector chip to prevent the detection of photons at the edges of the crystal and to improve the energy resolution and the peak to background ratio. To prevent the detection of photo- or Auger electrons emitted from the sample surface, the SDD is coupled with an electron trap (permanent magnet) placed in front of the end [96].

2D XRF analysis was done on pristine as well as Li containing charged (LiFC) and discharged (LiFD) samples and corresponding charged and discharged samples after 20 cycles (LiFC20 and LiFD20, respectively). Energy = 7200 eV; beam size = 200 x 100 mm^2 and further analysis while moving the incident energy to 6553 eV.

TXM – analysis was done in MISTRAL is Soft X-ray microscope beamline in Cerdanyola del Vallès, Barcelona, Spain. It is the full-field Transmission X-ray Microscopy beamline and one of the seven phase-I beamlines at ALBA. The Transmission X-ray Microscope (TXM) works from 270 eV to 1200 eV. A single-reflection elliptical glass capillary condenser focuses monochromatic light on to the sample, which is at cryo-temperature. The transmitted signal is collected by an objective Fresnel Zone plate (of 25 or 40 nm outermost zone widths) and a magnified image is delivered to a direct illumination CCD camera. The routinely expected spatial resolution in 2D is 30 nm and ~50 nm for tomographies. Energy resolution is up to $E/DE=5x10^3$, sample format - 3.05 mm TEM round grid. There is tilting possibility of ± 65º, X-ray magnification adjustable range

depends on the objective which was used. Detector type is PIXIS-XO: 1kx1k, pixel size = 13μm [97].

For the analysis the electrochemica conditions were as follows: Swagelok T cells, as positive electrode was used $Na_{1.9}Mn_{1.1}[Fe(CN)_6]$, (85:10:5=AM:CB:PVDF); as negative and counter electrodes - **Li** metal, electrolyte: 1M LP30 (**Li**), mass loading: 1.91 +/- 0.09 mg/cm^2. Theoretical specific capacity was considered to be 150 mAh/g, imposed current: C/10 (about 0.035 mA), potential range: 2.3 < E < 4.3 V (**Li**), initial positive polarization after 6 h of rest time. After that the cells dismantled in glove box to extract the electrodes that were rinsed with DMC, dried and scraped. The powder was deposed on standard carbon-coated TEM grids, and introduced to the TX microscope through a special transport chamber that avoids contact with air Analysied saples were formulated electrode (pristine), fully charged and fully discharged samples after one and fifty cycles.

3.2. Laboratory techniques

MP-AES - in this analysis The Agilent 4210 MP-AES was used, which is a high sensitivity optical emission spectrometer. Detection limits are down to ppb levels and linear dynamic range is larger compared to flame Atomic absorption spectrometer. In case of gases and liquids sample pretreatment is not necessary, in case of solids, solution preparation is needed. MP-AES is typically used on wide range of multi-element analyses [98]. During the test, first different concentration (0, 10ppm, 20 ppm, 30 ppm and 40 ppm) standard solution of Fe, Mn, Ni and Na was prepared (diluted by 0.5M nitric acid); then the sample was solved in 0.5M nitric acid. Three different analytical lines (wavelengths) were chosen for each element during the test.

TGA - the analysis was done from room temperature (25 °C) to 500 °C for manganese hexacyanoferrate and to 550 °C for the samples with the addition of nickel, with a heating rate of 5°C/min, and rapid cooling.

IR - the analysis was done with Bruker Alpha FT-IR spectrometer in ATR (attenuated total reflectance) mode at spectral range of 4000-400 cm^{-1}.

CV - Cyclic voltammetry (CV) was performed on the CH Instruments Model 660. For the analysis three electrode aqueous glass cell was assembled. As a work electrode the synthesized material was used, platinum wire as counter electrode and for the reference electrode saturated calomel electrode (SCE). The samples were tested from -0.8 or -1 to up to 1.2-1.3 V. generally in positive mode, but sometimes negative mode was also used. Scan rate in most cases 50, 20, 10, 5 and 1 mV. Open circuit potential was checked before every analysis. On the same apparatus A. C. Impedance experiment was also done in frequency range of 0.01 – 100 000 Hz, amplitude 0.005V.

Figure 21. Assembled three electrode system for cyclic voltammetry experiment

III. Results And Discussion

1. Defining The Formula: MP-AES And TGA

For the finding the exact formula of the synthesized compounds, MP-AES and TGA experiments were done. The results of atomic absorption spectroscopy are as folows:

Table 5. MP-AES measurements of Fe, Na, Mn and Ni, each on three different wavelength

Fe			
Wavelength nm	Concentration ppm (mg/L)		
	MnHCF	MnHCF + 10% Ni	MnHCF + 30% Ni
259.940	13.18	10.57	9.11
373.486	13.12	10.31	9.49
371.993	13.43	10.16	9.17
Average Concentration ppm (mg/L)	**13.24**	**10.34**	**9.25**
Na			
Wavelength nm	Wavelength nm		
568.820	568.820	568.820	568.820
588.995	588.995	588.995	588.995
589.592	589.592	589.592	589.592
Average Concentration ppm (mg/L)	Average Concentration ppm (mg/L)	Average Concentration ppm (mg/L)	Average Concentration ppm (mg/L)
Mn			
Wavelength nm	Concentration ppm (mg/L)		
	MnHCF	MnHCF + 10% Ni	MnHCF + 30% Ni
257.610	16.93	16.29	11.9
280.108	16	15.10	10.82
403.076	15.96	15.04	10.88
Average Concentration ppm (mg/L)	**16.29**	**15.47**	**11.20**
Ni			
Wavelength nm	Concentration ppm (mg/L)		
	MnHCF + 10% Ni	MnHCF + 30% Ni	
232.003	0.93	1.82	
349.295	0.92	1.85	
352.454	0.94	1.87	
Average Concentration ppm (mg/L)	**16.29**	**15.47**	

Obtained results were averaged, recalculated at first to the molar concentration and afterwards to the molar ratio. The formulas are written two ways, per Fe and per Mn.

Table 6. MnHCF formula calculation

Element	Atomic mass	MnHCF				
		Molar concentration (mmol/L)	Molar ratio		Formula (without water)	
			/Fe	/Mn	/Fe	/Mn
Fe	22.989769	0.237	1	0.799	$Na_{2.17}Mn_{1.25}[Fe(CN)_6]$	$Na_{1.74}Mn[Fe(CN)_6]_{0.8}$
Mn	54.938044	0.297	1.251	1		
Na	55.845	0.515	2.173	1.738		

In case of samples with the addition of nickel, instead of per Mn, manganese and nickel sum has been taken as "one".

Table 7. MnHCF + Ni 10% and MnHCF + Ni 30% formula calculation

Element	Atomic mass	MnHCF + Ni 10%				
		Molar concentration (mmol/L)	Molar ratio		Formula (without water)	
			/Fe	/Mn+ Ni	/Fe	/Mn
Fe	22.989769	0.185	1	0.623	$Na_{1.94}Ni_{0.086}Mn_{1.52}[Fe(CN)_6]$	$Na_{1.21}Ni_{0.053}Mn_{0.95}[Fe(CN)_6]_{0.62}$
Mn	54.938044	0.282	1.520	0.947		
Na	55.845	0.360	1.942	1.209		
Ni	58.6934	0.015845	0.086	0.053		
MnHCF + Ni 30%						
Fe	22.989769	0.166	1	0.704	$Na_{2.37}Ni_{0.19}Mn_{1.23}[Fe(CN)_6]$	$Na_{1.67}Ni_{0.134}Mn_{0.87}[Fe(CN)_6]_{0.7}$
Mn	54.938044	0.204	1.230	0.866		
Na	55.845	0.393	2.369	1.668		
Ni	58.6934	0.031	0.190	0.134		

From the results it can be concluded, that sodium content is decreasing from pure MnHCF to 10% nickel doped sample and then increasing again in Ni 30%. Obtained results do not include water content. For taking into the consideration the water inside the samples, thermogravimetric analysis was conducted and further calculations were made.

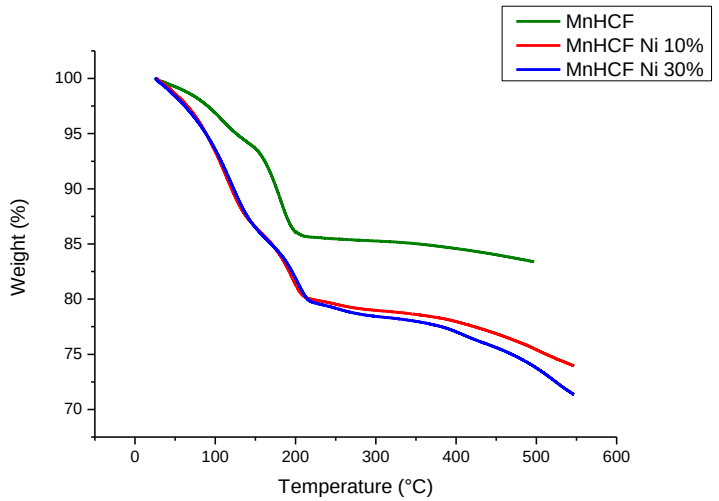

Figure 22. TGA Analysis

From the literature it is known that in MnHCF loses absorbed water at up to 120 °C. Sharp weight loss near 190 °C indicates for the loss of interstitial water. On higher temperature the decomposition of the MnHCF framework occures. In this case, manganese hexacyanoferrate loses water up to 199°C. However, with Ni addition, there is a shift toward the higher temperature [99], here up to 210-215 °C, with addition of 10 and 30% of nickel, respectively. It is also worth to mention, that TGA curves indicate, that with the addition of nickel, water content increased inside the synthesized material.

TGA first derivative graphs also have been constructed, showing the temperature where the maximum amount of water was lost (inflation point). However, one must consider, that the first inflation point cannot evaluate the general amount of the water that has been lost from the sample.

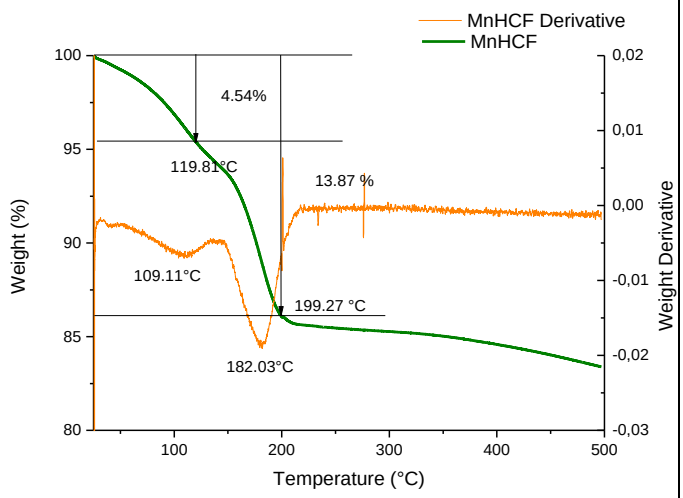

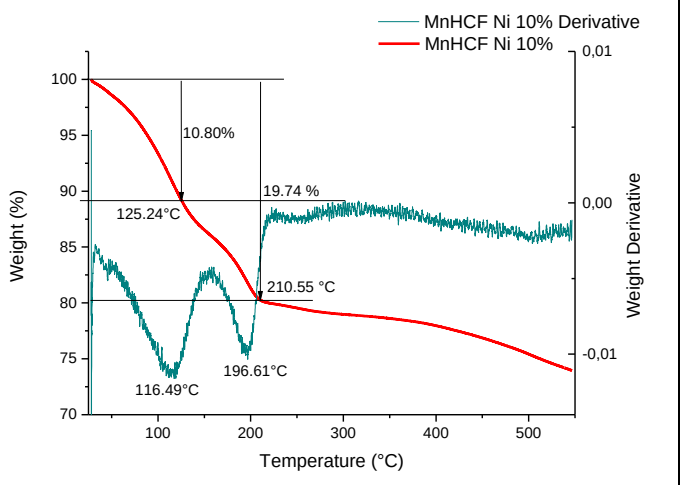

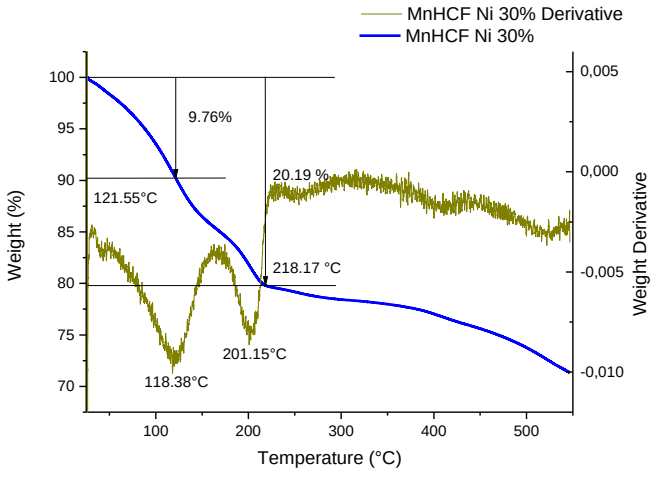

Figure 23. TGA graph and 1st Derivative of MnHCF (Top), MnHCF + Ni 10% (Bottom left) and MnHCF + Ni 30% (Bottom right)

After considering the results from TGA analysis and further calculation, new formulas were obtained already with addition of water in it:

Table 8. Final formula of the synthesized compounds

Formula	MnHCF	MnHCF + 10% Ni	MnHCF + 30% Ni
/Fe	$Na_{2.17}Mn_{1.25}[Fe(CN)_6]\cdot 2.96H_2O$	$Na_{1.94}Ni_{0.086}Mn_{1.52}[Fe(CN)_6]\cdot 4.71H_2O$	$Na_{2.37}Ni_{0.19}Mn_{1.23}[Fe(CN)_6]\cdot 4.85H_2O$
/Mn or /Mn+Ni	$Na_{1.74}Mn[Fe(CN)_6]_{0.8}\cdot 2.36H_2O$	$Na_{1.21}Ni_{0.053}Mn_{0.95}[Fe(CN)_6]_{0.62}\cdot 3.7H_2O$	$Na_{1.67}Ni_{0.134}Mn_{0.87}[Fe(CN)_6]_{0.7}\cdot 3.41H_2O$

The vacancies inside the MnHCF considering the general formula $A_xM[Fe(CN)_6]_{\gamma}\square_{1-\gamma}\cdot zH_2O$, are 20%. This value is increasing in Ni doped samples, especially with 10% addition, for up to 38% and then decreasing to 30% in the sample with 30% of nickel in it.

2. IR Analysis

Infrared spectra of the synthesized compounds were obtained.

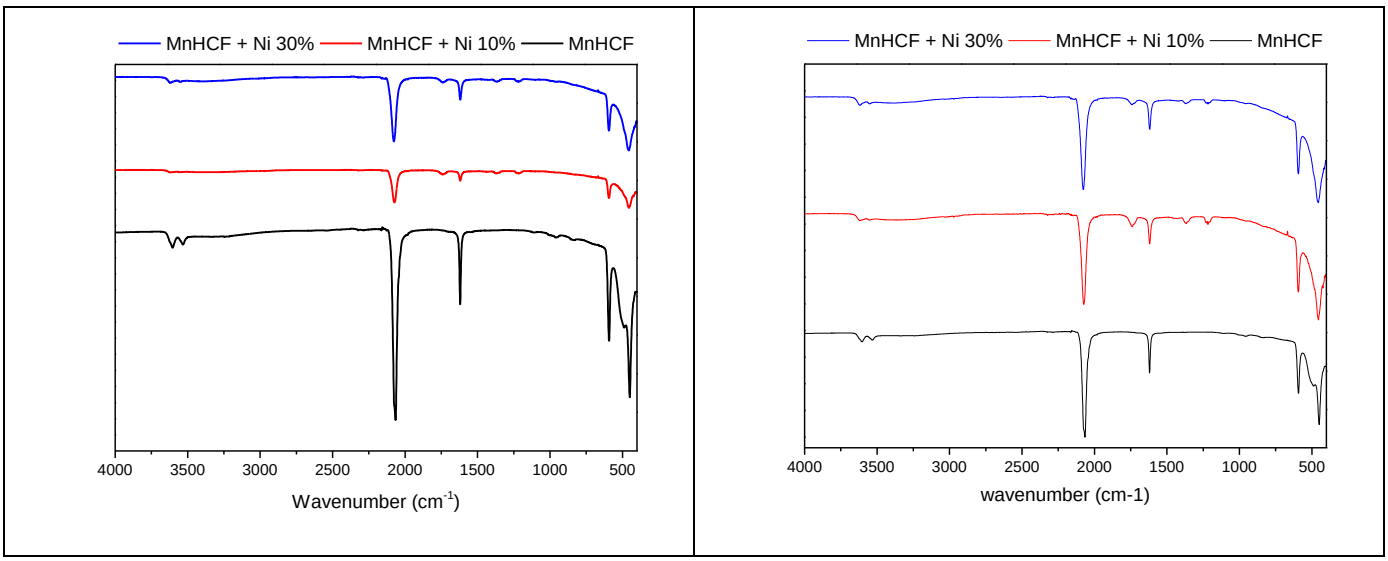

Figure 24. IR spectra of MnHCF, MnHCF + Ni 10% and MnHCF + Ni 30% (left) and normalized spectra (right)

From literature it is known, that in IR spectra of $K_4Fe^{II}(CN)_6$ and $K_3Fe^{III}(CN)_6$ complexes The C≡N stretches are found at approximately 2037.6 and 2115.2 cm^{-1}, for the Fe(II) and Fe(III) complexes, respectively. 2037.6 cm^{-1} is well-known C≡N stretching region of metal−cyanide complexes of the metal−ligand bonding interactions [100]. An increase in the effective charge on the iron resulted in a decrease of the metal−C≡N π back-bonding and an increase in the metal−C≡N σ bonding. The difference in the metal−ligand bonding interactions of the aqueous hexacyanoferrate complexes led to this 77.6 cm^{-1} blue shift and approximately 3 times decrease in the intensity of the C≡N stretch for the ferric species in comparison with its ferrous counterpart [101].

On IR spectra the signal of C≡N stretching of MnHCF was observed on 2066 cm^{-1}, whereas for MnHCF + Ni 10% and MnHCF + Ni 30% the signal was blue shifted for around 10 cm^{-1}. Band position shows mainly Fe^{II} character of the iron inside the complex. However, the shift appearing after the addition of Ni to Mn should have caused an increase in the effective charge on the iron, weakened metal−C≡N π back-bonding and strengthen σ bonding. The decrease of intensity is also observed as was expected from the literature. It worth to mention that the shoulder on 2075 cm^{-1} is also observed in case of pure MnHCF, but main signal is still centered on 2066 cm^{-1}.

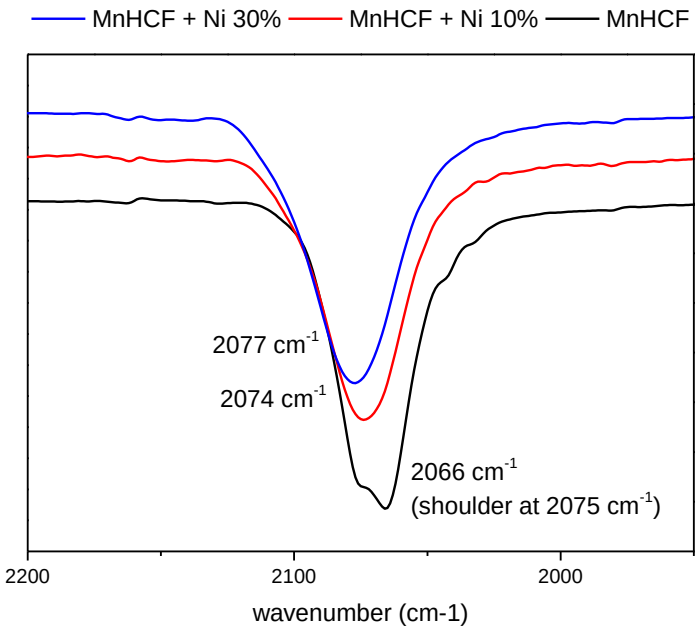

Figure 25. IR spectra region 1900-2200 cm -1 of MnHCF, MnHCF + Ni 10% and MnHCF + Ni 30% (normalized)

Fe-C-N-Fe bending modes characteristic in the far observed in infrared region (450-650 cm^{-1}) [102, 103]. The band at 592 cm^{-1} is assigned to a Fe^{2+}–CN stretching mode from ferrocyanide [104, 105]. Mn-N stretching occurs at low energy 350-200 cm^{-1}, which is not observed here [106]. Ni-N stretching also cannot be judged from this spectra, from the literature, it should be at around 565 - 532 cm^{-1} [107].

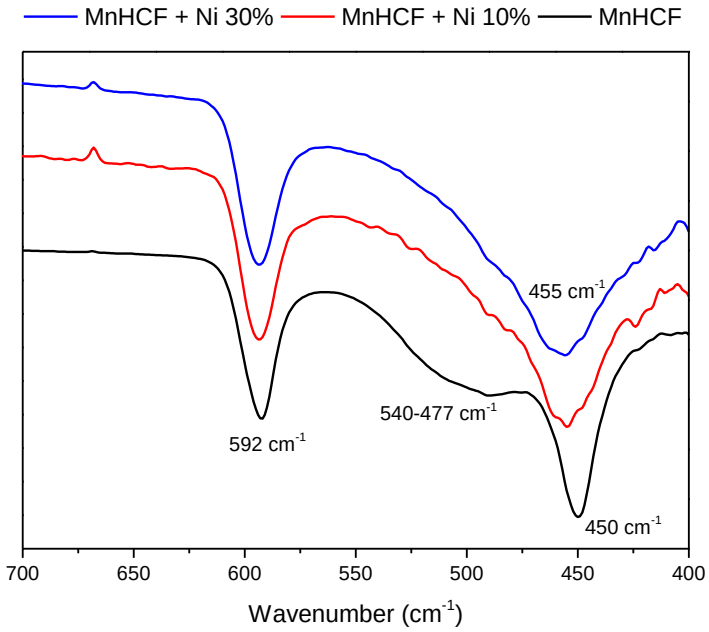

Figure 26. IR spectra region 700-400 cm -1 of MnHCF, MnHCF + Ni 10% and MnHCF + Ni 30% (normalized)

Sharp absorptions at 1620 and 3533 cm^{-1} in the IR spectra of MnHCF are associated with the O−H stretching and H−O−H bending modes arising from interstitial water, and the peak at 3604 cm^{-1} is characteristic of free surface water (non-hydrogen bonded) [108, 109, 99]. In case of Ni

addition there is practically same results in case of interstitial water. However, there is a shift of 12-13 cm^{-1} for the surface water signal. Also after second metal addition low intensity signals are appearing at 1217, 1366 and 1738 cm^{-1}. At present no clear evidence for the assignment of these peaks but probable they are due to the Ni interacting with water molecules in different crystallographic positions.

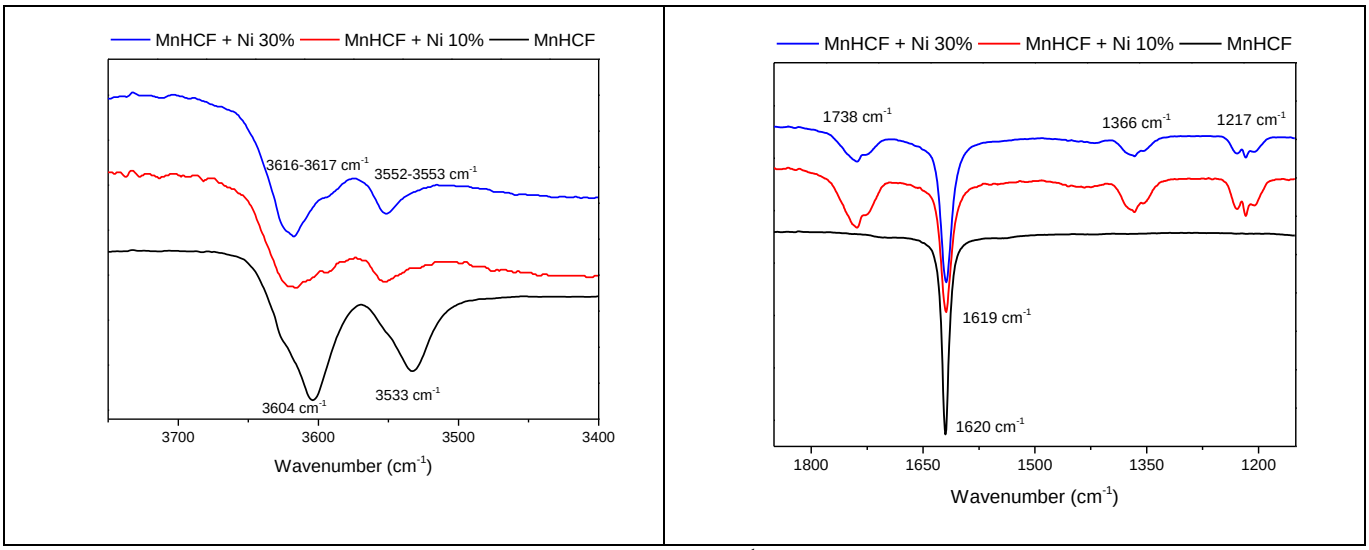

Figure 27. IR spectra region (normalized) 3750-3400 cm^{-1} of MnHCF, MnHCF + Ni 10% and MnHCF + Ni 30% (left) and 1850-1150 cm^{-1} (right).

3. PXRD Analysis

Powder X-ray diffraction data of the synthesized samples are as follows:

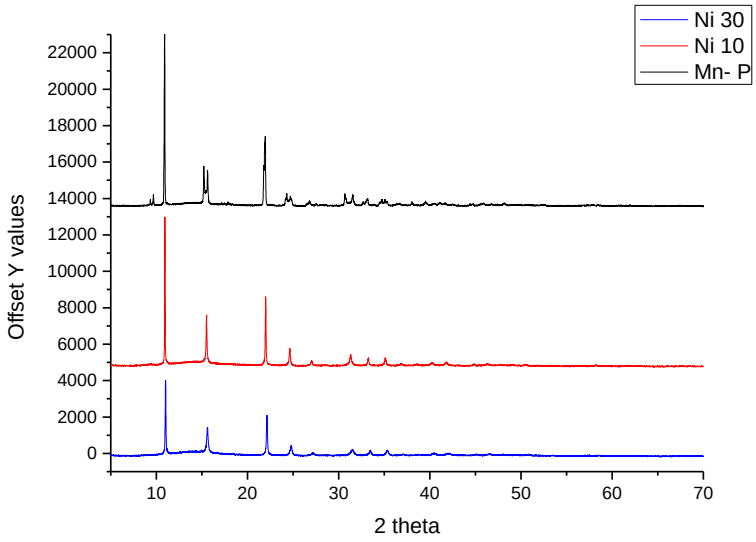

Figure 28. PXRD measurment data of MnHCF, 10% Ni doped MnHCF and 30% Ni doped MnHCF

Some differences inside the spectra can be seen directly:

- Two signals at 9.34˚ and 9.69˚ are observed only in pure MnHCF;
- Two signals in MnHCF at 15.21˚ and 16.61˚, whereas there is only one for samples with Ni at 15.51˚ for 10% addition and 16.61˚ for 30%;
- MnHCF peak at 21.95˚ has two shoulders, nickel doped samples have only single peaks (at 22.00˚ and 22.13˚ for 10% and 30% of Ni addition respectively);
- Two signals for pure MnHCF at 24.29˚ and 24.69˚, only one centered at 24.63˚ for 10% and 24.69˚ and 30% Ni containing samples;
- Two signals for pure MnHCF at 26.79˚ and 25.55˚, only one centered at 27.02˚ for 10% and 27.17˚ and 30% Ni containing samples;
- Two signals for pure MnHCF at 30.68˚ and 31.54˚, only one centered at 31.30˚ for 10% and 31.53˚ and 30% Ni containing samples;
- Three signals for pure MnHCF at 32.67˚, 33.17˚ and 33.87˚, only one centered at 33.26˚ for 10% and 33.46˚ and 30% Ni containing samples.

From these differences it is clear that the structure of the pure MnHCF sample is different of those with the nickel addition. On the other hand Ni containing samples have quite similar structure, but from the zoomed image it is evident that, there is a shift observed towards higher angles, with increasing the concentration of nickel.

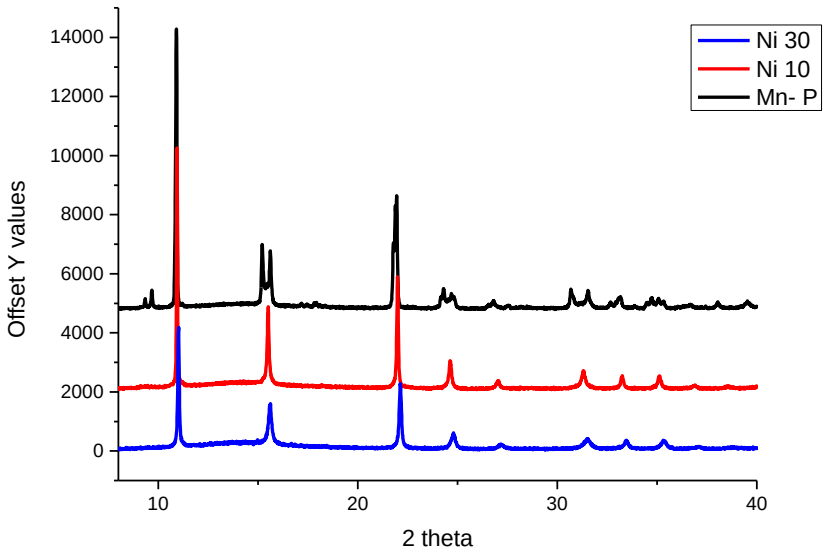

Figure 29. PXRD measurment data zoomed from 8° to 40°. MnHCF, 10% Ni doped MnHCF and 30% Ni doped MnHCF

PXRD measurement results were further treated with FullProf Suite software. Prior to the actual sample refinement, for the measurement calibration Si standard was used. As a peak shape was used Pseudo-Voigt Axial divergence asymmetry and as a background - linear intercalation between set background points. After refining shape, asymmetry, FWHM and instrumental parameters of Si standard (space group Fd-3m), which was taken from the NIST database, the wavelength was corrected from 1 Å to 0.9997 Å.

At first, the pure MnHCF was refined. The space group is P 21/n. The initial data about the possible atomic positions was taken from the literature [110]. Afterwards, parameters were refined step by step.

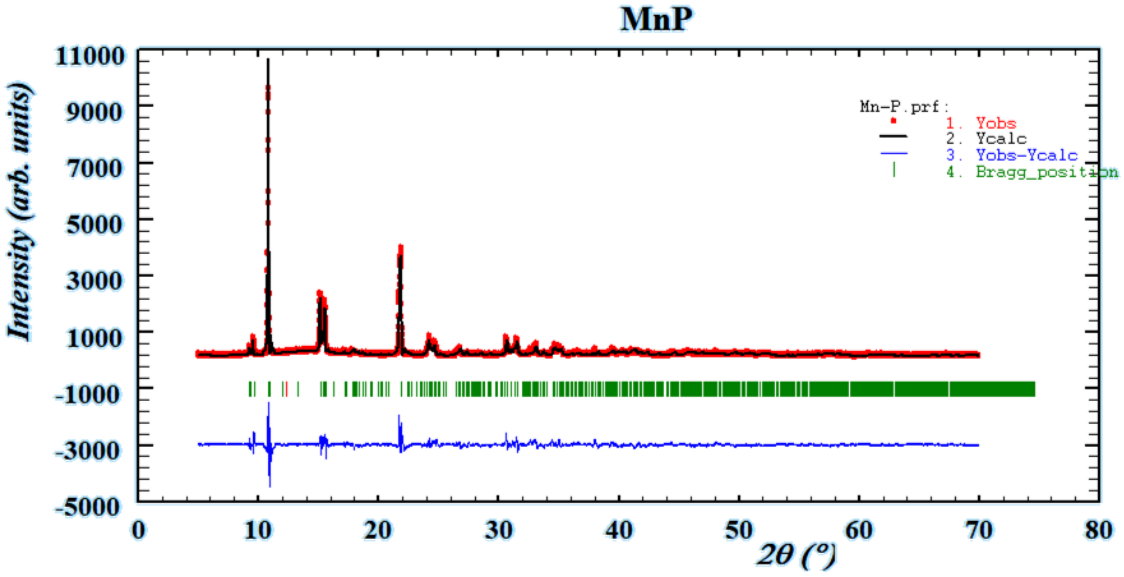

Figure 30. MnHCF refinement with Rietveld method

The final unit cell parameters and the goodness of the fit are presented in the table:

Table 9. MnHCF unit cell parameters and the goodness of the FullProf refinement

Symmetry operations	x, y, z x, -y, -z -x+½, y+½, -z+½ x+½, -y+½, z+½			
a / Å	10.5567			
b / Å	7.4757			
c / Å	7.4084			
β / deg	92.141			
Cell volume / $Å^3$	584.258			
Bragg R-factor	23.7			
Rf-factor	28.6			
Conventional Rietveld: Rp, Rwp, Re and χ^2	41.1	21.0	689	0.9304E-03
χ^2(Bragg contribution)	0.936E-03			

Atomic positions in case of manganese and iron was fixed to 2b positions, to (½; ½; ½) and (½; 0; 0) respectively. For other elements the positions were refined. As it is monoclinic cell, for the nitrogen and carbon three different positions were taken. Oxygen atom from the water molecules was also included inside the structure during the refinement.

Table 10. MnHCF atomic coordinates inside the unit cell

Atom label	**Coordinates**			**Wyckoff site position**
	X	**Y**	**Z**	
Mn1	0.5 (fixed)	0.5 (fixed)	0.5 (fixed)	2b
Fe1	0.5 (fixed)	0.0 (fixed)	0.0 (fixed)	2b
N1	0.52819	0.35053	0.70026	4e
N2	0.29596	0.49594	0.51416	4e
N3	0.52337	0.28730	0.27170	4e
C1	0.44653	0.21594	0.77885	4e
C2	0.24006	0.52979	0.54584	4e
C3	0.46199	0.14237	0.13755	4e
O1	0.26126	0.21609	0.29242	4e
Na1	0.26760	0.46816	0.03297	4e

After the MnHCF, Ni containing samples were refined. The same P 21/n model was tried, but it was not suitable. From the literature, neutron diffraction pattern of $K_{2x/3}Cu[Fe(CN)_6]_{2/3}\cdot nH_2O$ was reported to be a cubic cell, space group Fm-3m [111]. For the indication of the occupation of the unit cell stoichiometric ratios from the MP-AES and TGA experiments were used (with considering corresponding multiplicity). Several different positions were tried for the oxygen atom (32f, 192l), finally being refined on 24e position. The refinement procedure was done on both measurements with the acquisition time of 1s/step and longer ones - 3s/step.

Table 11. MnHCF + 10% Ni unit cell parameters and the goodness of the FullProf refinment

Symmetry operations	x, y, z; -x, -y, z; -x, y, -z; x, -y, -z; z, x, y; z, -x, -y; -z, -x, y; -z, x, -y; y, z, x; -y, z, -x; y, -z, -x; -y, -z, x; y, x, -z; -y, -x, -z; y, -x, z; -y, x, z; x, z, -y; -x, z, y; -x, -z, -y; x, -z, y; z, y, -x; z, -y, x; -z, y, x; -z, -y, -x; -x, -y, -z; x, y, -z; x, -y, z; -x, y, z; -z, -x, -y; -z, x, y; z, x, -y; z, -x, y; -y, -z, -x; y, -z, x; -y, z, x; y, z, -x; -y, -x, z; y, x, z; -y, x, -z; y, -x, -z; -x, -z, y; x, -z, -y; x, z, y; -x, z, -y; -z, -y, x; -z, y, -x; z, -y, -x; z, y, x; x, ½+y, ½+z; -x, ½-y, ½+z; -x, ½+y, ½-z; x, ½-y, ½-z; z, ½+x, ½+y; z, ½-x, ½-y; -z, ½-x, ½+y; -z, ½+x, ½-y; y, ½+z, ½+x; -y, ½+z, ½-x; y, ½-z, ½-x; -y, ½-z, ½+x; y, ½+x, ½-z; -y, ½-x, ½-z; y, ½-x, ½+z; -y, ½+x, ½+z; x, ½+z, ½-y; -x, ½+z, ½+y; -x, ½-z, ½-y; x, ½-z, ½+y; z, ½+y, ½-x; z, ½-y, ½+x; -z, ½+y, ½+x; -z, ½-y, ½-x; -x, ½-y, ½-z							
	Accusation time 1s/step				Accusation time 3s/step			
a / Å	10.4778				10.4724			
Cell volume / $Å^3$	1150.2975				1148.5315			
Bragg R-factor	42.6				36.1			
Rf-factor	72.7				58.7			
Conventional Rietveld: Rp, Rwp, Re and χ^2	151	27.1	950	0.8121E-03	63.0	31.0	968	0.1022E-02
χ^2(Bragg contribution)	0.856E-03				0.108E-02			

The atomic coordinates are as follows:

Table 12. MnHCF + 10% Ni atomic coordinates inside the unit cell

Atom label	**Coordinates**			**Occupation**	**Wyckoff site position**
	X	**Y**	**Z**		
Fe	0 (fixed)	0 (fixed)	0 (fixed)	2.48	4a
Mn	0.5 (fixed)	0.5 (fixed)	0.5 (fixed)	3.8	4b
Ni	0.5 (fixed)	0.5 (fixed)	0.5 (fixed)	0.2	4b
C	0.06995 (1s/step) 0.07022 (3s/step)	0 (fixed)	0 (fixed)	89.28	24e
N	0.38890 (1s/step) 0.46212 (3s/step)	0 (fixed)	0 (fixed)	89.28	24e
Na	0.25(fixed)	0.25 (fixed)	0.25 (fixed)	9.68	8c
O	0.23263 (1s/step) 0.24987 (3s/step)	0 (fixed)	0 (fixed)	88.8	24e

Same treatment was done for the 30% Ni doped sample. Unit cell parameter and cell volume decreased, compare to the sample, which contained 10% of nickel.

Table 13. MnHCF + 30% Ni unit cell parameters and the goodness of the FullProf refinment

Symmetry operations	x, y, z; -x, -y, z; -x, y, -z; x, -y, -z; z, x, y; z, -x, -y; -z, -x, y; -z, x, -y; y, z, x; -y, z, -x; y, -z, -x; -y, -z, x; y, x, -z; -y, -x, -z; y, -x, z; -y, x, z; x, z, -y; -x, z, y; -x, -z, -y; x, -z, y; z, y, -x; z, -y, x; -z, y, x; -z, -y, -x; -x, -y, -z; x, y, -z; x, -y, z; -x, y, z; -z, -x, -y; -z, x, y; z, x, -y; z, -x, y; -y, -z, -x; y, -z, x; -y, z, x; y, z, -x; -y, -x, z; y, -x, -z; -y, x, -z; -x, -z, y; x, -z, -y; x, z, y; -x, z, -y; -z, -y, x; -z, y, -x; z, -y, -x; z, y, x; x, ½+y, ½+z; -x, ½-y, ½+z; -x, ½+y, ½-z; x, ½-y, ½-z; z, ½+x, ½+y; z, ½-x, ½-y; -z, ½-x, ½+y; -z, ½+x, ½-y; y, ½+z, ½+x; -y, ½+z, ½-x; y, ½-z, ½-x; -y, ½-z, ½+x; y, ½+x, ½-z; -y, ½-x, ½-z; y, ½-x, ½+z; -y, ½+x, ½+z; x, ½+z, ½-y; -x, ½+z, ½+y; -x, ½-z, ½-y; x, ½-z, ½+y; z, ½+y, ½-x; z, ½-y, ½+x; -z, ½+y, ½+x; -z, ½-y, ½-x; -x, ½-y, ½-z							
	Accusation time 1s/step				Accusation time 3s/step			
a / Å	10.4036				10.4089			
Cell volume / $Å^3$	1126.0471				1127.7527			
Bragg R-factor	59.5				37.6			
Rf-factor	75.8				64.8			
Conventional Rietveld: Rp, Rwp, Re and χ^2	222	30.1	0.152E+04	0.3924E-03	147	28.6	0.102E+04	0.7863E-03
χ^2(Bragg contribution)	0.396E-03				0.790E-03			

As it is shown in the tables, for both cases – 10% and 30% of nickel addition in MnHCF, the difference between the accusation time of the measurements give the difference only in the thousandths place and in the cell volume, the variation is less than 2 $Å^2$.

The atomic coordinates of 30% containing nickel sample is shown in the table below:

Table 14. MnHCF + 30% Ni atomic coordinates inside the unit cell

Atom label	**Coordinates**			**Occupation**	**Wyckoff site position**
	X	**Y**	**Z**		
Fe	0 (fixed)	0 (fixed)	0 (fixed)	2.80	4a
Mn	0.5 (fixed)	0.5 (fixed)	0.5 (fixed)	3.48	4b
Ni	0.5 (fixed)	0.5 (fixed)	0.5 (fixed)	0.52	4b
C	0.07824 (1s/step) 0.12157 (3s/step)	0 (fixed)	0 (fixed)	100.80	24e
N	0.36080 (1s/step) 0.39811 (3s/step)	0 (fixed)	0 (fixed)	100.80	24e
Na	0.25(fixed)	0.25 (fixed)	0.25 (fixed)	13.36	8c
O	0.22897 (1s/step) 0.25394 (3s/step)	0 (fixed)	0 (fixed)	81.84	24e

From the atomic coordinates, it is visible, that both nickel containing samples have same structure, with the small decrease of the volume in 30% Ni.

4. XAS Analysis

In **XANES** part of X-ray absorption spectroscopy spectra, for the K edges of all three elements, pre-edge structure was observed, which means that, despite the fact, that Mn, Ni and Fe are in octahedral environment, they are not perfectly centro symmetric.

In Fe pre-edge region a single transition around 7114 eV is the dipole forbidden but quadrupole allowed 1s-3d transition [112], Fe^{II} sixfolded coordinated to the C-end of cyanide ligands and it is expected to be found in its low spin state (LS-Fe^{II}) with a $t_{2g}^6e_g^0$ electron configuration and spin multiplicity S = 0.

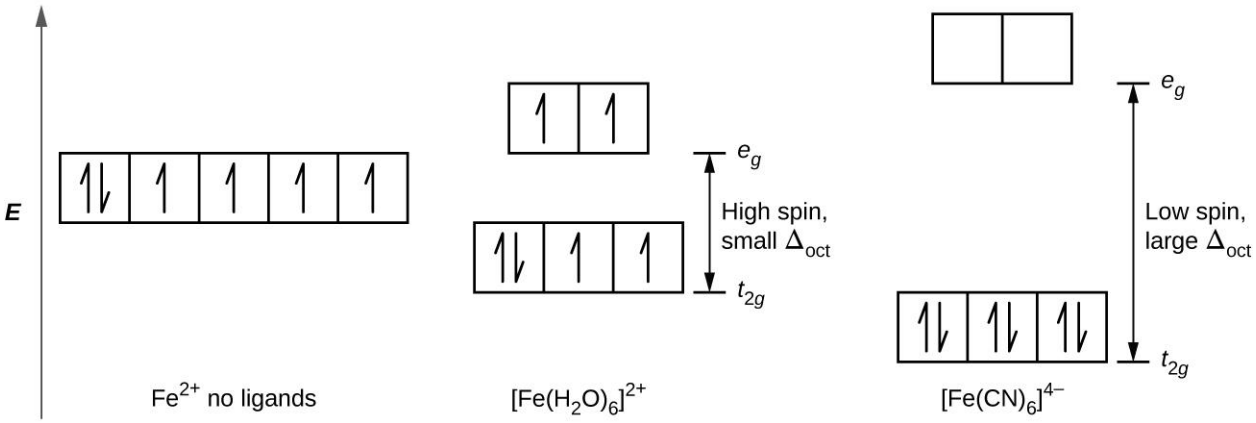

Figure 31. Fe^{II} electronic configuration of 3d orbitals [113]

Consequently, the only one possible transition is expected to the 3d-eg orbitals ≈7114 eV. Transitions occurring at higher energies, >7115 eV, arise from normally forbidden dipole transitions to the empty bound states that reflect longer-range effects of the shells beyond the cyanides [114, 115, 116].

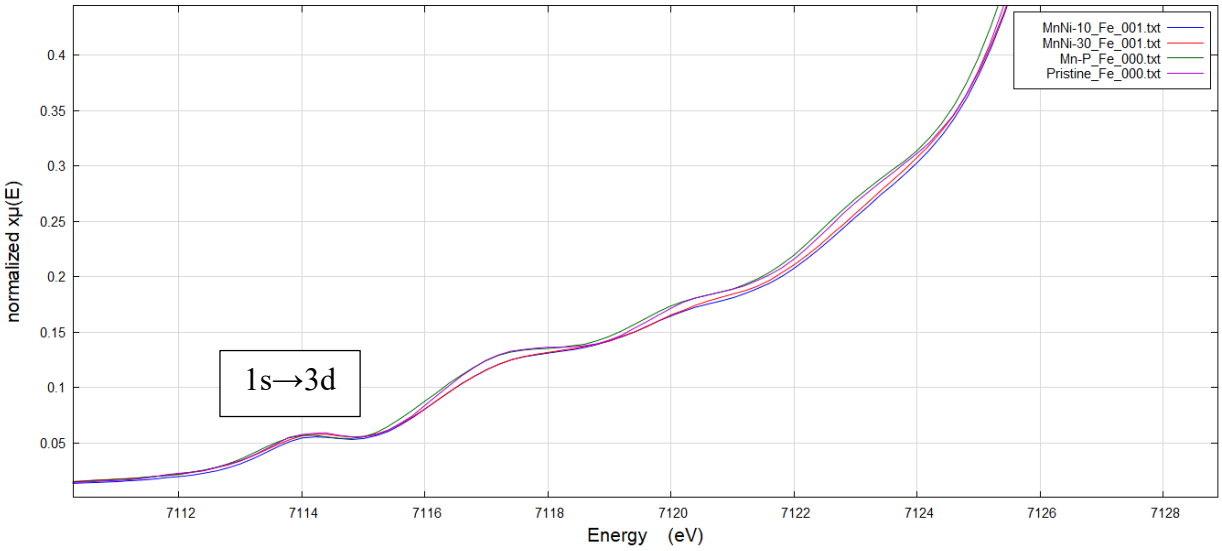

Figure 32. Fe K-edge Pre-edge structure

In overall, Ni doping does not cause major changes in the pre-edge structure. All synthesized samples have 1s→3d transition on the same energy. In other transitions, above 7115eV, MnHCF spectrum is very similar to Pristine. The last transition feature in the rising portion of the edge at 71123.2 eV is not observed in nickel doped samples at all. Generally, the intensity of absorbance is lowest in case of 10% addition of Ni, but the difference is very small.

Table 15. Fe K-edge pre -edge structure

Pristine		MnHCF		MnHCF + Ni 10%		MnHCF + Ni 30%	
Energy (eV)	Absorption (normalized)	Energy (eV)	Absorption (normalized)	Energy (eV)	Absorption (normalized)	Energy (eV)	Absorption (normalized)
7114.4	0.059	7114.2	0.057	7114.2	0.056	7114.2	0.058
7117.4	0.133	7117.4	0.132	7117.6	0.128	7117.6	0.128
7120.4	0.181	7120.4	0.181	7120.4	0.172	7120.4	0.174
7123.2	0.270	7123.2	0.270	-	-	-	-

Manganese in MnHCF has high spin (HS) Mn^{2+}, d^5 configuration [31]. It is in the octahedral environment, six-folded coordinated to the N-end of cyanide ligands. Spin multiplicity is S=½; 2S+1=2 possible transitions: to t_{2g} or e_g. In the pre-edge region of the K-edge can be observed the transitions that occur from the 1s core level to the 3d/4p orbitals.

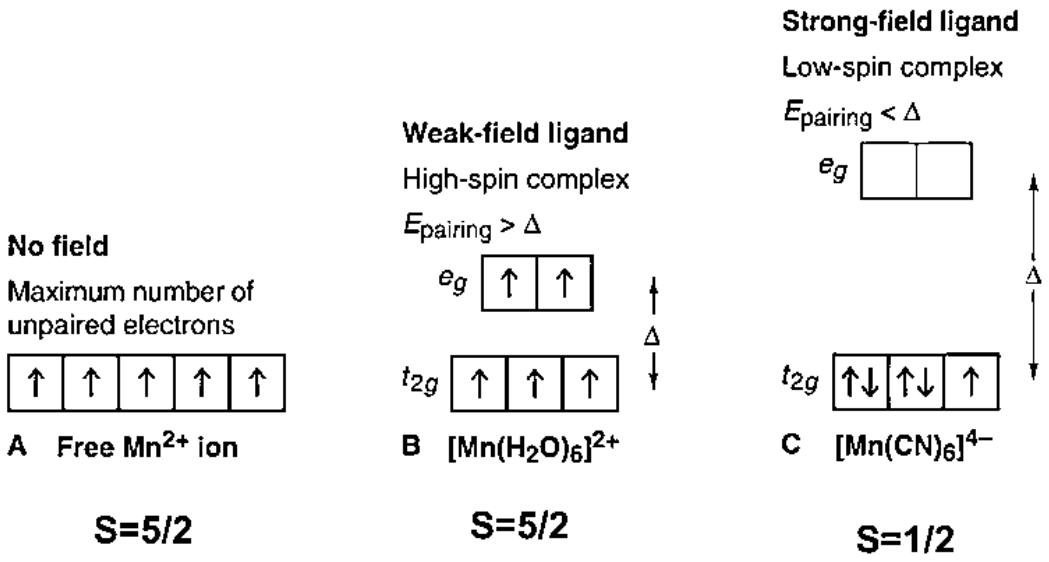

Figure 33. Mn^{II} electronic configuration of 3d orbitals

In pre-edge part of XAS spectra of synthesized samples there are two peaks, that are considered to be the transitions on 3d, in the t_{2g}/e_g [117] at ≈6540 eV and 4p orbitals at ≈6546 eV.

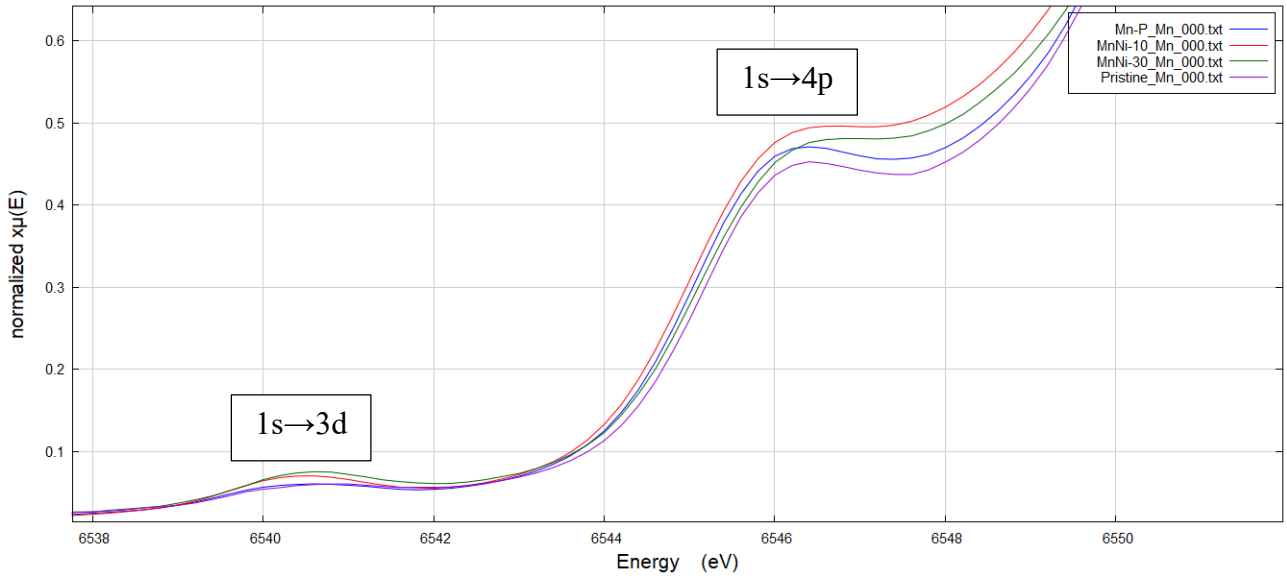

Figure 34. Mn K-edge pre -edge structure

In all synthesized samples have 1s→3d transition on the same energy, slightly shifted towards lower energy than the same transition peak in pristine. 1s→4p transition peak is observed in the same energy in synthesized MnHCF and pristine, difference between them and Ni doped samples is very small.

Generally, the intensity of absorbance is higher in samples with nickel, especially in 1s→3d transition, but the difference is still quite small.

Table 16. Mn K-edge pre -edge structure

Transition	Pristine		MnHCF		MnHCF + Ni 10%		MnHCF + Ni 30%	
	Energy (eV)	Absorption (normalized)	Energy (eV)	Absorption (normalized)	Energy (eV)	Absorption (normalized)	Energy (eV)	Absorption (normalized)
1s→3d	6541	0.0604	6540.6	0.0605	6540.6	0.0701	6540.6	0.0752
1s→4p	6546.4	0.4525	6546.4	0.4709	6546.6	0.4935	6546.6	0.4756

Nickel in Ni doped MnHCF has high spin (HS) Ni^{2+}, d^8 configuration. S=1; 2S+1=3. It is in the octahedral environment, as Ni is partially substituting Mn inside the structure of MnHCF, the environment is the same: six-folded coordinated to the N-end of cyanide ligands.

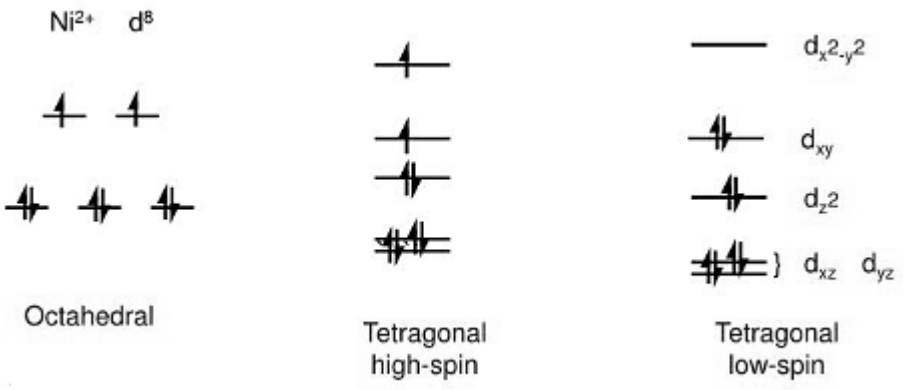

Figure 35..Ni^{II} electronic configuration of 3d orbitals in the crystal field

In the pre-edge region of the K-edge can be observed the transitions that occur from the 1s core level to the 3d/4p orbitals. Around ≈8333 eV 1s→3d transition peak is observed, whereas 1s→4p peak is approximately ≈8341 eV

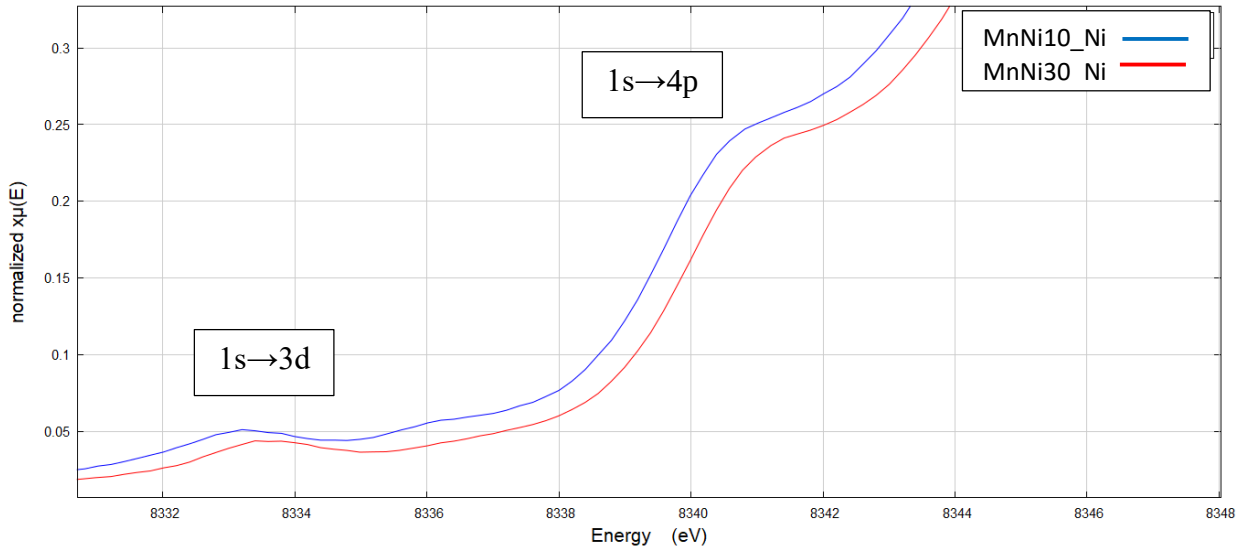

Figure 36. Ni K-edge pre -edge structure

The pre-edge structure has quite similar pattern also in case of Ni K-edge. However, 10% addition of Ni has small shift towards the lower energy compare to 30% of Ni of 0.2 eV and 0.6 eV for 1s→3d and 1s→4p transitions, respectively. Also sample with 10% content of nickel has a little bit higher intensity in both transitions.

Table 17. Ni K-edge pre -edge structure

Transition	MnHCF + Ni 10%		MnHCF + Ni 30%	
	Energy (eV)	Absorption (normalized)	Energy (eV)	Absorption (normalized)
1s→3d	8333.2	0.0514	8333.4	0.0441
1s→4p	8340.8	0.247	8340.4	0.241

Iron K-edge edge jump is quite similar in all samples. The shift is around ≈0.2 eV and it is centered at ≈7130 eV. The intensity is not varying a lot either and is a little bit lower for Ni-doped samples. In overall, the addition of the second metal has not influenced the oxidation state of Fe.

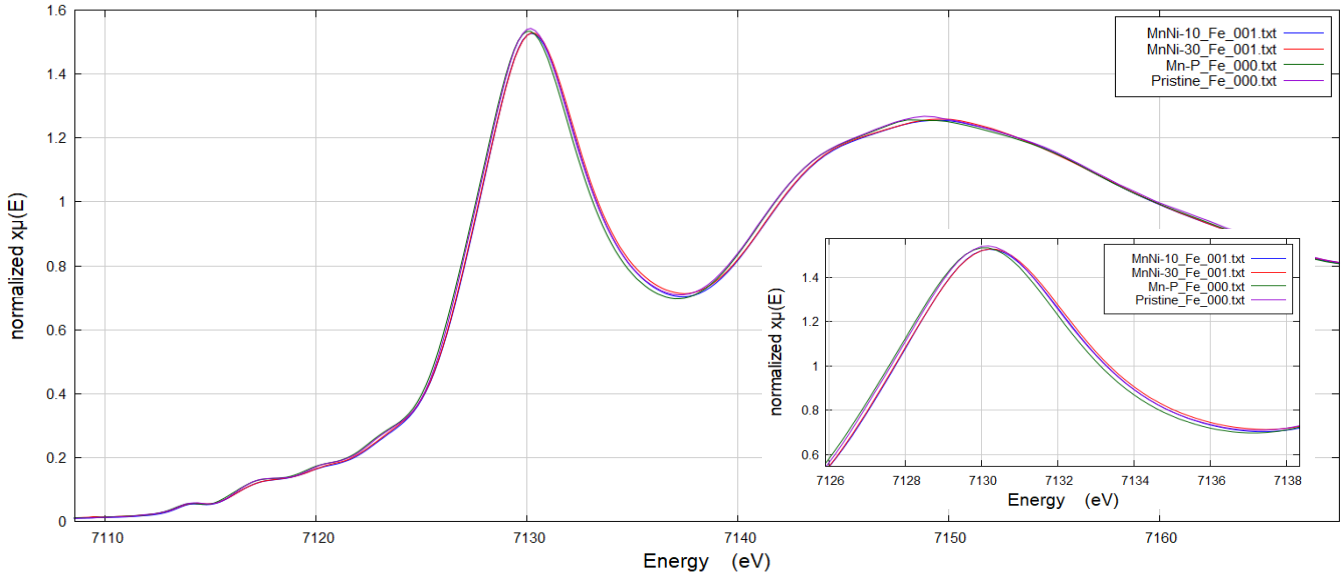

Figure 37. XANES spetrum of Fe K-edge, zoom at peak maximum

Difference in XANES spectra is also small for Mn K-edge. They are centered at ≈ 6553.2 eV, except 30% Ni doped sample, which is slightly shifter to higher energy, ≈ 6553.4 eV. More significant changes are observed in case of absorption intensity. Addition of nickel decreases the height of the peak.

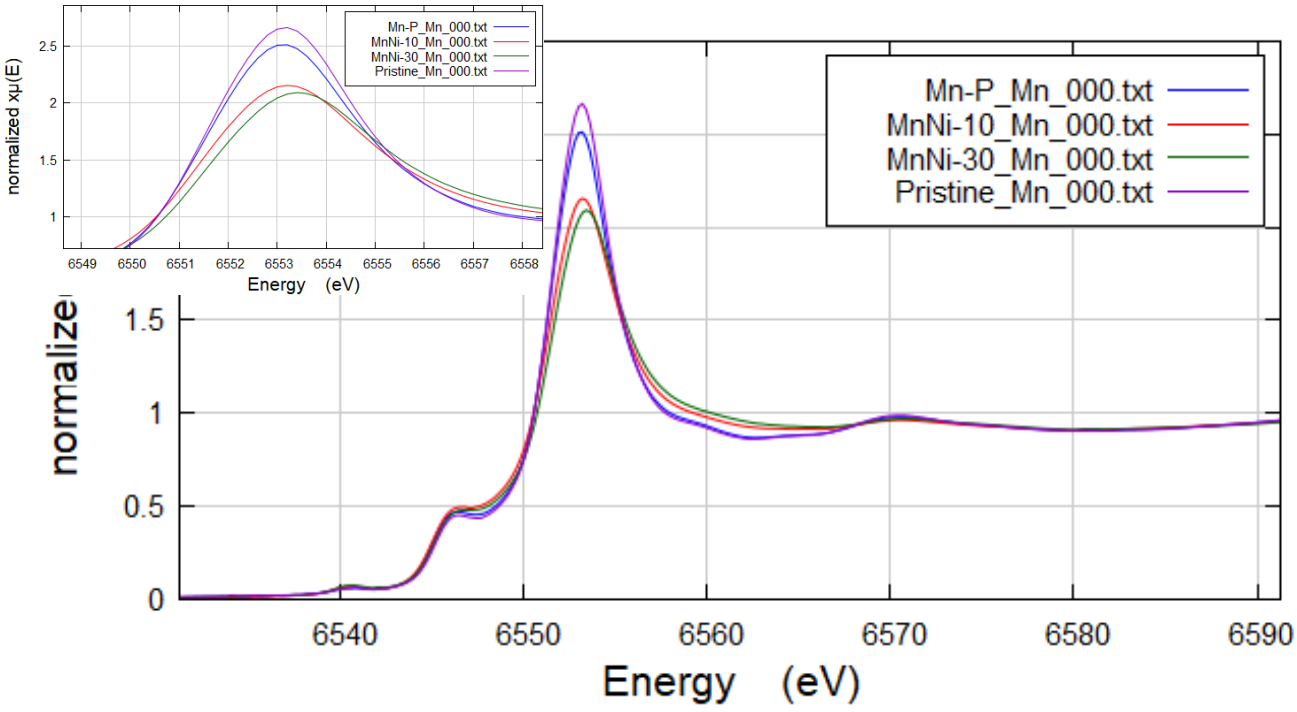

Figure 38. XANES spectrum of Mn K-edge, zoom at edge maximum

In case of Ni, 30% addition causes the shift of edge jump towards the higher energies by 0.4 eV, compare to 10% of nickel, also intensity has decreased. Shift towards the higher energies generally means the increase of the oxidation state. In this analysis peak maximum is centered at approximately ≈8349.2 – 8349.6 eV for Ni 10% and Ni 30% respectively.

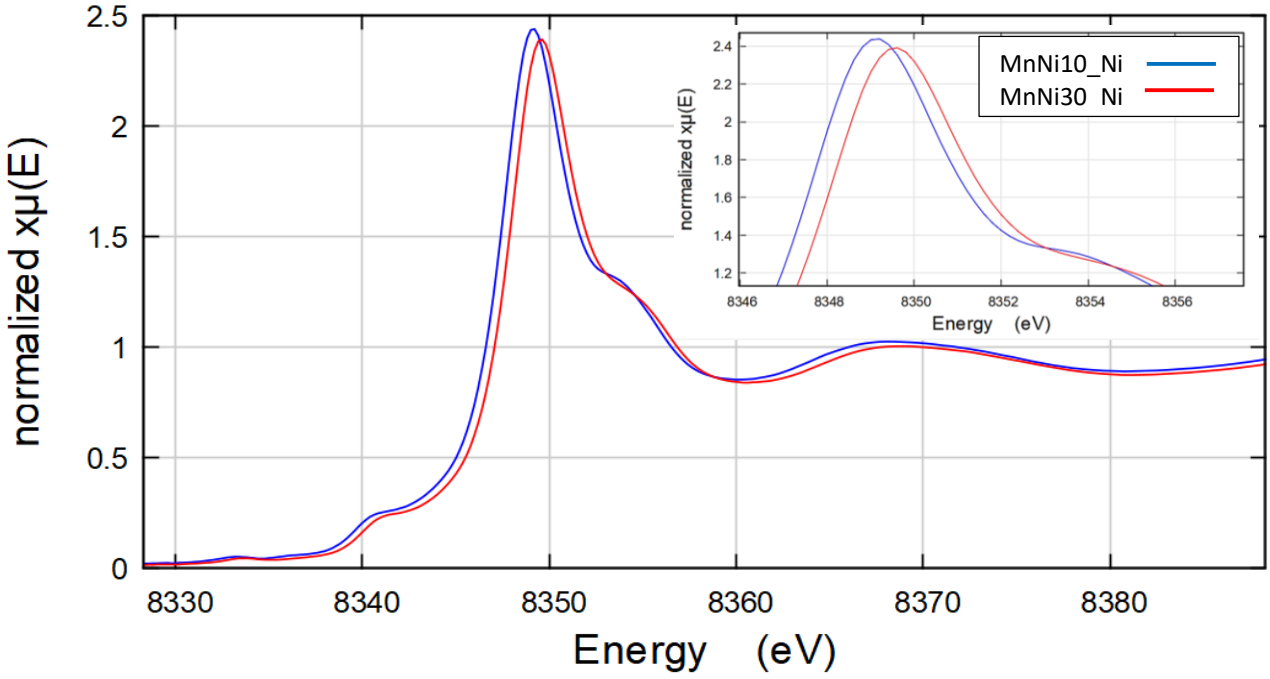

Figure 39. XANES spectrum of Mn K-edge, zoom at edge maximum

The **EXAFS** part of the XAFS spectra gives a relevant structural information of the local coordination site around the metals. The analysis have been conducted using the GNAXS program [118, 119] which takes into account the multiple scattering formalism (MS) and allows a direct comparison of the experimental spectra to a theoretical one. The method used the decomposition of the EXAFS signals into a sum of several contributions, namely, the n-body terms. The theoretical signal was calculated ab initio and contained the relevant two-body γ(2), three-body γ(3), and four-body γ(4) MS terms [120]. The two-body terms were associated with pairs of atoms and probed their distances and variances. The three-body terms were associated with triplets of atoms and probe angles, and bond–bond and bond–angle correlations. The four-body terms were associated with chains of four atoms, and probe distances and angles in-between, and bond–bond and bond–angle correlations. However, since Fe-C-N-Mn chains featured angles in-between close to 180°, the actual number of parameters used to define the γ(3) or the γ(4) peaks was reduced by symmetry.

Experimental EXAFS signals were compared to the theoretical model, which was built up based on the previous published literature on a similar material [110].

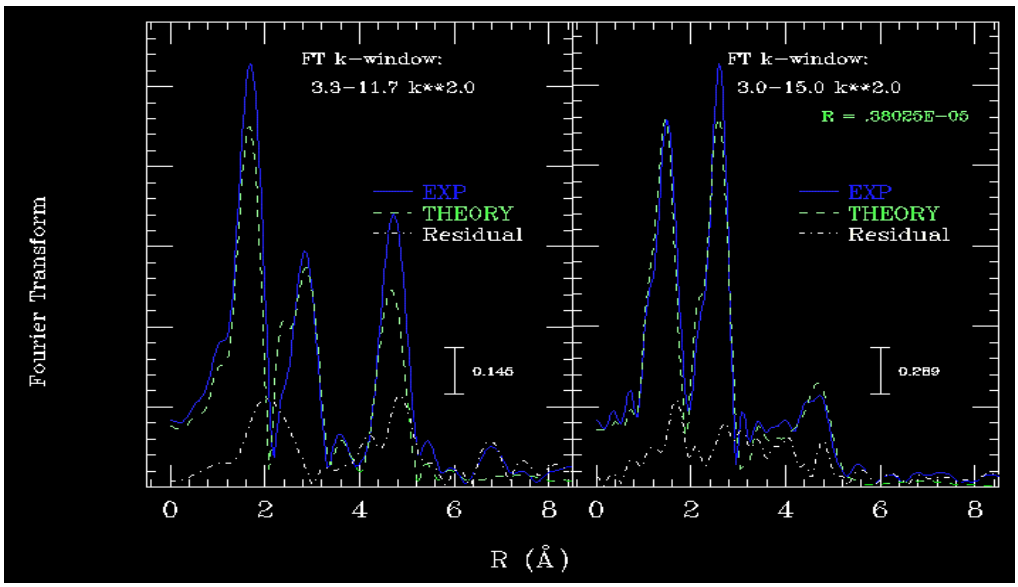

Figure 40. Preliminary EXAFS data analysis, for the MnHCF, Furie Transform curves of Mn (left) and Fe (right)

Based on the preliminary fitting, there is a good match between the two curves, which confirms the accuracy of this structural model. On the left side of the image, on Mn FT curve the first signal corresponds to N, the second to C and the third to the iron. The same way with Fe FT, the first peak correspond to C, second to N and third to Mn.

Table 18. Structural parameters of pure MnHCF, MnHCF + Ni 10% and MnHCF Ni 30% , obtained by EXAFS preliminary firritng procedurea

	MnHCF	MnNCF + Ni 10%	MnGCF + Ni 30%	Model (from literature [110])
Fe-C / Å	1.874	1.876	1.876	1.876
σ^2 Fe-C / Å^2	0.0025	0.0023	0.0024	0.003
C≡N / Å	1.182	1.179	1.179	1.183
σ^2 C≡N / Å^2	0.010	0.0095	0.010	0.010
Mn-N / Å	2.182	2.153	2.122	2.18
σ^2 Mn-N / Å^2	0.0068	0.0095	0.011	0.0065
beta (asym)		0.53	0.007	

Bond length Fe-C is not changing by Ni doping of the sample. C≡N bond length is also almost same, which represent, that carbon-nitrogen bond is very stable and stiff and consequently the local structure near iron is not changing. On the other hand, the bond length Mn-N is gradually reducing with the increase of Ni content. Corresponding Debye-Waller factors confirm added that Mn site gets more distorted and even asymmetry parameter for the Mn-N pair distribution (deviation from a Gaussian) needs to be added.

Na was not included in primary refinement, according to the first approximation, because from the both metals it should have distance more than 4 Å, which is too large number for the single scattering

It worth to mention, that following the XRD data, nickel in this model has been put in the same position as Mn. From the calculations on Fe side, it looks correct. As an additional check, the Fourier Transform of the experimental K2-extracted EXAFS data taken at the K-edge of Ni can be used. As displayed in the figure below, three main peaks, corresponding to the N, C and Fe scatters are obvious. They arises from the Ni-N-C-Fe structural framework.

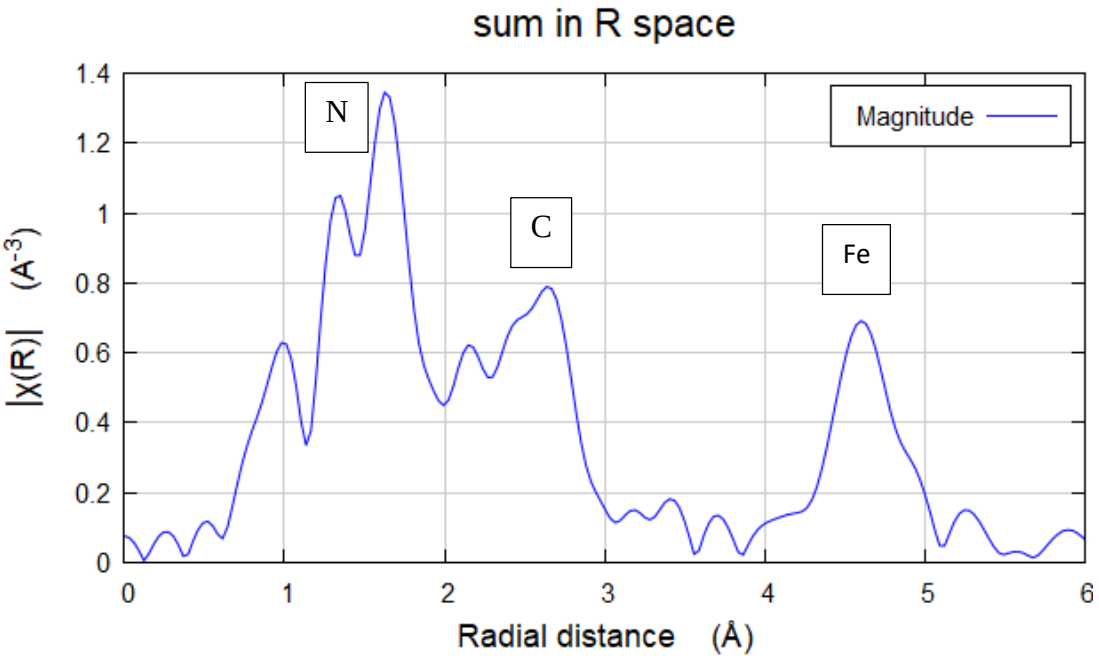

Figure 41. Fourier Transform of the experimental K2-extracted EXAFS data at the K-edge of Ni

5. Cathode material after cycling

5.1. 2D XRF Analysis

In 2D XFR measurements, MnHCF sample was probed, which was synthesized previously similar way, as the samples discussed within this work. In case of pristine sample, obtained spectra both regions show identical spectrum to the cumulative (total) spectrum.

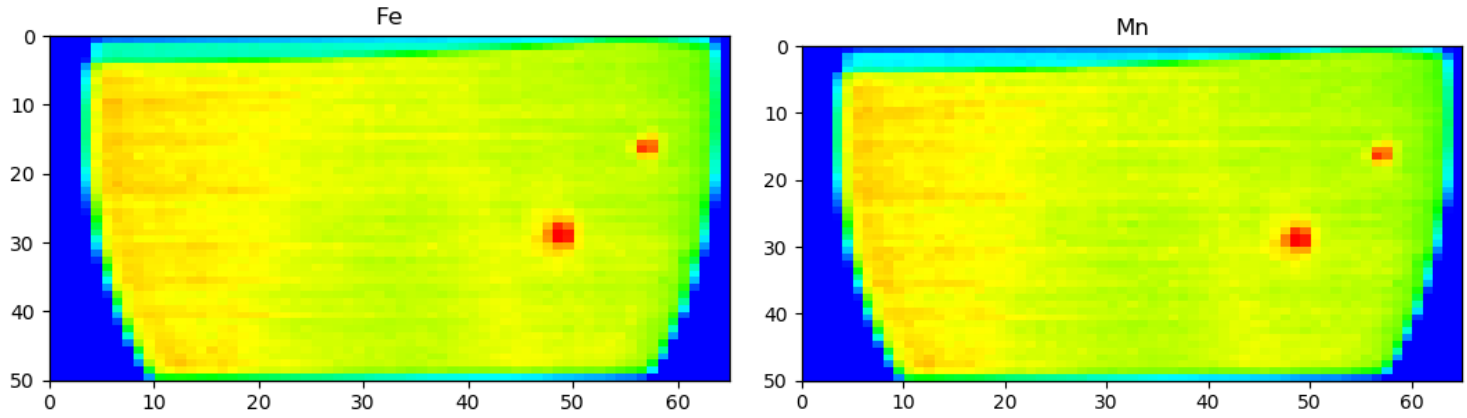

Figure 42. 2D image of Pristine sample, Fe (on the left) and Mn (on the right), energy 7200eV

Same for the Li containing charged sample after 50 cycles. From the analysis done at 7200 eV, there is almost no difference in spectra.

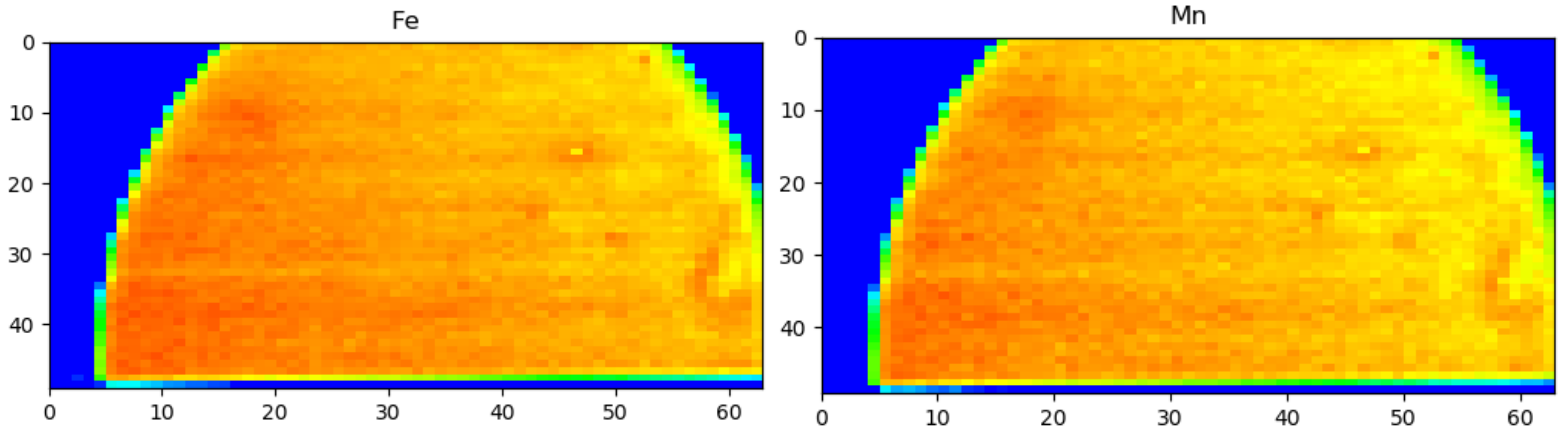

Figure 43. 2D image of LiFC20 sample, Fe (on the left) and Mn (on the right), energy 7200eV

The spectra was also checked in the right part of the sample, where some inhomogeneities are observed, but there was no actual difference between the spectral patterns of those compared to the overall spectrum.

For the further measurements the energy was shifted to 6553 eV. The reason for changing the energy was the increase of the contribution of the reduced species of manganese. Oxidized Mn is shifted towards the higher energy and consequently in 6553 eV the contribution of oxidized manganese is much lower, compared to the reduced one.

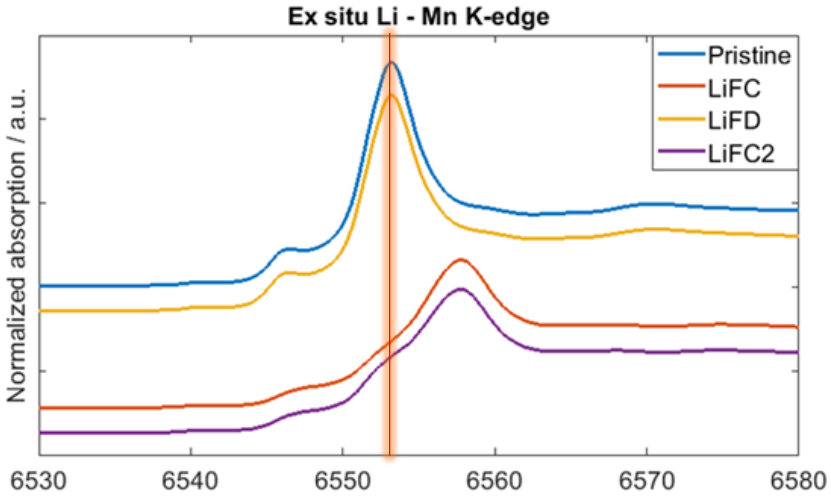

Figure 44. K-edge of the Mn in the oxidized (charged: LiFC and LiFC2) and reduced (Pristine and LiFD) samples [110]

For Pristine, there was no difference observed, after moving from 7200 eV to 6553 eV, as was expected. On the other hand, for the LiFC50, there was observable a changed in the image.

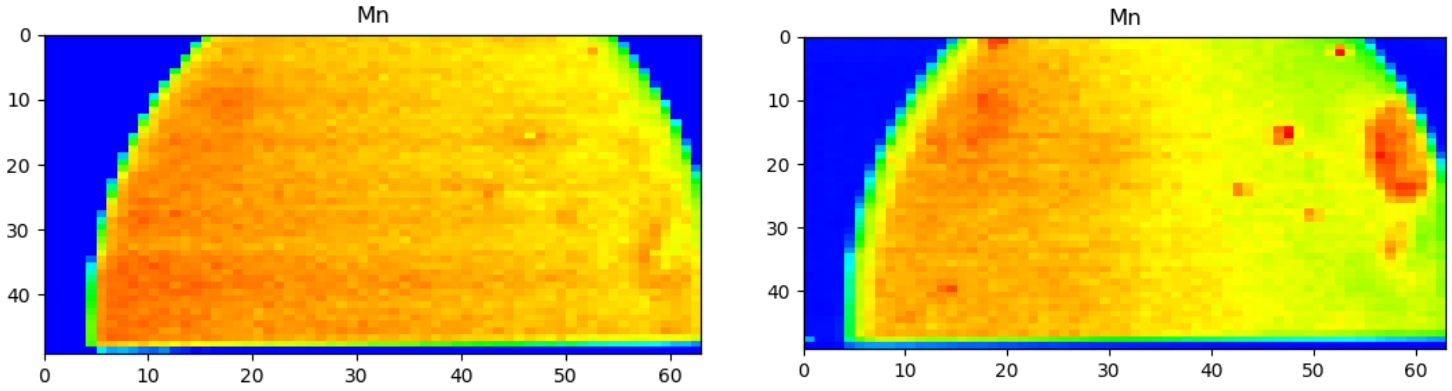

Figure 45. LiFC20 images measured at 7200 eV (left) and 6553 eV (right)

However the actual XRF spectrum from the region on the right side part was not different from the average spectrum of the sample.

Generally, from the analysis using 6553 eV energy, it was evident that manganese species distribution is changing during the cycling.

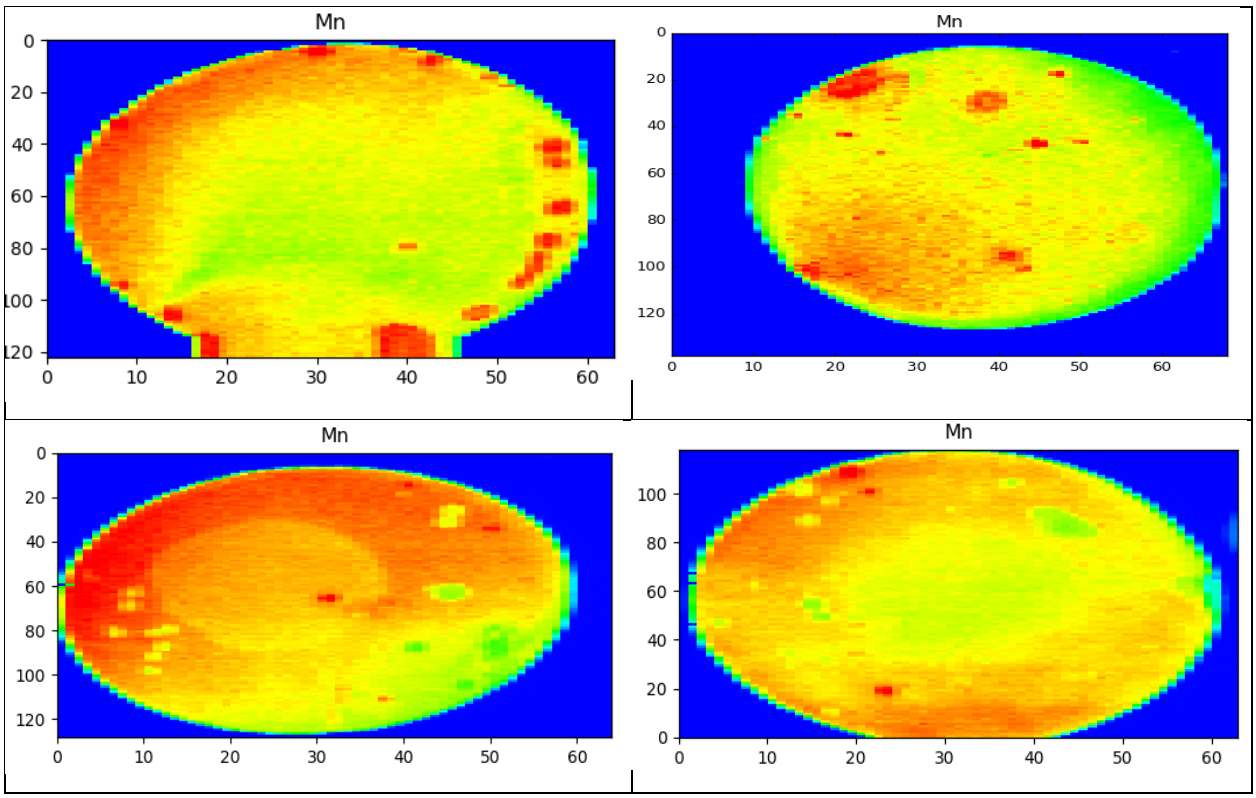

Figure 46. Logarithm scale data of LiCF (upper left), LiCF20 (upper right), LiFD (down left) and LiFD20 (down right)

For understanding more details, the XAS spectrum was taken. From the XANES part of the spectrum, there were some variations observed. As it is already visible from the images, LiFD is the most homogenous sample, regarding to the Mn species. XANES spectrum confirmed the same. Charged sample has "red" areas, mostly in the peripheral part of the sample, XANES spectra also shows that in those discrete regions of high absorption values manganese is more reduced, which is confirmed by the edge shift towards the lower energy, as reported in the literature [110].

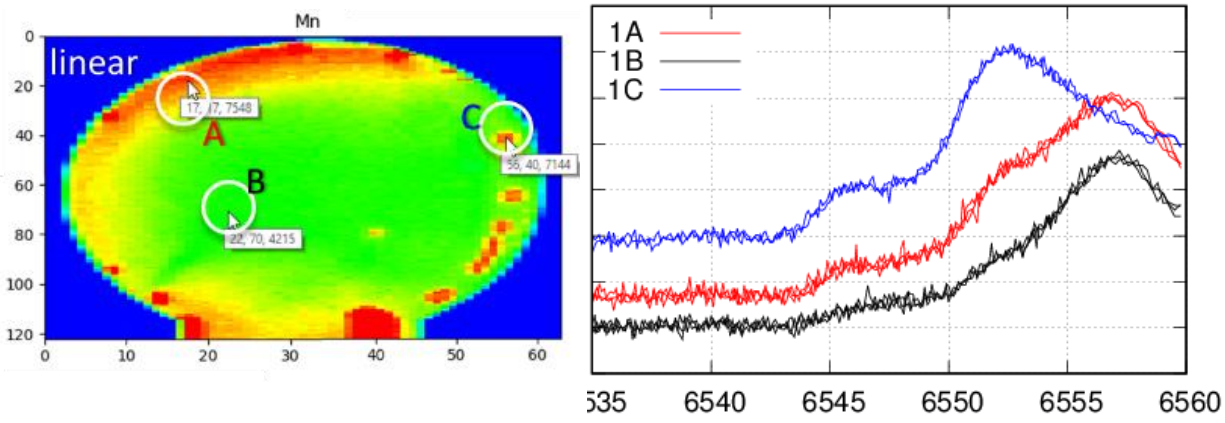

Figure 47. LiFC and corresponding XANES spectra

More inhomogeneous distribution is visible in the cycled samples: in LiFD20 the red spectra of the A region, is more reduced, compare to the region B and C, which is characteristic to the charged sample.

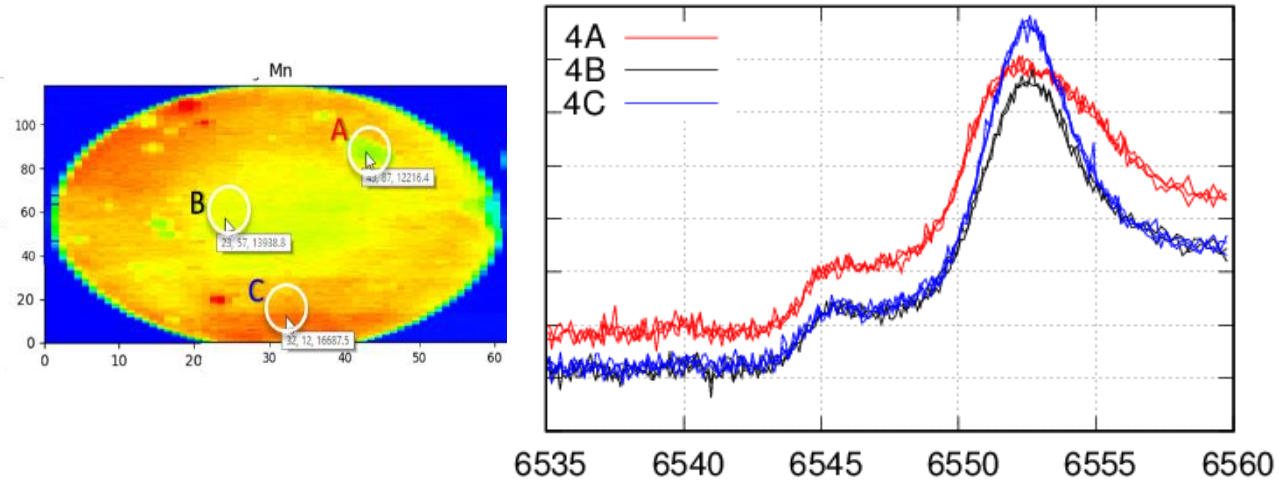

Figure 48. LiFD20 and corresponding XANES spectra

Most inhomogeneities are observed in case of charged cycled sample. Here the blue and red spectra, which corresponds the C and A regions, respectively, have similar shape, but the intensity is different and there is a shift. The spectrum from the B region (black line) is shifted toward the lower energy, its shape is different from other two and the pre-edge structure is also more intense. From the simple comparison of these measurements to the data, it can be concluded that area C, which is in the "greener" area, corresponds to mostly oxidized species of Mn, whereas "B" shows the pattern of the discharged sample. Area which is signed as A, has the spectrum between "B" and "C", but with its pattern still looks more like the reduced sample.

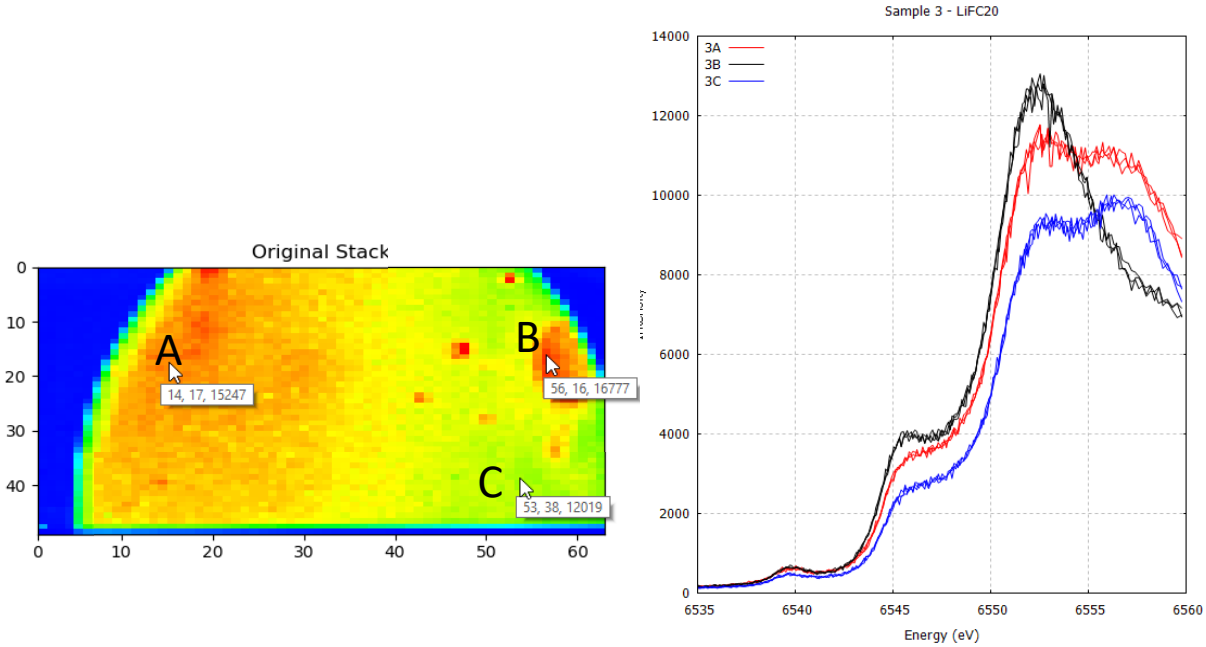

Figure 49. LiFC20, measured at 6553 eV and Mn K-edge XANES spectrum

2D XRF analysis is very useful technic for the characterization of the materials and monitoring of the different species during the charging/discharging cycles. The measurement showed, that during cycling discharges (charged) species of manganese started to appear in the charged (discharged) samples. However LiFC20 had less homogenous distribution than LiFD20. Reduced species in the charged sample is appearing mostly in the peripheral parts of the sample.

5.2. TXM Analysis

Analysis of transmission soft X-ray microscopy was performed on pure MnHCF samples, similar to the above discussed samples, but from the previous batch of synthesis. L edge of Mn and Fe and K edge of the N of the pristine, charged and discharged sample, after one and fifty cycles.

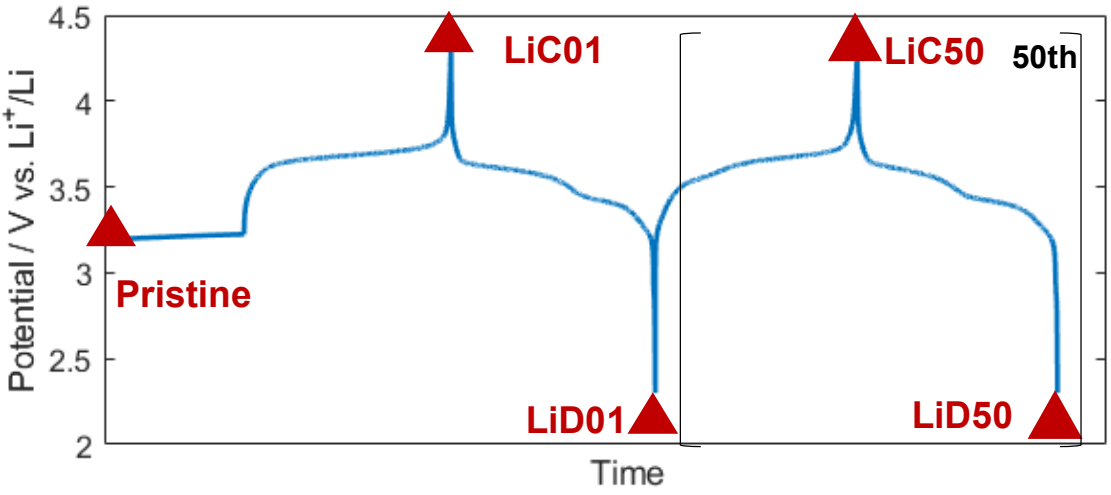

Figure 50. Scheme of charge/discharge cycling process of the material

As it is known from the literature, Fe experiences strong crystal field and is bound to σ-donor and π-acceptor C-end, consequently it is in low spin state, octahedral environment. On the other hand, Mn experiences moderate crystal field and is bound to σ-donor N-end and it is high spin state, also octahedral environment [121].

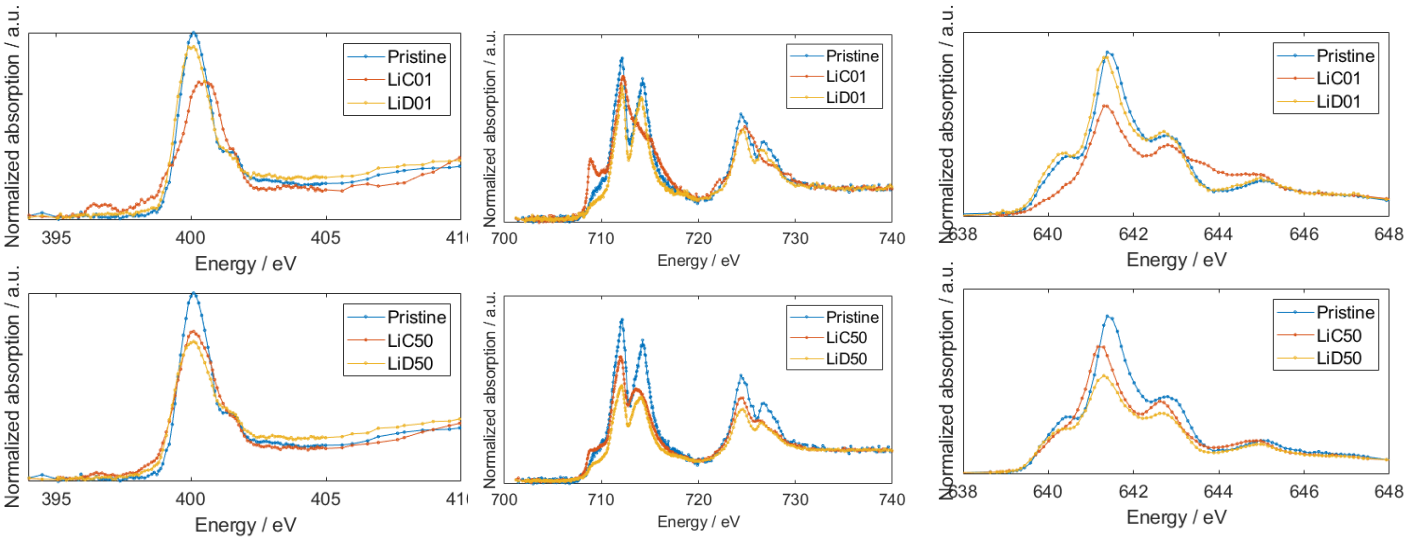

Figure 51. Spectra of N edge (left), Fe edge (middle) and Mn edge (right)

Generally, in the nitrogen edge, the transition at 397 eV appears only in the charged state. It can be associated to the transition occurring from N 1s to the hybridized state with Fe(III) 3d t_{2g}. The transition involves a state with high metal character, so it has low intensity [122].

In iron edge, there are several transitions observed: at approximately 709eV 2p → 3d t_{2g}, which is only visible for Fe(III); the most intense signal at around 712 eV, corresponding to the transition 2p → 3d e_g, that is occuring in case of both Fe(III) and Fe(II): Fe(III) low spin $3d^5$ ($t_{2g}^5 + e_g^0$) and Fe(II) low spin $3d^6$ ($t_{2g}^6 + e_g^0$); and the peak near 714 eV characteristic to the π-backdonation 2p → π*(CN)-3d(metal with t_{2g} symmetry), it is also visible for both Fe(III) and Fe(II), but back-donation is generally stronger in case of Fe(II). Same transitions from $2p_{½}$ (L2 edge) are visible in higher energy (725-727 eV) [123].

For Mn edge, the transition just above 640 eV is appearing only in charged samples for Mn(II) and is not any longer visible after the oxidation (Mn(III)).

For each sample and for each edge these 3 peaks were chosen. From the stack of images, near those peak maxima, 3 consecutive images have been averaged up. Apart of the peaks, for the further treatment of the results, 10 slices have been averaged as pre-absorption and 10 slices as post-edge region.

Table 19. Energies of the peaks in different edges

Edges	Peak A (eV)	Peak B (eV)	Peak C (eV)
N	396	400	401
Fe	708	712	714
Mn	640	641	643

For the correct assessment of the results, series of treatment have been done to the images obtained by measurement. There are two main points - the signal should be coming from the active material itself and not from the carbon or binder; and for the quantification the obtained intensities should be reliable, not affected by the saturation.

To check the presence of another absorbing materials rather than the MnHCF, "Peak subtracted the pre-absorption" image overlay with "pre-absorption" images was used. The explanation behind this treatment is the fact, that in the pre-absorption part, signal is coming from both carbon and selected element, but near the edge, the absorbance of the element is raising, whereas the absorbance of the carbon stays approximately the same. So, by the subtraction the "pre-absorption" from the "peak", the result image shows only element contribution on the absorbance, free from other materials influence. By overlapping the result image to pre-absorption image, the highlighted part can be helpful in finding exactly this contribution. It can also be confirmed by the corresponded spectra of the highlighted regions. These regions were mostly some distinct particles, randomly distributed inside the sample.

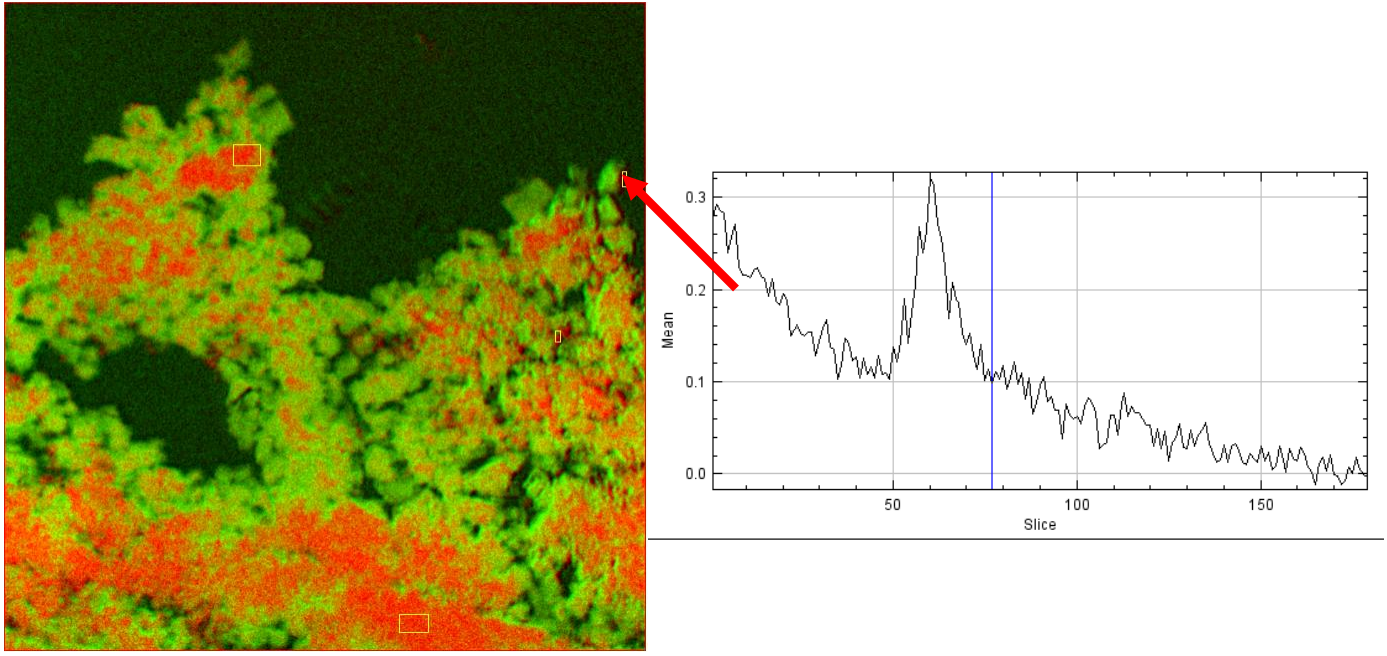

Figure 52. Identifying carbon in LiD50 sample, N edge

The saturation of the peaks has been checked with scattered plots of the peak against the pre-absorption. When the points suffer from the decline of the linearity, the results are getting doubtful. For obtaining such plots, peak image and pre-absorption image were transformed from their corresponding 1D arrays and then plotted against each other as usual xy plot.

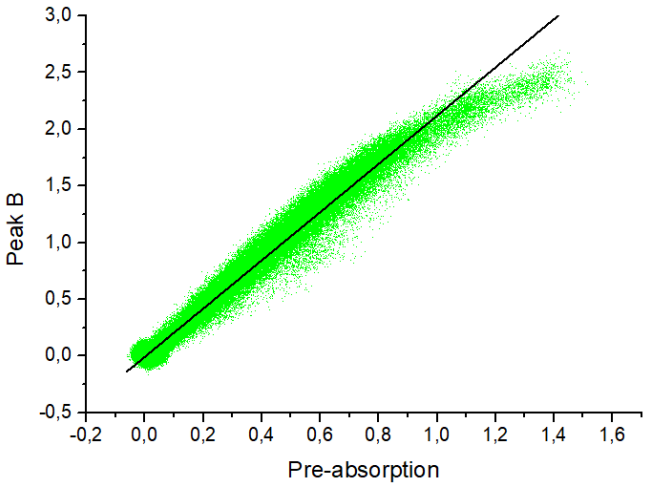

Figure 53. LiC01 Fe Peak B vs. Pre-absorption

As the scatter plot shows, when the intensity reaches up to 2, the dependence between the peak and the pre-absorption is no longer linear. This value is different for every sample, every edge and every peak, but generally Peak B was always getting saturated. Because of this reason, during the treatment more focus was made on peak A and peak C.

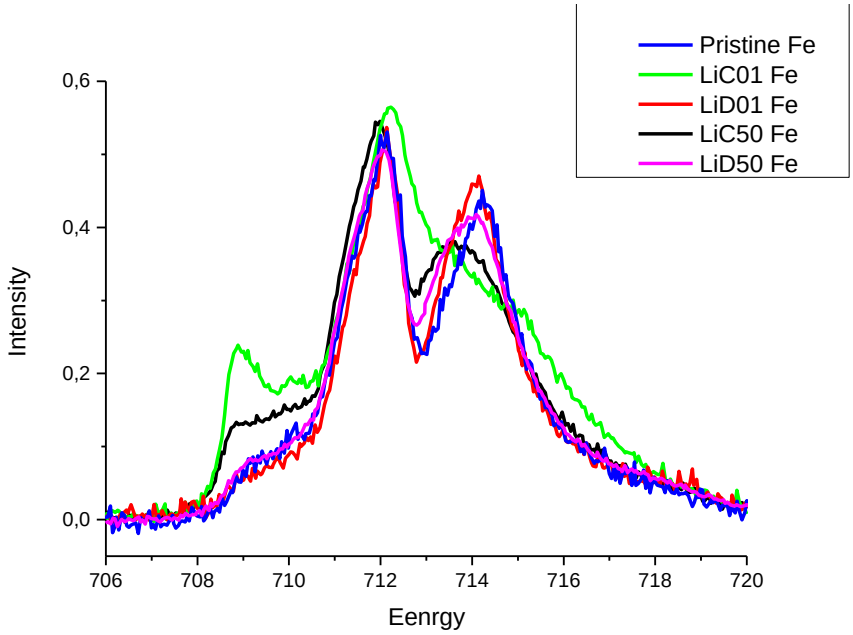

Figure 54. Average spectra of Fe edge of all samples

In iron edge as it was expected in LiC01 Fe there is intense Peak A and Peak C is visible as a slope, on the other hand, in LiD01 Fe Peak A has practically disappeared and Peak C intensity significantly increased, LiD50 Fe spectrum also looks quite similar to LiD01 Fe. But in LiC50 Fe, the spectrum is intermediate between LiC01 Fe and LiD01 Fe: there is the Peak A, but the intensity is lower than in uncycled charged sample; peak C is also visible, but less intense than in LiD01 Fe. Consequently, there is some kind of intercalation presented in cycled charged sample. Same results were obtained from the other edges.

In Mn edge there is still no peak in Peak A region, but there is a slope in LiC50 Mn sample. Also there is a shift in peak B from pristine to samples, with maximum shift in lower energy in LiC50 Mn.

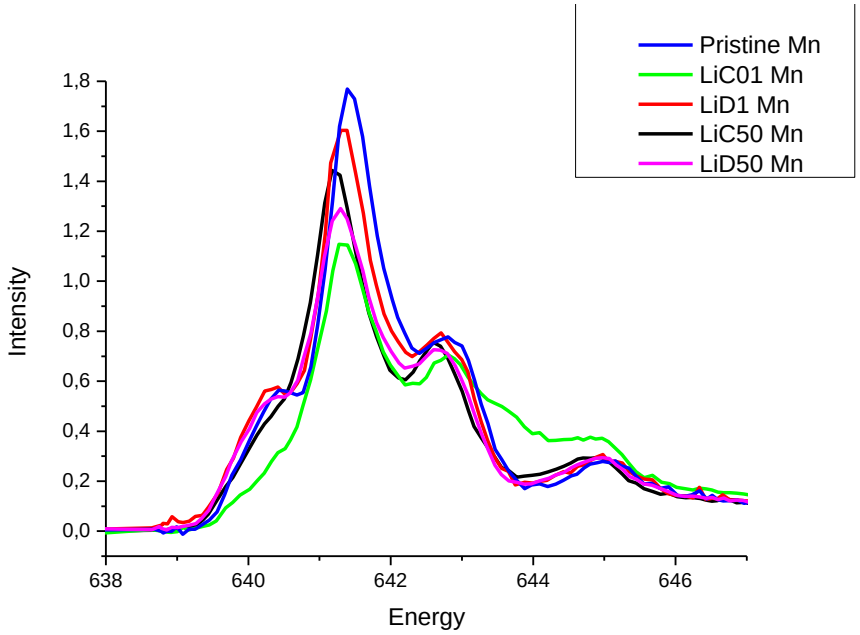

Figure 55. Average spectra of Mn edge in different samples

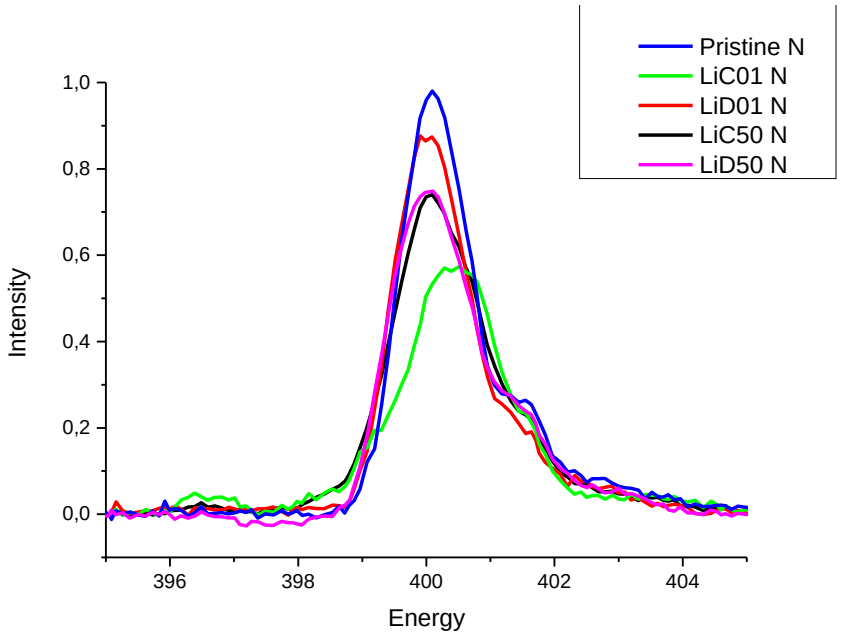

Figure 56. Average spectra of N edge in different samples

Core-shell composition difference was checked by choosing the threshold values corresponding to bulk and surface to restrict these areas. Spectra were obtained and compared.

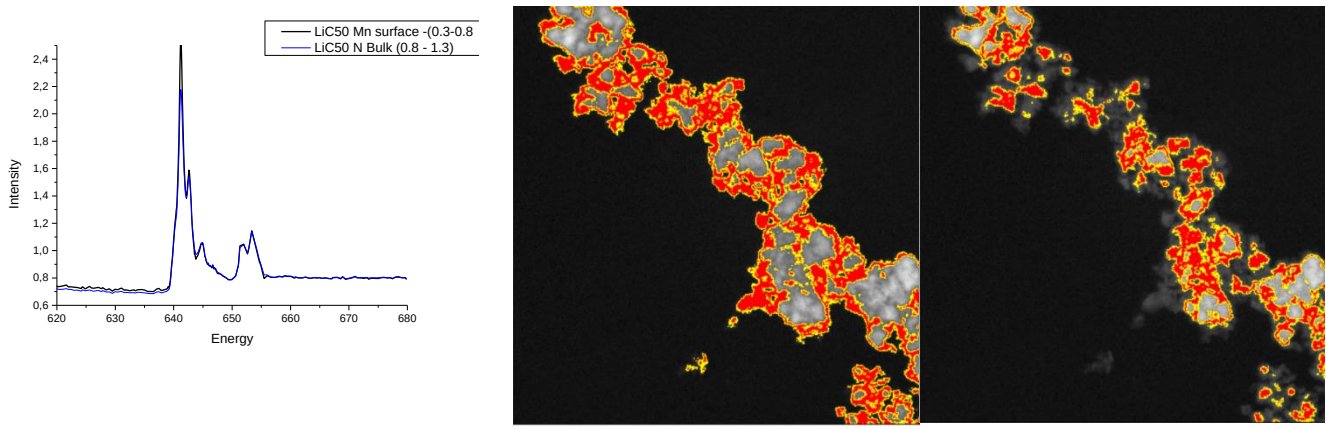

Figure 57. LiC50 Mn 0.3 - 0.8 (left), 0.8 - 1.3 (right) and the corresponding spectra

The spectra looked quite similar, which means that there is no core-shell effect. But it does not necessarily grant the homogeneity. As peak A is the most sensitive in all edges, the ratio Peak A/Peak C was extensively studied to localize spectral variations. From the ratio maps, the inhomogeneities inside the sample is evident. By the careful investigation different Peak A/Peak C, on different samples, LiC50 was chosen, as one of the

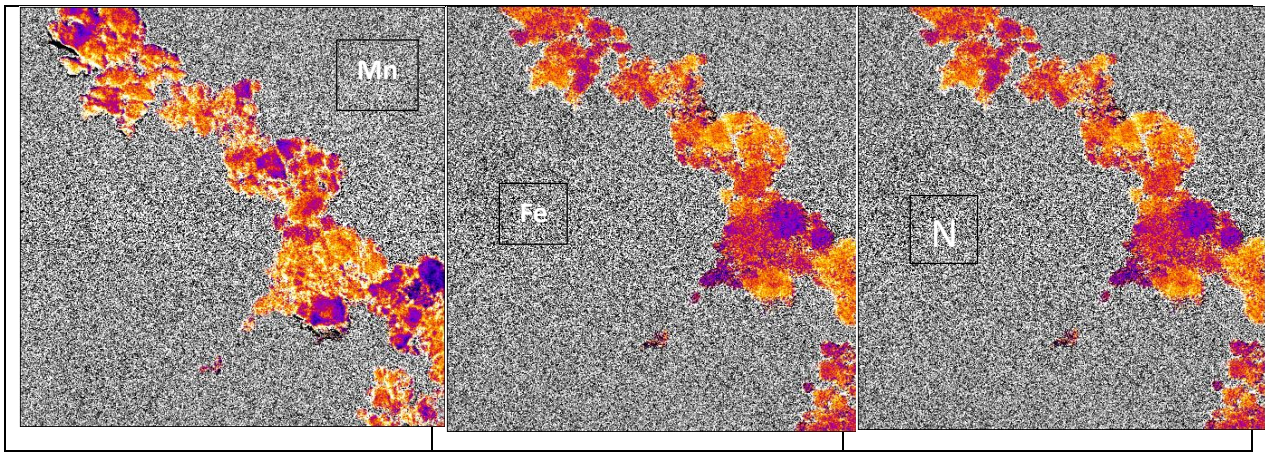

Figure 58. Ratio maps of (Peak A-pre-absorption)/(Peak C-pre-absorption) of Mn, Fe and N edges.

For dividing the sample to the regions, which might differ from one another, the scatter plots (Peak C - Pre-absorption) vs. (Peak A – Pre-absorption) were used. Pre-absorption was subtracted to the average peak spectra to avoid detecting contributions coming from not the active material. There is he linear fit line added to the scatter plot, but as it is seen, there is a significant deviation. Distribution of the points inside the scattered plot is not a perfect line. so several regions can be selected.

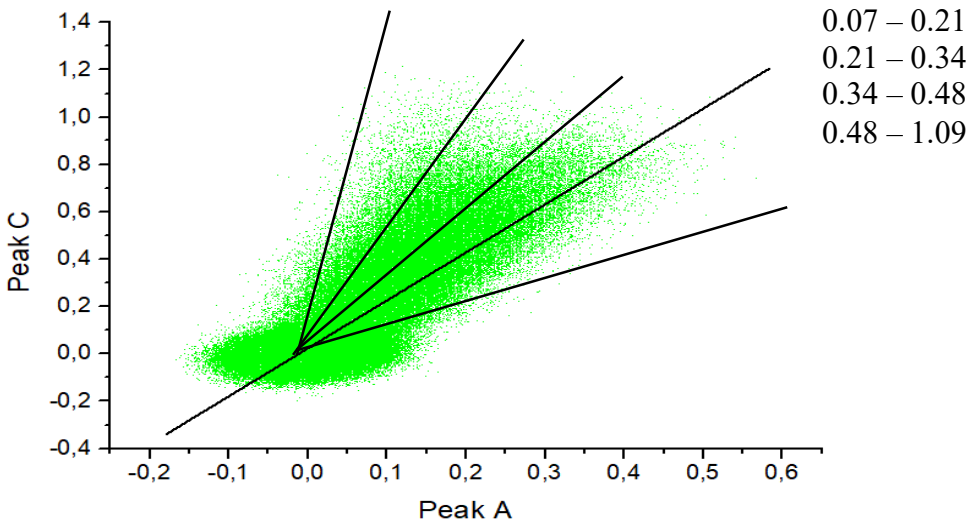

Figure 59. Scatter plot of LiC50 Fe (Peak C - Pre-absorption) vs. (Peak A – Pre-absorption) divided to four regions accordong to its deviation frp, the linear fit

From the slope of the lines, 4 threshold ranges were chosen in the (Peak C - Pre-absorption) /(Peak A – Pre-absorption) map. For each range corresponding selections and spectra were obtained. They were compared to each other and to the first cycled samples.

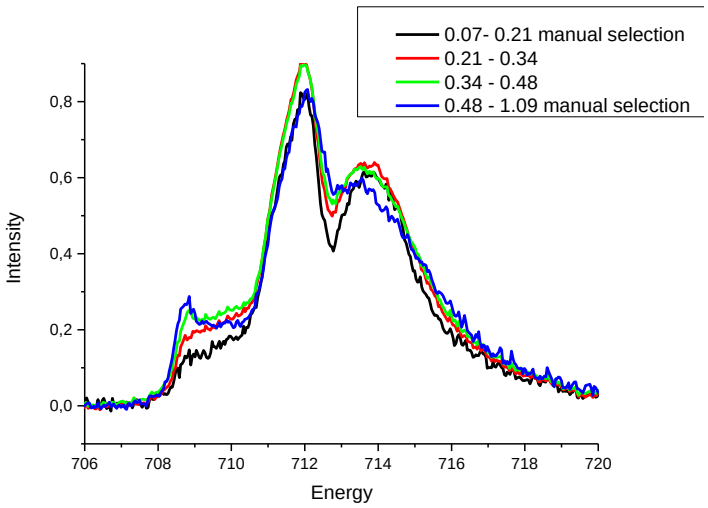

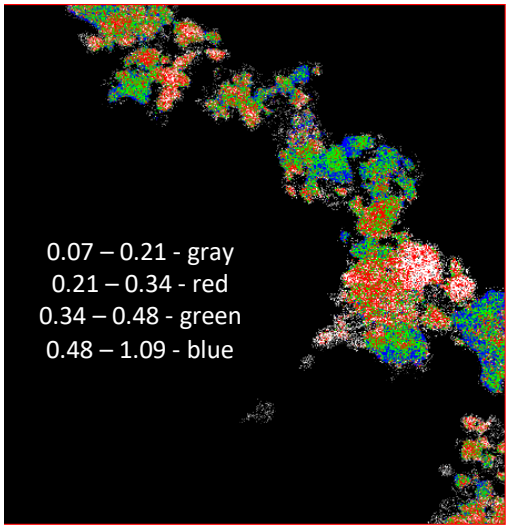

Figure 60. Spectra of four regions of the Fe edge of LiC50 sample (left) and corresponding masks composite image (right)

As it is visible from the spectra above, high Peak A/Peak C ratio corresponds to the most deintercalated part of the sample, which looks quite similar to LiC01 Fe average spectra.

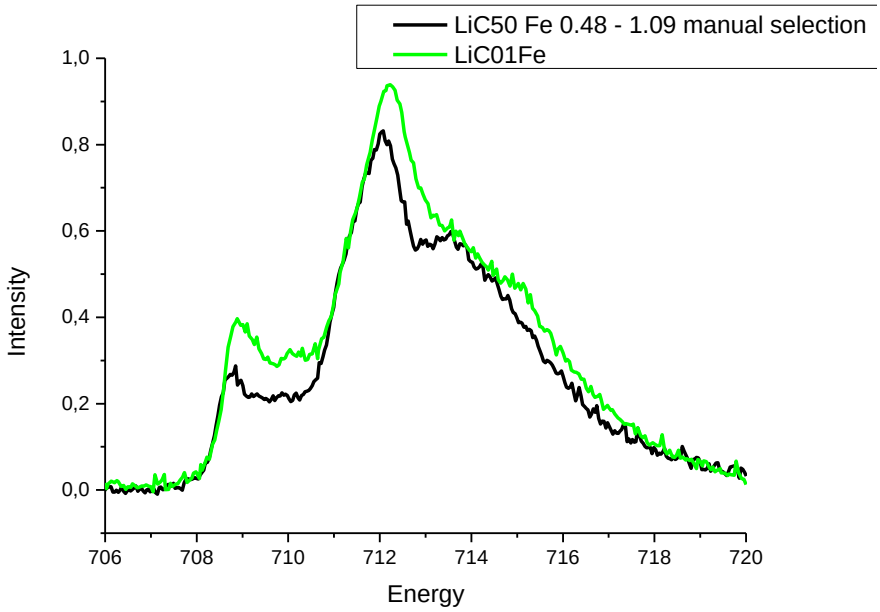

Figure 61. Spectrum of the 0.48 - 1.09 region of the Fe edge of LiC50 sample compared to LiC01 Fe average spectrum

On the other hand, low Peak A/Peak C ratios looks more like discharged sample. For avoidance of the noise and artefacts, at first, 5 points 5pixel by 5 pixel were chosen inside this range and plotted For the further check, 15 points from Mn edge were chosen (see below) and transferred to Fe edge. Indeed, the intercalation is observed in different element edges correspond to the same parts of the sample.

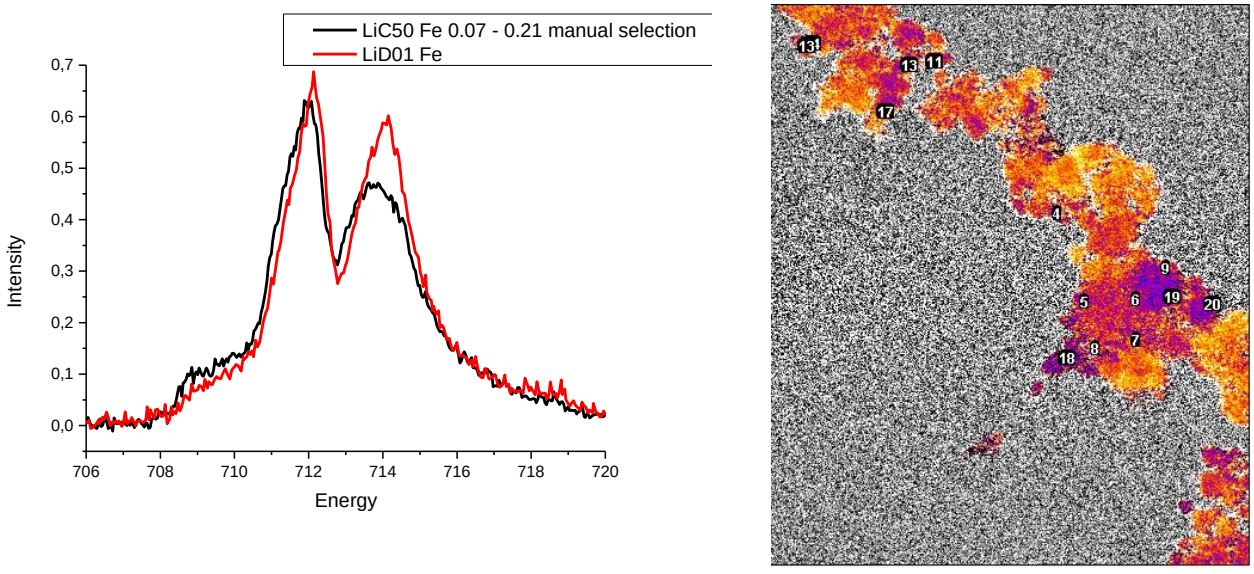

Figure 62. Spectrum of the 0.07 - 0.21 region, 14 points of the Fe edge of LiC50 sample compared to LiD01 Fe average spectrum (left) and same 14 points on (Peak C - Pre-absorption)/(Peak A – Pre-absorption) map

Small intensity in Peak A region in LiC50 sample is still visible, but it is very low, also Peak C intensity has significantly increased. However, there is not a perfect overlap to the discharged sample spectrum, For peak A the sample is almost completely intercalated, but not really for peak

C. This means that the compound is something intercalated-like, but indeed not identical to LiD01, which means that total intercalation even in just some parts of LiC50 sample is not reached.

Same treatment was done on the other edges:

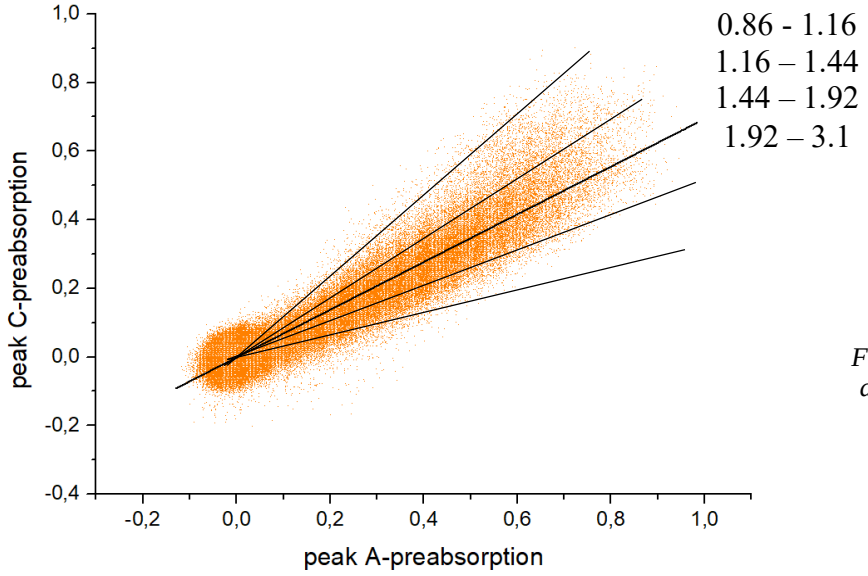

Figure 63. Scatter plot of LiC50 Mn (Peak C - Pre-absorption)/(Peak A – Pre-absorption) divided by four regions

As in the Mn edge peak A is generally observed in intercalated sample, consequently, Peak A/Peak C ratio is the opposite to Fe edge. It is expected to see less deintercalated region on the high threshold range (1.92 – 3.1).

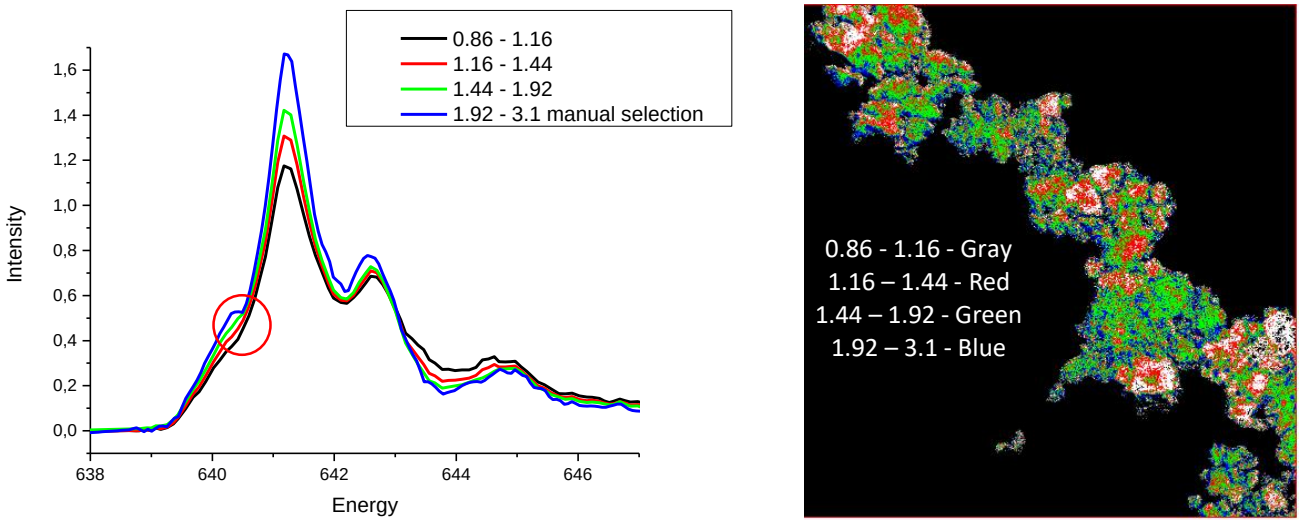

Figure 64. Spectra of four regions of the Mn edge of LiC50 sample (left) and corresponding selections composite image (right)

To check if on Mn edge it has the same pattern as iron edge (intercalation in charged sample), five selected points from LiC50 Fe were carefully transferred to Mn stack. Similarities between two edges were observed As above was mentioned, addition of 15 points were chosen in LiC50 Mn,

which were in the range suggested by scattered plot. As a result, Peak A is visible, but less intense than in discharged samples.

Figure 65. Spectrum of the 1.92 -- 3.1 region, 20 points of the Mn edge of LiC50 sample compared to LiC01 Mn and LiD01 Mn average spectrum (left) and same 20 points on (Peak C - Pre-absorption)/(Peak A – Pre-absorption) map

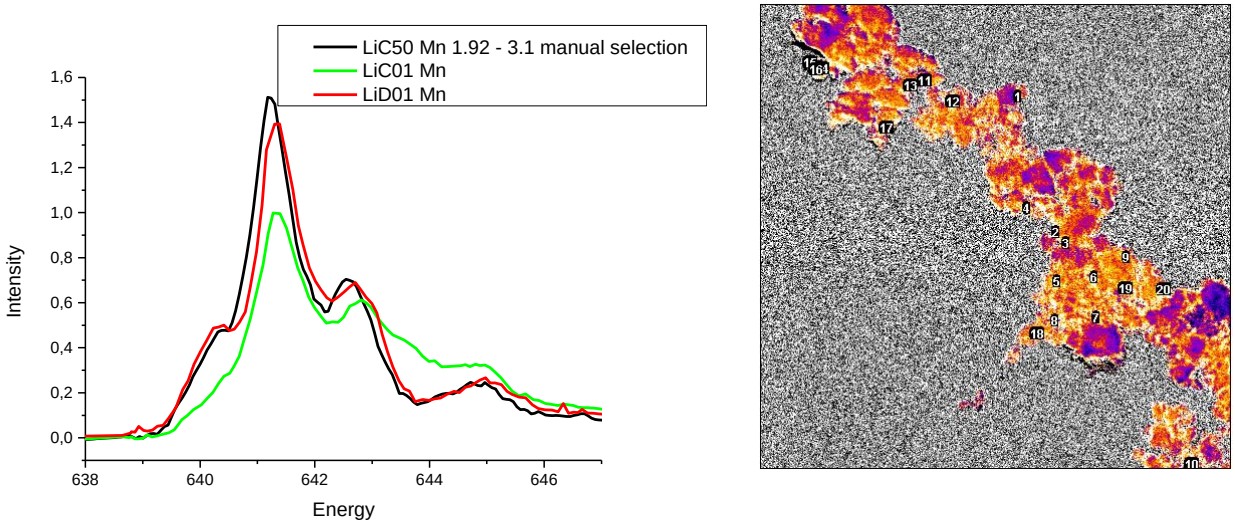

In nitrogen edge, peak A, which is, generally, visible in charged samples, already has very low intensity, so judging intercalation for N edge is harder.

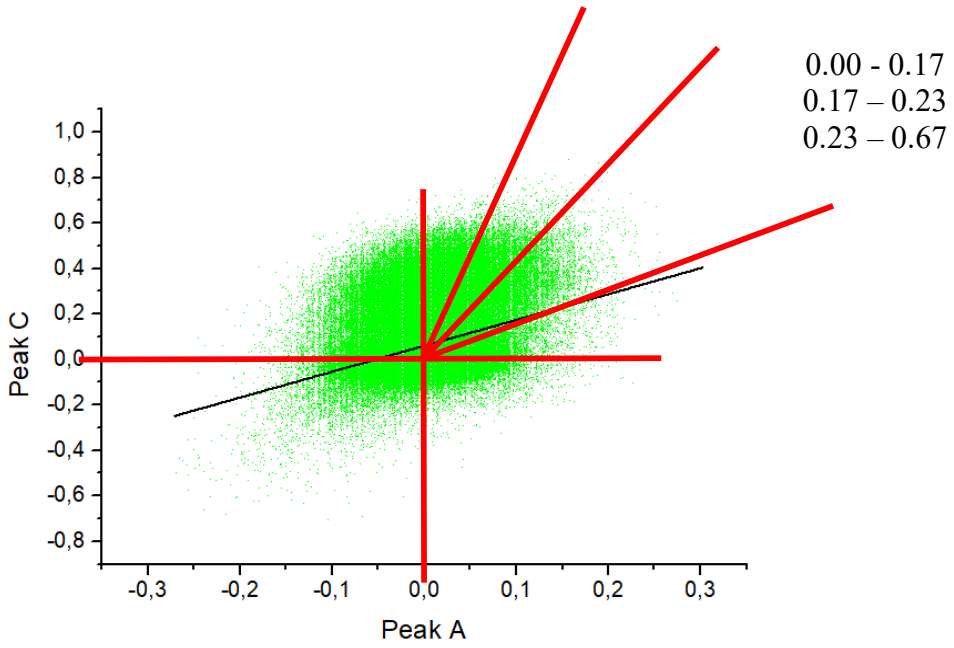

Figure 66. Scatter plot of LiC50 N (Peak C - Pre-absorption)/(Peak A – Pre-absorption) divided by three regions

Corresponding spectra were obtained and masks and composite images were made.

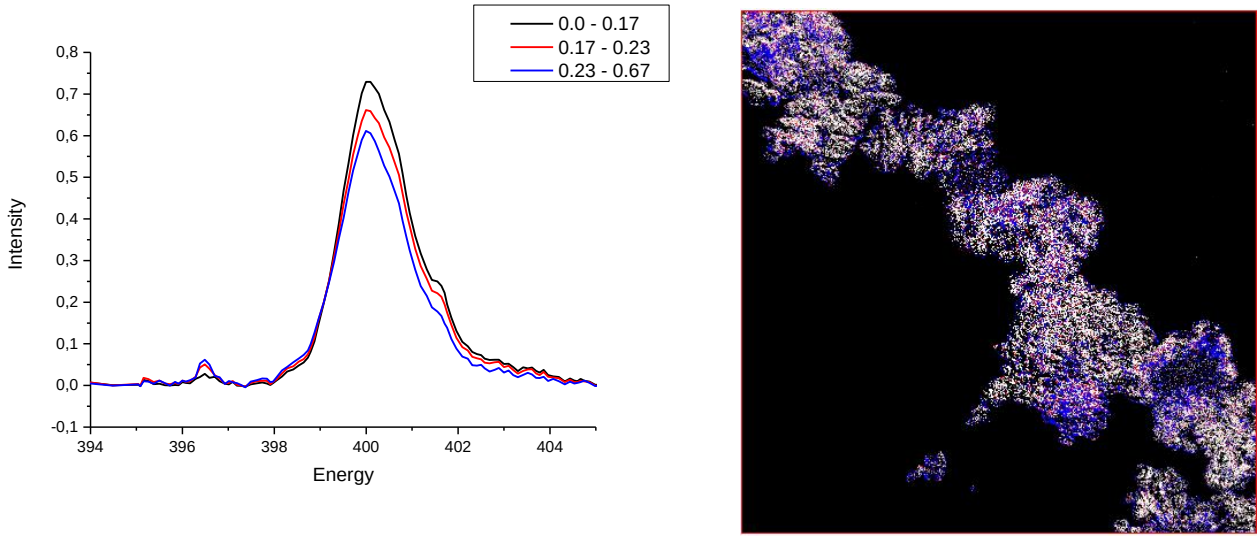

Figure 67. Spectra of three regions of the N edge of LiC50 sample (left) and corresponding masks composite image (right)

All points, which were chosen in iron and manganese edge were transferred to nitrogen edge. The average spectrum of those selection looks similar to LiD01 sample, and shares practically nothing with LiC01 sample.

Figure 68. Spectrum of the 0.00 -- 0.17 region, 19 points of the N edge of LiC50 sample compared to LiC01 N and LiD01 N average spectrum (left) and same 19 points on (Peak C - Pre-absorption)/(Peak A – Pre-absorption) map

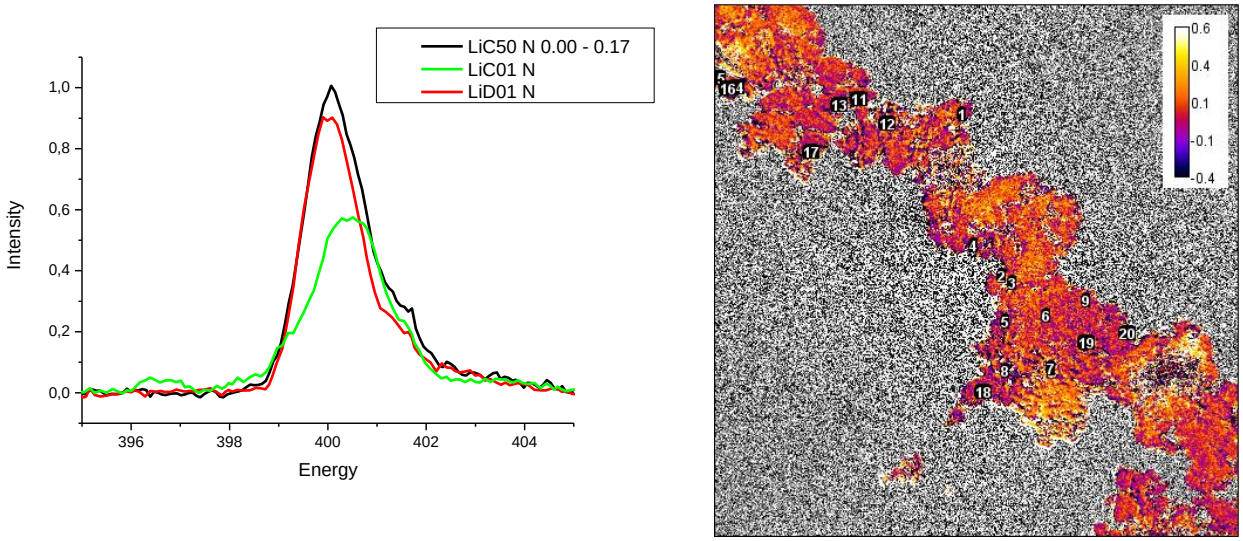

In overall, there is some consistencies between different edges. The spatial distribution of each region mask and their overlap among the other edges is shown in the matrix below:

			Mn				Fe				N		
			I	II	III	IV	I	II	III	IV	I	II	III
			12.47 %	24.59 %	34.00 %	17.16 %	13.99 %	33.47 %	34.13 %	16.56 %	31.30 %	7.44 %	16.00 %
Mn	I	12.47 %											
	II	24.59 %											
	III	34.30 %											
	IV	17.16 %											
Fe	I	13.99 %											
	II	33.47 %											
	III	34.13 %											
	IV	16.56 %											
N	I	31.30 %											
	II	7.44 %											
	III	16.00 %											

To sum up, using transmission soft X-ray microscopy made possible to see the changes inside the cathode material after charge/discharge cycling. After 50 cycles in LiC50 sample, there is evident presence of intercalated species, which were found in all edges. It was possible to transfer their location from one edge to another and retrieve them by this way, which means, that there was a good correlation between the edges.

6. Electrochemical Characterization: Cyclic Voltammetry

Electrochemical characterization of synthesized samples was done by cyclic voltammetry. As an electrolyte $NaNO_3$ was used with tree different concentrations: 0.1M, 1M and 5M aqueous solutions.

As it was mentioned in the experimental part, several scan rates (SR) were tested. The voltage always refers to a standard, SCE. Generally, with decreasing the scan rate, data becomes more resolved as electrolyte has more time to fully insert to the electrode material, and the separation of the oxidation-reduction peaks is more evident. For example, 30% addition of Ni sample in 0.1M $NaNO_3$ electrolyte, oxidation peak were obtained by using low scan rate:1 mV, whereas in case of 5 mV, it is not visible.

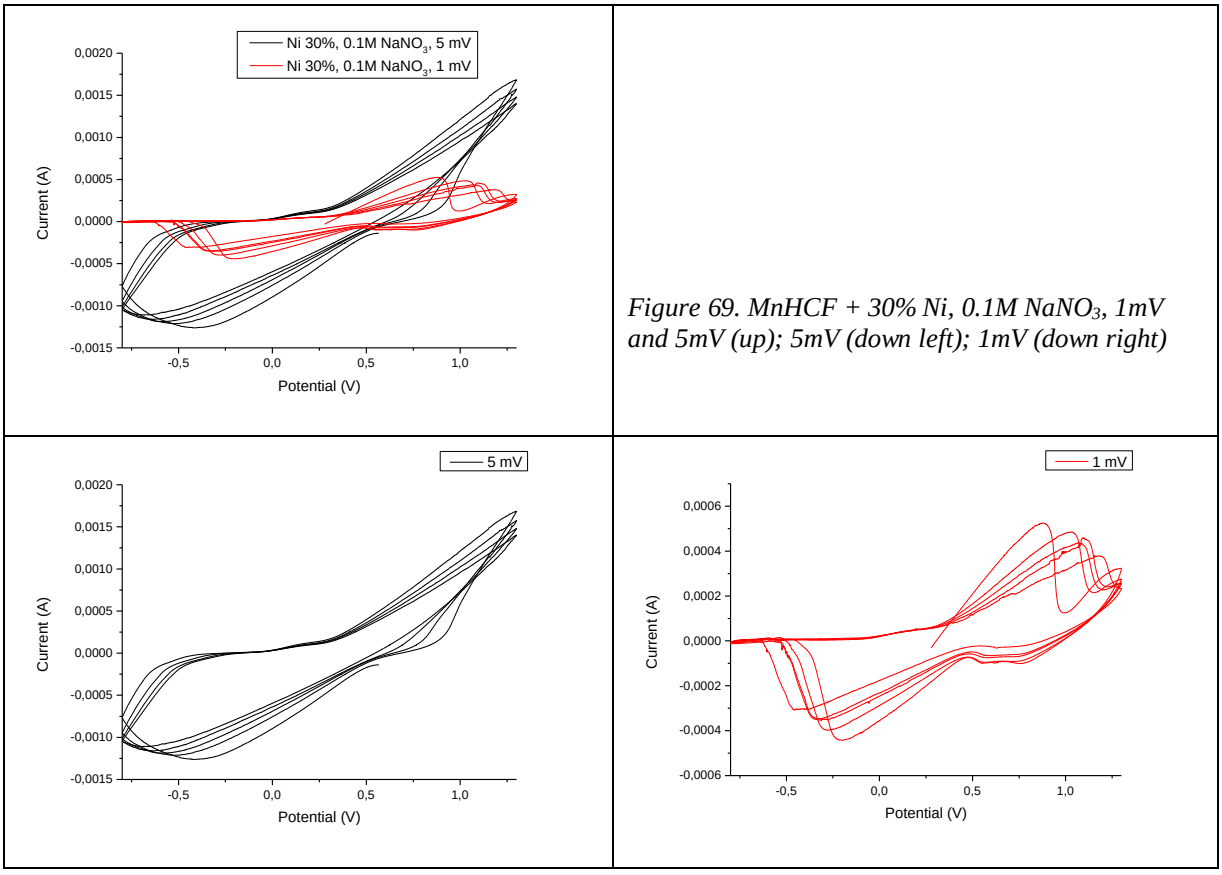

Figure 69. MnHCF + 30% Ni, 0.1M $NaNO_3$, 1mV and 5mV (up); 5mV (down left); 1mV (down right)

Of course, using glass electrodes, also has limitation towards the scan rate. Usually, SR lower than 0.5mV is not used.

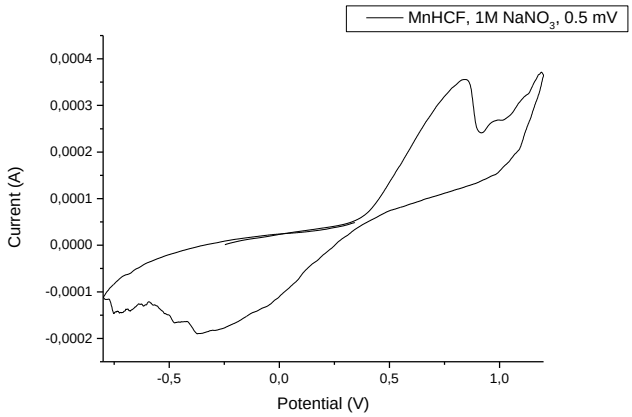

Figure 70. MnHCH, 1M NaNO3, SR=0.5mV

During the cycling sodium ions are migrating from electrolyte into cathode material (discharge), MnHCF, and back (charge).

$$MnHCF^{+}_{solid} + Na^{+} + e^{+} \rightleftarrows NaMnHCF_{solid}$$

As it is known from the literature, Ni is not electrochemically active in Prussian Blue materials [41], however, it has an influence, which was confirmed in CV experiments as well. In overall, addition of nickel to MnHCF caused the increase of peak-to-peak separation.

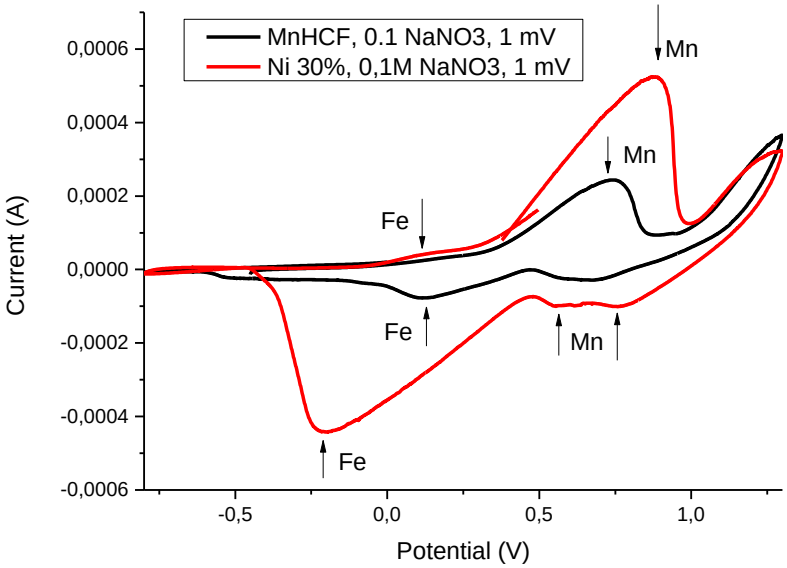

$Mn^{2+/3+}$ oxidation peak moved from 0.75 to 0.88 V versus SCE, whereas the reduction has shifted from 0.13 to -0.21 versus SCE. Totally increment to peak-to-peak separation is up to 0.5V. In Ni containing sample, the region of Mn reduction showed more than one peak, which allows to

conclude, that there might be several different manganese electroactivity interests some nearly-equivalent Mn sites, whose oxidation reduction phenomena occurring at different voltages. Fe oxidation peak has very low intensity in both samples.

Peak-to-peak separation has also increased with changing the concentration of the electrolyte from 0.1M to 1M and 5 M.

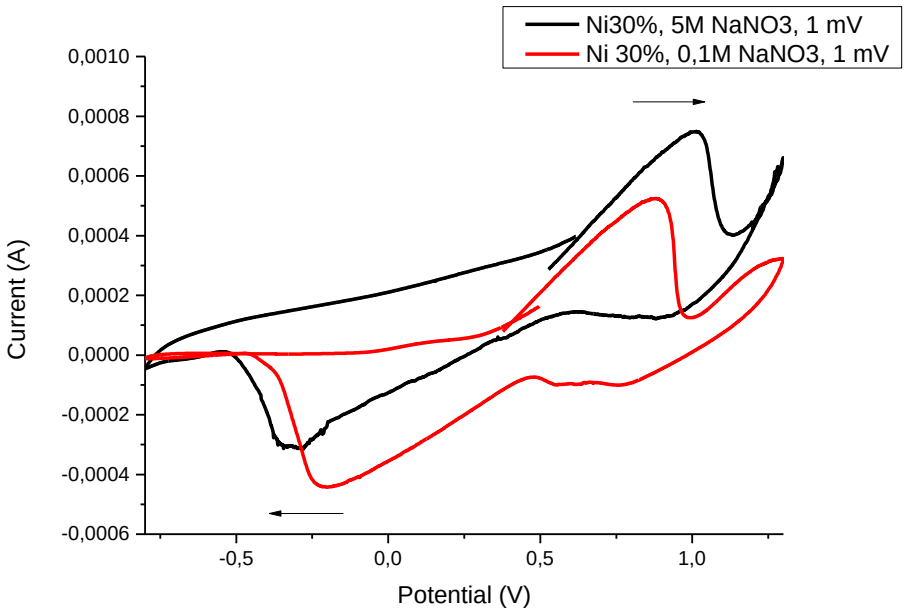

This phenomena is expectable and explainable with Nernst equation:

$$E = E^0 + \frac{RT}{nF}\ln\frac{(Ox)}{(Red)} = E^0 + 2.3026\frac{RT}{nF}\log_{10}\frac{(Ox)}{(Red)}$$

$$E = E^0 + \frac{RT}{nF}\log[Na^+] = E^0 + 0.059\log[Na^+]$$

Theoretically with the increase of the concentration of the electrolyte by 10 times, the peak-to-peak separation is increasing by 59 mV. In practice, it is, generally, a little bit more. Here also, as the concentration increased 50 times (0.1M to 5M), it was expected to be the shift of 295 mV. According to the experimental measurements the oxidation peak of Mn got shifted to higher potential by approximately 0.165V, as for reduction peak of iron, it shifted towards lower potential by 0.1V. Same has also been detected in the other samples, in pure MnHCF from 0.1M to 1M and to 5M, the Fe reduction peak shifted from 0.117V to -0.011V and -0.140 V versus SCE respectively; in MnHCF + 10% Ni same peak shifted from 0.102 to -0.120V versus SCE.

Conclusions

In this work, it was evident that in synthesized metal hexacyanoferrates nickel addition to manganese causes changes in structure and consequently in its properties. MP-AES and TGA measurements show the increase of both vacancies and water content, however, the sample with 10% nickel doping has higher values in these parameters than 30% of Ni.

As IR spectra suggests, second metal addition to Mn should have caused an increase in the effective charge on the iron, weakened metal−C≡N π back-bonding and strengthen σ bonding. Also new bands got visible, which again confirms the changes in the functional groups of the materials.

Further differences became evident from the PXRD analysis, which showed that space group of the material changed after nickel addition. Second metal doping caused the increase of the symmetry from monoclinic P 21/n to cubic F m-3m. Cell volume almost doubled from pure MnHCF to 10% Ni addition MnHCF. From 10% to 30% Ni addition small contraction of the unit cell is observed. Here it can also be said, that refinement of the parameters were quite tedious, especially with light elements such as oxygen.

XAS analysis showed only minor differences in the pre-edge and XANES part of the absorption spectra. EXAFS fitting demonstrated that nickel addition caused almost no local structure disturbance in Fe site, which can be explained by high stability and stiffness of C≡N bond. However, Mn-N bond length gradually decreased with Ni addition. Debye-Waller factor and asymmetry parameter shows distortion at Mn site. It worth to mention, that Ni position to same as Mn, which was chosen from the XRD fitting, was in good correlation with EXAFS fitting as well.

Important conclusions about MnHCF as cathode material (using a material previously synthesized) can be derived from the charge/discharge cycling. Complementary imaging techniques 2D XRF as macro-analysis and TXM as micro-analysis showed intercalation in charged sample after cycling. The inhomogeneities are higher in cycled charged sample, than in cycled discharged one. TXM measurements showed that the intercalation is visible in all probed edges (Fe and Mn L-edge and N K-edge) and they are in a good correlation with one another.

Electrochemical test showed two redox active centers in the synthesized material: Mn and Fe. Despite the fact that Ni is not taking part in actual oxidation-redaction process, it influenced the dynamic of the electrochemical processes of the material. Further tests are needed to investigate and confirm such observation.

References

[1] "THE NOBEL PRIZE IN CHEMISTRY," THE NOBEL PRIZE, [Online]. Available: https://www.nobelprize.org/prizes/chemistry/#:~:text=The%202019%20Nobel%20Prize%20in,the%20greatest%20benefit%20to%20humankind..

[2] Languang Lu, Xuebing Han, Jianqiu Li, Jianfeng Hua, Minggao Ouyang, "A review on the key issues for lithium-ion battery management in electric vehicles," *Journal of Power Sources,* vol. 226, pp. 272-288, 15 March 2013.

[3] M. Armand, J. M. Tarascon, *Nature,* no. 451, p. 652, 2008.

[4] Yonggang Wang, Jin Yi, Yongyao Xia, "Recent Progress in Aqueous Lithium-Ion Batteries," *Advanced Energy Materials,* no. 2, pp. 830-840, 18 June 2012.

[5] W. Harris, "Ph.D. Thesis UCRL-8381," University of California, Berkeley.

[6] KM Abraham and S.B. Brummer, "Lithium Batteries," *Academic Press,* 1983.

[7] M. Whittingham, *Prog. Solid State Chem.,* no. 12, pp. 41-111.

[8] B. C. H. Steele, "Fast ion transport in solids: solid-state batteries and devices," *North-Holland/American Elsevier, Inc.,* p. 103, 1973.

[9] K. Mizushima, P.C. Jones, P.J. Wiseman, and J.B. Goodenough, *Mat. Res. Bull.,* no. 15, p. 783, 1980.

[10] M.M. Thackeray, W.I.F. David, P.G. Bruce, and J. B. Goodenough, *Mat. Res. Bull.,* no. 18, p. 461, 1983.

[11] M. Lazzari and B. Scrosati, *J. Electrochem. Soc.,* no. 127, p. 773, 1980.

[12] D.W. Murphy, F.J. DiSalvo, J.N. Carides and J.V. Waszczak, *Mat. Res. Bull.,* no. 13, p. 1395, 1978.

[13] Walter van Schalkwijk, Bruno Scrosati, "Introduction," in *Advances in Lithium Ion Batteries*, Boston, MA, Springer, 2002, pp. 1-2.

[14] Dr. Prasant Kumar Nayak, Liangtao Yang, Wolfgang Brehm, Prof. Philipp Adelhelm, "From Lithium-Ion to Sodium-Ion Batteries: Advantages, Challenges, and Surprises," *Angewandte Chemie International Edition,* vol. 57, no. 1, pp. 102-120, 2018.

[15] W. Li, J. R. Dahn, D. Wainwright, *Science,* no. 264, p. 1115, 1994.

[16] Marc Walter, Maksym V. Kovalenko and Kostiantyn V. Kravchyk, "Challenges and benefits of post-lithium-ion batteries," *New Journal of Chemistry,* no. 44, pp. 1677-1683, 2020.

[17] Michael D. Slater Donghan Kim Eungje Lee Christopher S. Johnson, "Sodium-Ion Batteries," *Advanced Functional Materials,* vol. 23, no. 8, pp. 947-958, 2013.

[18] Y.-U. Park, D.-H. Seo, H.-S. Kwon, B. Kim, J. Kim, H. Kim, I. Kim, H.-I. Yoo and K. Kang, *Journal of American Chemical Society,* vol. 135, pp. 13870-13878, 2013.

[19] M. Nose, H. Nakayama, K. Nobuhara, H. Yamaguchi, S. Nakanishi and H. Iba, *Journal of Power Sources,* vol. 234, pp. 175-179, 2013.

[20] B. Jache and P. Adelhelm, , 2014, 53, 10169–10173, *Angewandte Chemie International Edition,* vol. 53, pp. 10169-10173, 2014.

[21] H. Kang, Y. Liu, K. Cao, Y. Zhao, L. Jiao, Y. Wang and H. Yuan, *Journal of Material Chemistry A,* no. 3, p. 17899–17913, 2015.

[22] M. Walter, R. Erni and M. V. Kovalenko, *Scientific Reports,* no. 5, p. 8418, 2015.

[23] C.-M. Park, J.-H. Kim, H. Kim and H.-J. Sohn, *Chemical Society Reviews,* no. 39, p. 3115–3141, 2010.

[24] DONGLIANG CHAO, WANHAI ZHOU, FANGXI XIE, CHAO YE, HUAN LI, MIETEK JARONIEC, SHI-ZHANG QIAO, "Roadmap for advanced aqueous batteries: From design of materials to applications," *SCIENCE ADVANCES,* 2020.

[25] Jiangfeng Qian, Chen Wu, Yuliang Cao, Zifeng Ma, Yunhui Huang, Xinping Ai, Hanxi Yang, "Prussian Blue Cathode Matherials for Sodium-Ion Batteries and Other Ion Batteries," *Advanced Energy Materials,* no. 8, p. 1702619, 2018.

[26] Baoqi Wang, Yu Han, Xiao Wang, Naoufal Bahlawane, Hongge Pan, Mi Yan and Yinzhu Jiang, "Prussian Blue Analogs For Rechargeable Batteries," *iScience,* no. 3, pp. 110-133, 25 May 2018.

[27] A. Paolella, C Faure, V. Timoshevski, S. Marras, G. Bertoni, A. Guerfi, A. Vijh, M. Armand, K. Zaghib, *Journal of Materials Chemistry A,* no. 5, p. 18919, 2017.

[28] T. Shibata, Y. Morimoto, *Chemical Communications,* no. 50, p. 12941, 2014.

[29] M. Takachi, Y. Fukuzumi, Y. Morimoto, *Dalton Transactions,* no. 45, p. 458, 2016.

[30] K. Itaya, I. Uchida, V. D. Neff, *Accounts of Chemical Research,* no. 162, p. 162, 1986.

[31] Y. H. Lu, L. Wang, J. G. Cheng, J. B. Goodenough, *Chemical Communications,* no. 48, p. 6544, 2012.

[32] M. Takachi, T. Matsuda, Y. Moritomo, *Japanese Journal of Applied Physics,* no. 52, p. 090202, 2013.

[33] Y. You, X. L. Wu, Y. X. Yin, Y. G. Gou, *Journal of Materials Chemistry A,* no. 1, p. 14061, 2013.

[34] Wu et al., *American Chemical Society,* 2016.

[35] Wang et al., 2013a.

[36] Song et al. , *American Chemical Society,* 2015.

[37] Matsuda et al., 2013.

[38] Fu et al., 2017.

[39] Yang et al., 2014.

[40] Morimoto et al., 2016.

[41] Dezhi Yang, Jing Xu, Xiao-Zhen Liao, Yu-Shi He, Haimei Liu and Zi-Feng Ma, "Structure optimization of Prussian blue analogue cathode materials for advanced sodium ion batteries," *ChemComm*, no. 50, p. 13377, 2014.

[42] "Introduction & History," Elettra Synchrotron Trieste, 01 December 2011. [Online]. Available: https://www.elettra.trieste.it/lightsources/elettra/odac/elettra-intro.html?showall=.

[43] "Introduction & History: Elettra configuration since 2007," Elettra Synchrotron Trieste, 01 December 2011. [Online]. Available: https://www.elettra.trieste.it/lightsources/elettra/odac/elettra-intro/page-3.html?showall=.

[44] "Introduction & History: Elettra operation configuration since 2010," Elettra Synchrotron Trieste, 01 December 2011. [Online]. Available: https://www.elettra.trieste.it/lightsources/elettra/odac/elettra-intro/page-4.html?showall=.

[45] dc.edu.au, "HSC Physics – Quanta to Quarks," Dux College Sydney, [Online]. Available: https://dc.edu.au/wp-content/uploads/synchrotrons.png.

[46] M. Giorgetti, "X-ray analysis: XAFS, EXAFS equation, approximations and single terms," University of Bologna, Bologna, 2019.

[47] P. Fornasini, "Introduction," in *Welcome to XAFS: a friendly but not so short tutorial*, Trento, Italy, Department of Physics, University of Trento, January 2014, pp. 2-9.

[48] M. GIorgetti, "X-ray analysis: XANES spectroscopy," University of Bologna, Bologna, 2019.

[49] Sayers, D. E., Stern E. A., Lytle F.W., *Physical Review Letters*, vol. 27, pp. 1204-1207, 1971.

[50] W. Bragg, "The structure of some crystals as indicated by their diffraction of X-rays," *Proc. R. Soc. Lond. A Math. Phys. Eng. Sci.*, no. 89, pp. 248-277, 1913.

[51] Benedict Tsz Woon Lo, Lin Ye, Shik Chi Edman Tsang, "The Contribution of Synchrotron X-Ray Powder Diffraction to Modern Zeolite Applications: A Mini-review and Prospects," *Chem*, vol. 4, no. 8, pp. 1778-1808, 9 August 2018.

[52] Cameron F. Holder, Raymond E. Schaak, "Tutorial on Powder X-ray Diffraction for Characterizing Nanoscale Materials," *Americal Chemical Society Nano*, no. 13, pp. 7359-7365, 23 July 2019.

[53] J.K. Cockcroft, A.N. Fitch, "Experimental setups," in *Powder Diffraction. Theory and Practice*, S. B. R.E. Dinnibier, Ed., Royal Society of Cambridge, 2008, pp. 20-57.

[54] M.G. O'Brien, A.M. Beale, S.D.M. Jacques, M. Di Michiel, B.M. Weckhuysen, "Closing the operando gap: the application of high energy photons for studying catalytic solids at work," *Appl. Catal. A Gen.*, no. 391, pp. 468-476, 2011.

[55] H. Kohlmann, "Structural Analysis in Inorganic Chemistry," University of Leipzig, Leipzig, 2019.

[56] S. Daviero-Minuad, "Chapter 5: Powder X-ray Diffraction," UCCS - Unite de Catalyse et Chimie du Solide, Villeneuve d'Ascq, 2018.

[57] Eva Margui, Rene Van Grieken, "Introduction," in *X-Ray Fluorescence Spectrometry and Related Techniques: An Introduction*, New York, Momentum Press, 2013.

[58] K. G. Janssens, "X-Ray Fluorescence Analysis," in *Handbook of Spectroscopy*, D. S. G. Moore, Ed., 2014.

[59] Dino Tonti, Mara Olivares-Marín, Andrea Sorrentino and Eva Pereiro, "Studies of Lithium-Oxygen Battery Electrodes by Energy- Dependent Full-Field Transmission Soft X-Ray Microscopy," in *X-ray Characterization of Nanostructured Energy Materials by Synchrotron Radiation*, L. P. Mehdi Khodaei, Ed., IntechOpen, 22 March, 2017.

[60] A. D., Soft X-Rays and Extreme Ultraviolet Radiation: Principles and Applications, Cambridge: Cambridge University Press, 1999.

[61] M. S., "Interaction between radiation and matter: an introduction," in *Synchrotron Radiation: Fundamentals, Methodologies and Applications*, V. G. Mobilio S, Ed., Bologna, Società Italiana di Fisica, 2001, p. Vol. 82.

[62] Andrea Sorrentino, Josep Nicolás, Ricardo Valcárcel, Francisco Javier Chichón, Marc Rosanes, Jose Avila, Andrei Tkachuk, Jeff Irwin, Salvador Ferrer, Eva Pereiro, "MISTRAL: a transmission soft X-ray microscopy beamline for cryo nano-tomography of biological samples and magnetic domains imaging," *Journal of Synchrotron Radiation*, vol. 22, no. 4, pp. 1112-7, 2015.

[63] Balaram Vysettia, Dharmendra Vummitib,e, Parijat Royc, Craig Taylord, C.T. Kamalaa, M. Satyanarayanana,Prasenjit Karb, K.S.V. Subramanyama, Arun Kumar Rajub, and Krishnaiah Abburie, "Analysis of Geochemical Samples by Microwave Plasma-AES," *Atomic Spectroscopy*, vol. 35, no. 2, pp. 65-66, March/April 2014.

[64] Rodolfo Lorençatt, Debora Nascimento Monção, Rafael Araújo Silva, "High Throughput, Multi-Element Analysis of Effluents by MP-AES: Low-cost method using the Agilent 4210 MP-AES with AVS 4 switching valve in accordance with Brazilian regulations," *Agilent Trusted Answers: Application Note, Environmental*, Vols. 5994-1746EN, no. DE. 8216898148, 17 May 2020.

[65] Zhanen Zhang and Kazuaki Wagatsuma, "Comparison of the analytical performance of high-powered, microwave-induced air plasma and nitrogen plasma atomic emission spectrometry," *The Royal Society of Chemistry, Journal Of Analitical Atomic Spectrometry*, no. 17, p. 699–703, 18 June 2002.

[66] "Thermogravimetric Analysis (TGA)," in *A beginners guide*, Waltham, MA 02451 USA, PerkinElmer.Inc, 2010-2015, pp. 3-4, 6.

[67] D.A. Granados, Hector I. Velasquez, Farid Chejne Janna, "Energetic and exergetic evaluation of residual biomass in a torrefaction process," *Energy*, vol. 10, no. 74, p. 1016, 2014.

[68] "3. Infrared spectroscopy," in *Modern Chemical Techniques*, THE ROYAL SOCIETY OF CHEMISTRY, p. 62.

[69] C. Schaefer and F. Matossi, Das Ultrarot Spektrum, Berlin: Springer, 1930.

[70] V. Scheidt, *Naturf.*, vol. 5, no. 76, p. 270, 1952.

[71] M. Stimson, *Journal of Americal Chemical Society*, no. 74, p. 1805, 1952.

[72] P. R. 1. 3. 1. M.J. Stimson, *Phys. Radium* , no. 15, p. 390, 1954.

[73] G. Pimentel, *Spedrochim. Acta*, no. 12, p. 94, 1957.

[74] J. Lecompte, *Anal. Chim. Acta,* no. 2, p. 727, 1948.

[75] J. Lecompte, *Cahiers Phys.,* no. 17, p. 1, 1943.

[76] F. Miller and C.H. Wilkins, *Analytical Chemistry,* no. 24, p. 1253, 1952.

[77] J. R. Ferraro, "Introduction to Inorganic Infrared Spectroscopy," in *Progress in Infrared Spectroscopy*, H. A. Szymanski, Ed., New York, Springer Science+Business Media, 1962, pp. 35-36.

[78] Panowicz, Robert & Miedzińska, Danuta & Palka, Norbert & Niezgoda, Tadeusz, "The initial results of THz spectroscopy non-destructive investigations of epoxy-glass composite structure," 2011.

[79] "Basics of voltammetry and polarography," in *Application Note P-2*, Princeton Applied Research, Applied Instrument Group, pp. 1-12.

[80] J. Wang, "Chapter 2," in *Analytical Electrochemistry,*, John Wiley & Sons, 2000.

[81] R.S. Nicholson and I. Shain, "Theory of stationary electrode polarography, single scan and cyclic methods applied to reversible, irreversible and kinetic systems," *Analytical Chemistry,* no. 36, pp. 706-723, 1964.

[82] Joshi P.S., Sutrave D.S., "A Brief Study of Cyclic Voltammetry and Electrochemical Analysis," *International Journal of ChemTech Research,* vol. 11, no. 09, pp. 77-89, 2018.

[83] Noémie Elgrishi, Kelley J. Rountree, Brian D. McCarthy, Eric S. Rountree, Thomas T. Eisenhart and Jillian L. Dempsey, "A Practical Beginner's Guide to Cyclic Voltammetry," *Journal of Chemical Education,* vol. 2, no. 95, pp. 197-206, 2018.

[84] Bard, A. J.; Faulkner, L. R., Electrochemical Methods: Fundamental and Applications, New Jersey: John Wiley & Sons: Hoboken, 2nd ed., 2001.

[85] J.-M. Savéant, Elements of Molecular and Biomolecular Electrochemistry, 2006: John Wiley & Sons: Hoboken, New Jersey.

[86] "XAFS: Beamline description," Elettra Synchrotron Trieste, 28 November 2019. [Online]. Available: https://www.elettra.trieste.it/lightsources/elettra/elettra-beamlines/xafs/specifications.html?showall=.

[87] "XAFS: Optical scheme," Elettra Synchrotron Trieste, 28 November 2019. [Online]. Available: https://www.elettra.trieste.it/lightsources/elettra/elettra-beamlines/xafs/specifications/page-2.html?showall=.

[88] "XAFS: Specifications," Elettra Synchrotron Trieste, 13 January 2012. [Online]. Available: https://www.elettra.trieste.it/lightsources/elettra/elettra-beamlines/xafs/specs.html.

[89] "XAFS: Endstation," Elettra Synchrotron Trieste, 28 November 2019. [Online]. Available: https://www.elettra.trieste.it/lightsources/elettra/elettra-beamlines/xafs/specifications/page-3.html?showall=.

[90] "MCX: Beamline Description," Elettra Synchrotron Trieste, 31 October 2012. [Online]. Available: https://www.elettra.trieste.it/lightsources/elettra/elettra-beamlines/mcx/endstations.html.

[91] "MCX: Beamline description - diffractometer," Elettra Synchrotron Trieste, 31 October 2012. [Online]. Available: https://www.elettra.trieste.it/lightsources/elettra/elettra-beamlines/mcx/endstations/page-2.html?showall=.

[92] "MCX: Specifications," Elettra Synchrotron Trieste, 19 February 2019. [Online]. Available: https://www.elettra.trieste.it/lightsources/elettra/elettra-beamlines/mcx/specifications.html?showall=.

[93] "MCX: Specifications - Monochromators," Elletra Synchrotron Trieste, 19 February 2019. [Online]. Available: https://www.elettra.trieste.it/lightsources/elettra/elettra-beamlines/mcx/specifications/page-3.html?showall=.

[94] "X-ray Fluorescence: Specifications," Elettra Synchrotron Trieste, 31 July 2019. [Online]. Available: https://www.elettra.trieste.it/lightsources/elettra/elettra-beamlines/microfluorescence/2019-07-30-16-19-44.html.

[95] "X-ray Fluorescence: beamline description," Elettra Synchrotron Trieste, 31 July 2019. [Online]. Available: https://www.elettra.trieste.it/lightsources/elettra/elettra-beamlines/microfluorescence/beamline-description.html.

[96] " X-ray fluorescence: X-ray fluorescence detectors," Elettra Synchrotron Trieste, 31 July 2019. [Online]. Available: https://www.elettra.trieste.it/lightsources/elettra/elettra-beamlines/microfluorescence/beamline-description/page-3.html?showall=.

[97] "MISTRAL - Soft X-ray microscope beamline," ALBA Synchrotron Facility. [Online].

[98] "4210 MP-AES," Agilent, [Online]. Available: https://www.agilent.com/en/products/mp-aes/mp-aes-systems/4210-mp-aes.

[99] Jie Song, Long Wang, Yuhao Lu, Jue Liu, Bingkun Guo, Penghao Xiao, Jong-Jan Lee, Xiao-Qing Yang, Graeme Henkelman and John B. Goodenoug, "Removal of Interstitial H2O in Hexacyanometallates for a Superior Cathode of a Sodium-Ion Battery," *Journal of Americal Cheical Society,* vol. 137, p. 2659, 13 February 2015.

[100] L. H. Jones, "Nature of Bonding in Metal Cyanide Complexes asRelated to Intensity and Frequency of Infrared Absorption Spectra," *Inorganic Chemistry,* no. 2, pp. 777-780, 1963.

[101] M. Ross, A. Andersen, Z. W. Fox, Y. Zhang, K. Hong, J. Lee, A. Cordones, A. M. March, G. Doumy, S. H. Southworth, M. A. Marcus, R. W. Schoenlein, S. Mukamel, N. Govind, R. W. Schoenlein, S. Mukamel, N. Govind and M. Khalil, "Comprehensive Experimental and Computational Spectroscopic Study of Hexacyanoferrate Complexes in Water: From Infrared to X-ray Wavelengths," *The Journal of Physical Chemistry B,* no. 122, pp. 5078-5079, 2018.

[102] Wilde, R. E.; Ghosh, S. N.; Marshall, B., *Journal of Inorganic Chemistry,* no. 9, p. 2512, 1970.

[103] Pawel J. Kulesza, Marcin A. Malik, Andrzej Denca and Jerzy Strojek, "In Situ FT-IR/ATR Spectroelectrochemistry of Prussian Blue in the Solid State," *Analytical Chemistry,* no. 68, p. 2444, 1998.

[104] H.-A. Chu, M.T. Gardner, J.P. O'Brien, G.T. Babcock, *Biochemistry,* no. 38, pp. 4533-4541, 1999.

[105] Hsiu-An Chu, Warwick Hillier, Neil A Law, Gerald T Babcock, "Vibrational spectroscopy of the oxygen-evolving complex and of manganese model compounds," *Biochimica et Biophysica Acta (BBA) Bioenergetics,* no. 1-2, pp. 69-82, 5 January 2001.

[106] L.J. Boucher, Mirjana Kotowski, Karl Koeber, Dieter Tille, "Mn Manganese: Coordination Compounds 7," in *Gmelin handbook of Inorganic Chemistry*, Springer-Verlag Berlin Heidelberg GmbH, 1990, p. 8.

[107] Hana Bashir Shawish, Wan Ying Wong, Yi Li Wong, Sheng Wei Loh, Chung Yeng Looi, Pouya Hassandarvish, Alicia Yi Ling Phan, Won Fen Wong, Hao Wang,Ian C. Paterson,Chee Kwee Ea,Mohd Rais Mustafa,Mohd Jamil Maah, "Nickel(II) Complex of Polyhydroxybenzaldehyde N4-Thiosemicarbazone Exhibits Anti-Inflammatory Activity byInhibiting NF-κB Transactivation," *PLoS ONE,* vol. 6, no. 9, p. e100933, 30 June 2014.

[108] P. J. Kulesza, M. A. Malik, A. Denca and Strojek, *Journal of Analytical Chemistry*, no. 68, pp. 2442-2446, 1996.

[109] J. H. Her, P. W. Stephens, C. M. Kareis, J. G. Moore, K. S. Min, J. W. Park, G. Bali, B. S. Kennon and Miller, *J. S. Inorg. Chem.* , no. 49, pp. 1524-1534, 2010.

[110] A. A. J. A. G. P. S. G. M. Mullaliu, "Highlighting the Reversible Manganese Electroactivity in Na-Rich Manganese Hexacyanoferrate Material for Li- and Na-Ion Storage.," *Small Methods,* p. 1900529, 2019.

[111] Dariusz Wardecki, Dickson O. Ojwang, Jekabs Grins, and Gunnar Svensson, "Neutron Diffraction and EXAFS Studies of K2x/3Cu[Fe(CN)6]2/3·nH2O," *Crystal Growth and Design,* no. 17, pp. 1285-1292, 2017.

[112] A. Mullaliu, G. Aquilanti, P. Conti, J. R. Plaisier, M. Fehse,L. Stievano, M. Giorgetti, *Journal of Physical Chemistry C,* no. 122, p. 15868, 2018.

[113] OpenStax, "19.3 SPECTROSCOPIC AND MAGNETIC PROPERTIES OF COORDINATION COMPOUNDS," in *Chemistry: Chapter 19 Transition Metals and Coordination Chemistry*, Rice University, 2016.

[114] K. Hayakawa, K. Hatada, P. D'Angelo, S. Della Longa, C. R. Natoli,M. Benfatto, *Journal of American Chemical Society,* no. 126, p. 15618, 2004.

[115] A. Bianconi, M. Dell'Ariccia, P. J. Durham, J. B. Pendry, *Physical Review B,* no. 26, p. 6502, 1982.

[116] N. Kosugi, T. Yokoyama, H. Kuroda, *Search Results,* no. 104, p. 449, 1986.

[117] F. Farges, *Physical Review B,* no. 71, p. 155109, 2005.

[118] A. Filipponi, A. Di Cicco, C. R. Natoli, *Phys. Rev. B,* no. 52, pp. 15122 - 15135, 1995.

[119] A. Filipponi, A. Di Cicco, *Phys. Rev. B* , no. 52, p. 15135, 1995.

[120] M. Giorgetti, M. Berrettoni, A. Filipponi, P. J. Kulesza, R. Marassi, *Chem. Phys. Lett.,* no. 108, p. 275, 1997.

[121] *J. Am. Chem. Soc.,* no. 118, pp. 6422-6427, 1996.

[122] Firouzi, A., Qiao, R., Motallebi, S. et al. , "Monovalent manganese based anodes and co-solvent electrolyte for stable low-cost high-rate sodium-ion batteries," *Nature Communication,* no. 9, p. 861, 2018.

[123] Rosalie K. Hocking, Erik C. Wasinger, Frank M. F. de Groot, Keith O. Hodgson, Britt Hedman, and Edward I. Solomon, "Fe L-Edge XAS Studies of K4[Fe(CN)6] and K3[Fe(CN)6]: A Direct Probe of Back-Bonding," *Journal of the American Chemical Society,* vol. 32, no. 128, pp. 10442-10451, 2006.

[124] "Wyckoff Positions of Group P21/c (No. 14) [unique axis b]," Bilbao Crystallographic Server, [Online]. Available: https://www.cryst.ehu.es/cgi-bin/cryst/programs/nph-wp-list.

[125] "Wyckoff Positions of Group Fm-3m (No. 225)," Bilbao Crystallographic Server, [Online]. Available: https://www.cryst.ehu.es/cgi-bin/cryst/programs/nph-wp-list.

[126] J. Y. Luo, W. J. Cui, P. He, Y. Y. Xia, Nat. Chem. 2010, 2, 760., *Nature Chemistry,* no. 2, p. 760, 2010.

[127] S. e. al., *American Chemical Society*, 2015.

[128] Olavi Keski-Rahkonen and Manfred O Krause, Total and partial atomic-level widths. Atomic Data and Nuclear Data Tables, 2 ed., vol. 14, 1974, p. 139–146.

[129] "History Of Batteries: A Timeline," upsbatterycenter.com, 3 June 2014. [Online]. Available: http://www.upsbatterycenter.com/blog/history-batteries-timeline/.

Appendix 1: Powder X-ray diffraction

Si XRD data from NIST:

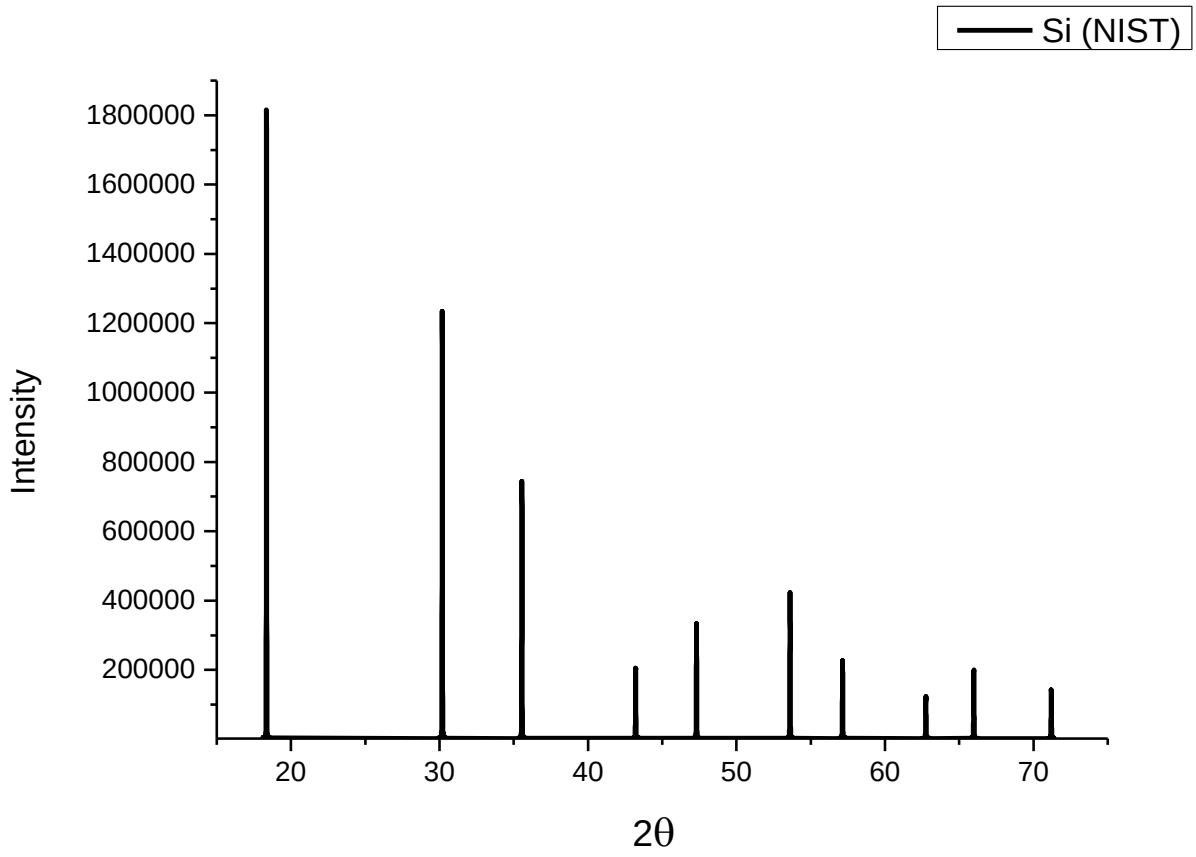

Wyckoff positions of P21/n [124]:

Wyckoff Positions of Group $P2_1/c$ (No. 14) [unique axis b]

Multiplicity	Wyckoff letter	Site symmetry	Coordinates
4	e	1	(x,y,z) (-x,y+1/2,-z+1/2) (-x,-y,-z) (x,-y+1/2,z+1/2)
2	d	-1	(1/2,0,1/2) (1/2,1/2,0)
2	c	-1	(0,0,1/2) (0,1/2,0)
2	b	-1	(1/2,0,0) (1/2,1/2,1/2)
2	a	-1	(0,0,0) (0,1/2,1/2)

MnHCF structure obtained from FPStudio (FullProf Suite):

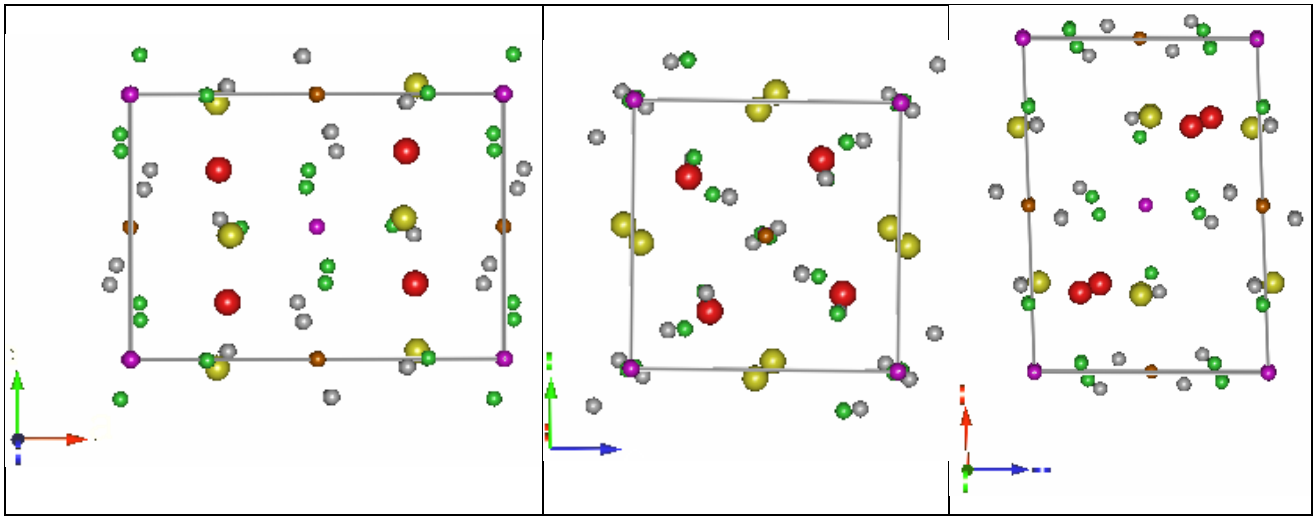

Wyckoff positions of Fm-3m [125]:

Wyckoff Positions of Group *Fm*-3*m* (No. 225)

Multiplicity	Wyckoff letter	Site symmetry	Coordinates
			(0,0,0) + (0,1/2,1/2) + (1/2,0,1/2) + (1/2,1/2,0) +
192	l	1	(x,y,z) (-x,-y,z) (-x,y,-z) (x,-y,-z) (z,x,y) (z,-x,-y) (-z,-x,y) (-z,x,-y) (y,z,x) (-y,z,-x) (y,-z,-x) (-y,-z,x) (y,x,-z) (-y,-x,-z) (y,-x,z) (-y,x,z) (x,z,-y) (-x,z,y) (-x,-z,-y) (x,-z,y) (z,y,-x) (z,-y,x) (-z,y,x) (-z,-y,-x) (-x,-y,-z) (x,y,-z) (x,-y,z) (-x,y,z) (-z,-x,-y) (-z,x,y) (z,x,-y) (z,-x,y) (-y,-z,-x) (y,-z,x) (-y,z,x) (y,z,-x) (-y,-x,z) (y,x,z) (-y,x,-z) (y,-x,-z) (-x,-z,y) (x,-z,-y) (x,z,y) (-x,z,-y) (-z,-y,x) (-z,y,-x) (z,-y,-x) (z,y,x)
96	k	..m	(x,x,z) (-x,-x,z) (-x,x,-z) (x,-x,-z) (z,x,x) (z,-x,-x) (-z,-x,x) (-z,x,-x) (x,z,x) (-x,z,-x) (x,-z,-x) (-x,-z,x) (x,x,-z) (-x,-x,-z) (x,-x,z) (-x,x,z) (x,z,-x) (-x,z,x) (-x,-z,-x) (x,-z,x) (z,x,-x) (z,-x,x) (-z,x,x) (-z,-x,-x)
96	j	m..	(0,y,z) (0,-y,z) (0,y,-z) (0,-y,-z) (z,0,y) (z,0,-y) (-z,0,y) (-z,0,-y) (y,z,0) (-y,z,0) (y,-z,0) (-y,-z,0) (y,0,-z) (-y,0,-z) (y,0,z) (-y,0,z) (0,z,-y) (0,z,y) (0,-z,-y) (0,-z,y) (z,y,0) (z,-y,0) (-z,y,0) (-z,-y,0)
48	i	m.m 2	(1/2,y,y) (1/2,-y,y) (1/2,y,-y) (1/2,-y,-y) (y,1/2,y) (y,1/2,-y) (-y,1/2,y) (-y,1/2,-y) (y,y,1/2) (-y,y,1/2) (y,-y,1/2) (-y,-y,1/2)
48	h	m.m 2	(0,y,y) (0,-y,y) (0,y,-y) (0,-y,-y) (y,0,y) (y,0,-y) (-y,0,y) (-y,0,-y) (y,y,0) (-y,y,0) (y,-y,0) (-y,-y,0)
48	g	2.m m	(x,1/4,1/4) (-x,3/4,1/4) (1/4,x,1/4) (1/4,-x,3/4) (1/4,1/4,x) (3/4,1/4,-x) (1/4,x,3/4) (3/4,-x,3/4) (x,1/4,3/4) (-x,1/4,1/4) (1/4,1/4,-x) (1/4,3/4,x)
32	f	.3m	(x,x,x) (-x,-x,x) (-x,x,-x) (x,-x,-x) (x,x,-x) (-x,-x,-x) (x,-x,x) (-x,x,x)
24	e	4m. m	(x,0,0) (-x,0,0) (0,x,0) (0,-x,0) (0,0,x) (0,0,-x)
24	d	m.m m	(0,1/4,1/4) (0,3/4,1/4) (1/4,0,1/4) (1/4,0,3/4) (1/4,1/4,0) (3/4,1/4,0)
8	c	-43m	(1/4,1/4,1/4) (1/4,1/4,3/4)
4	b	m-3m	(1/2,1/2,1/2)
4	a	m-3m	(0,0,0)

MnHCF + 10% Ni PXRD data refinement:

Acquisition time 1s/step.

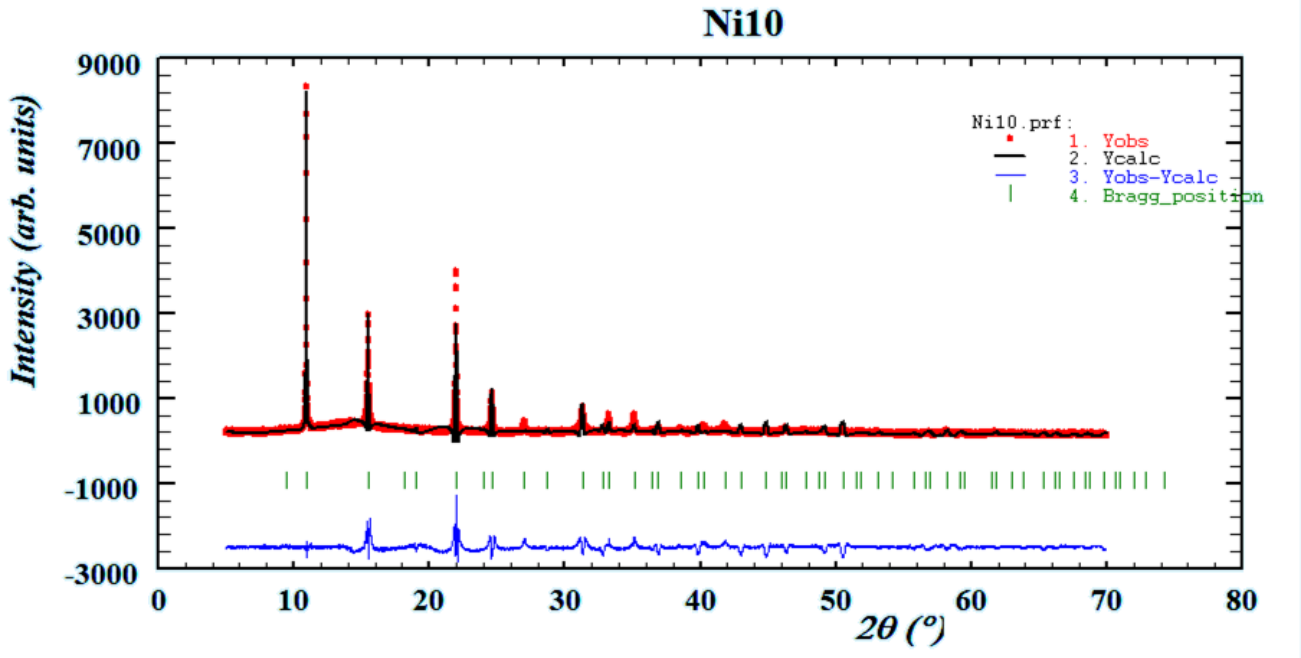

Acquisition time 3s/step.

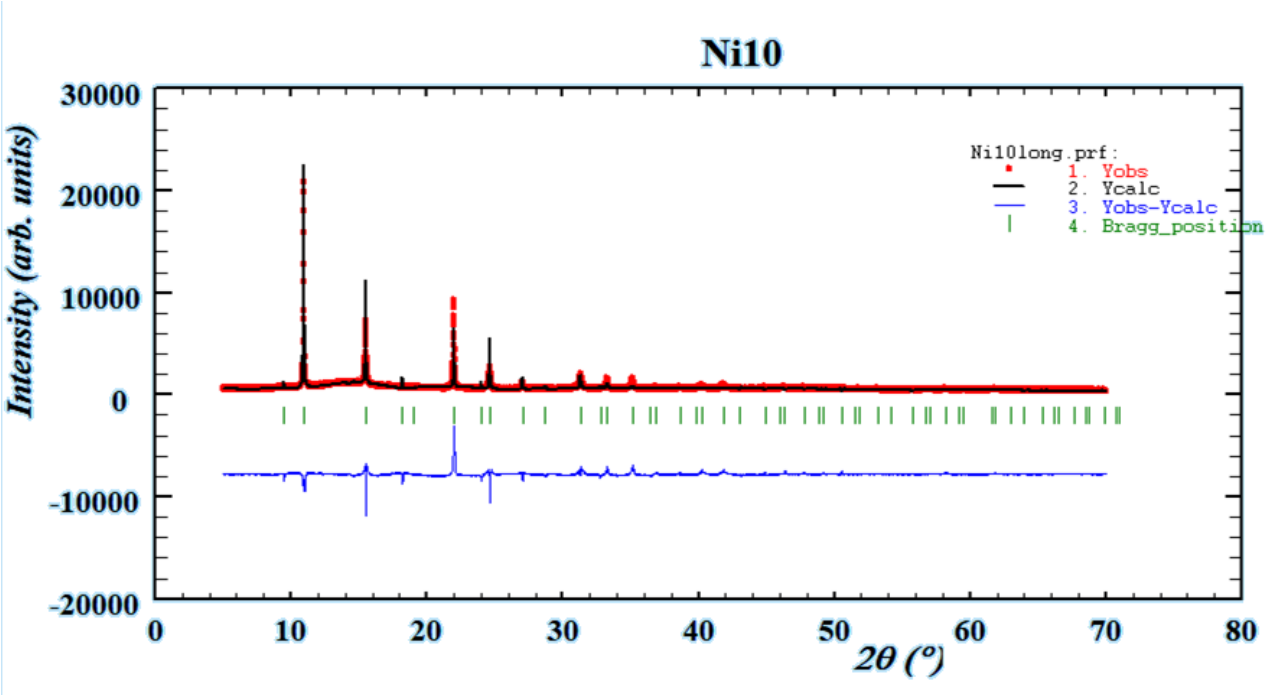

MnHCF + 30% Ni PXRD data refinement:

Acquisition time 1s/step.

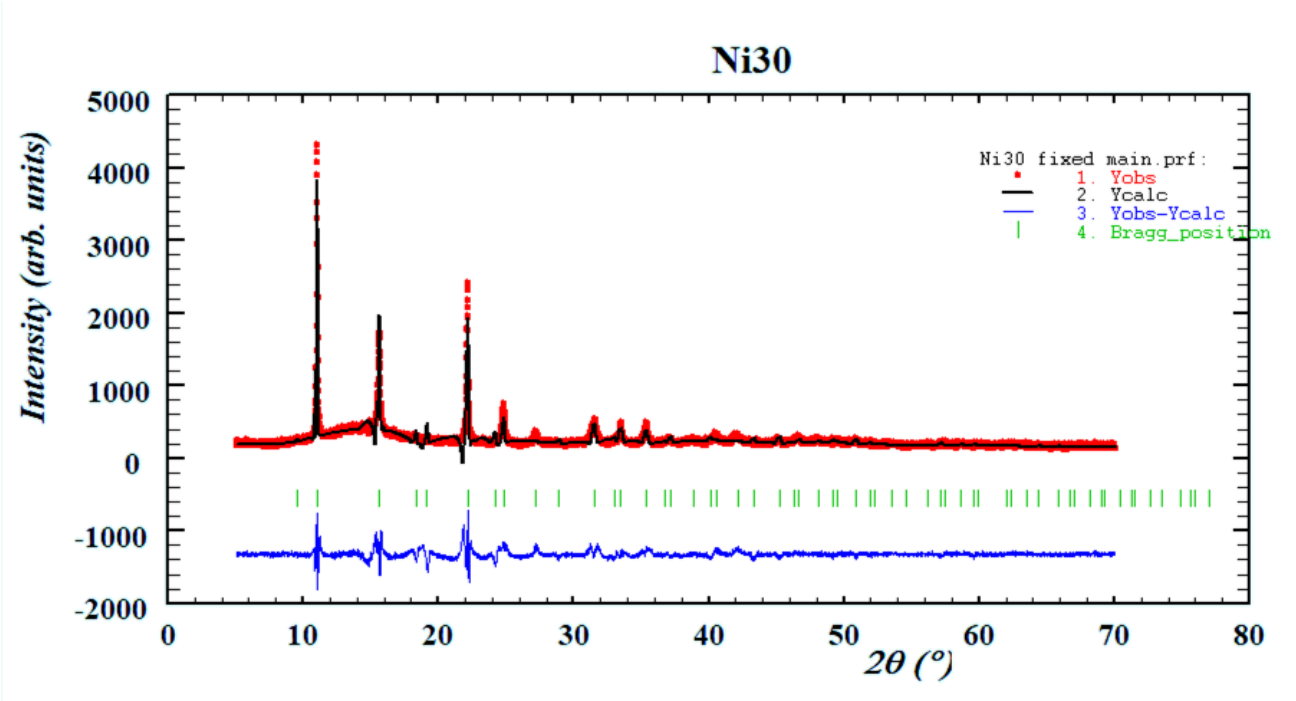

Acquisition time 3s/step.

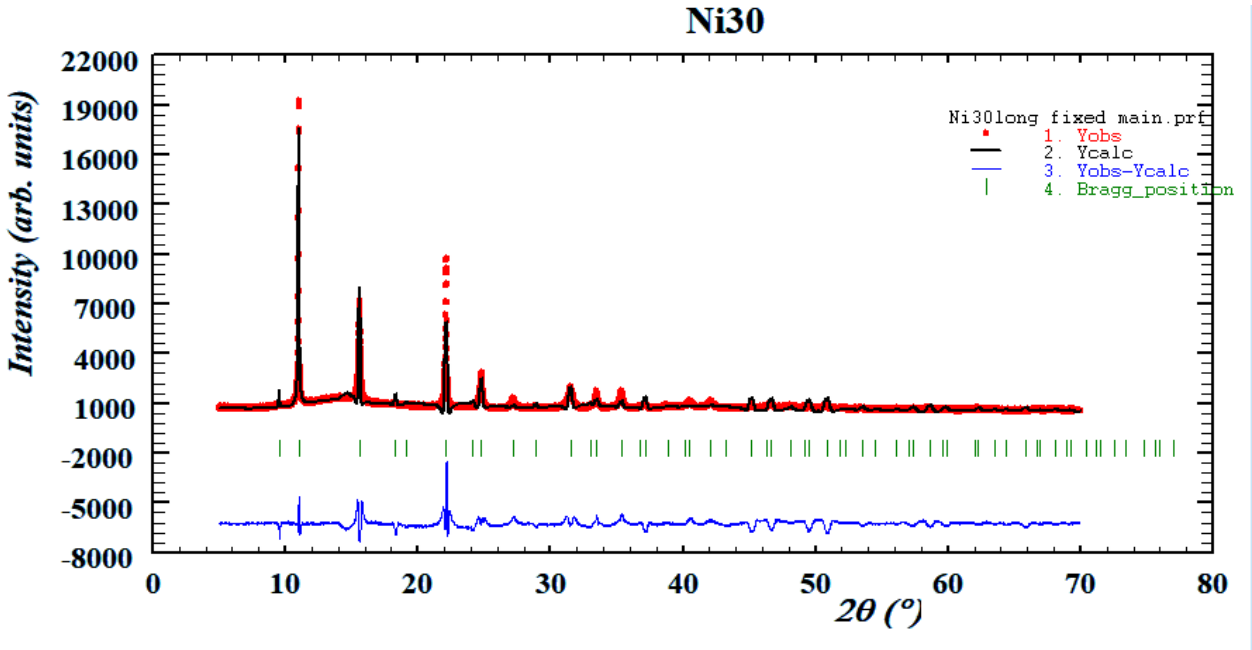

MnHCF + 10% Ni structure obtained from FPStudio (FullProf Suite):

Acquisition time 1s/step (left) and 3s/step (right)

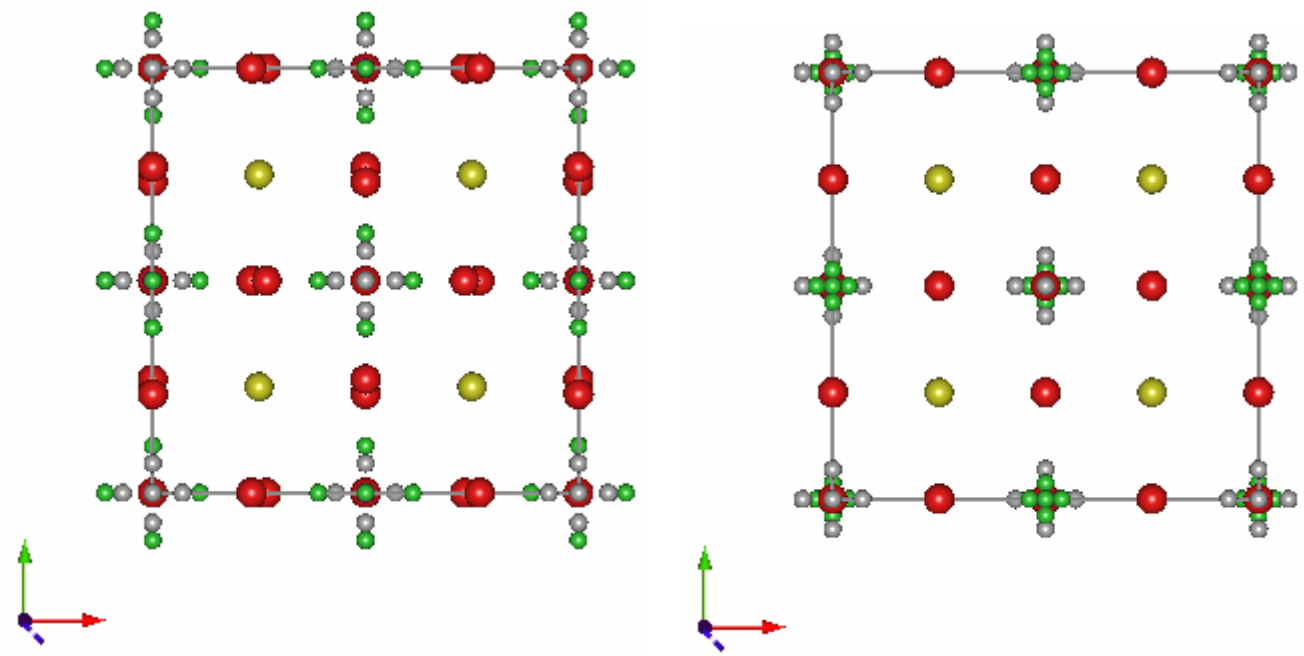

MnHCF structure obtained from FPStudio (FullProf Suite):

Acquisition time 1s/step (left) and 3s/step (right)

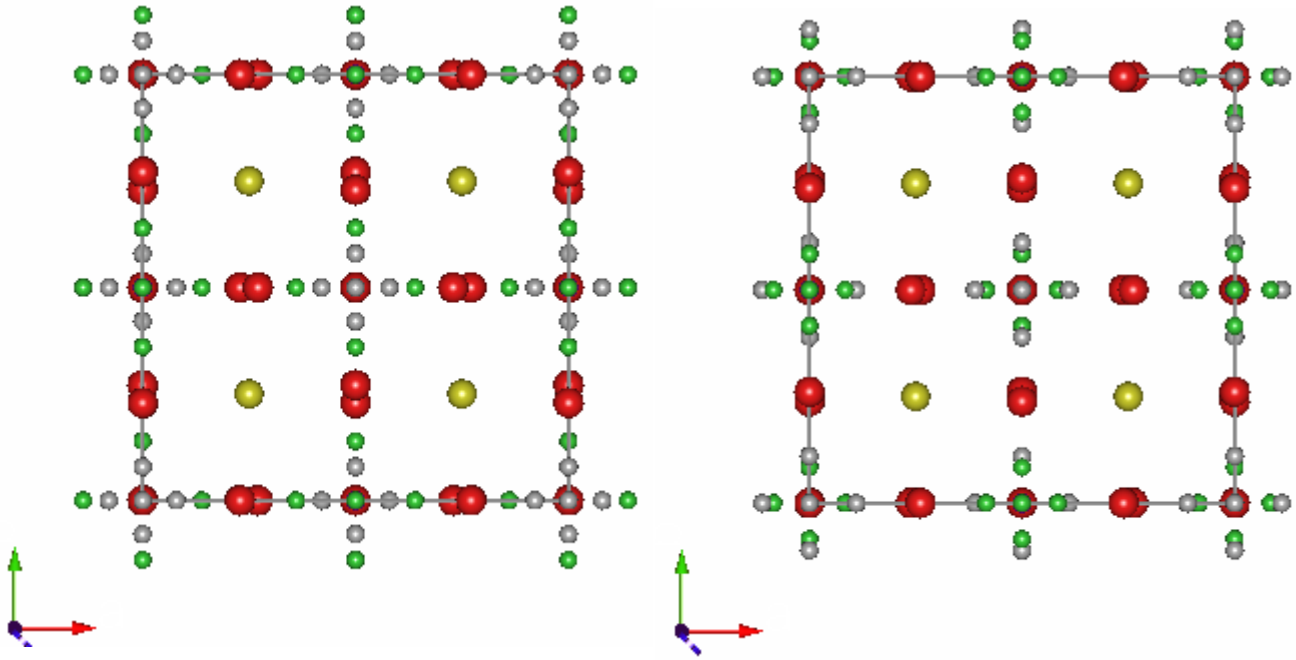

Indexing MnHCF:

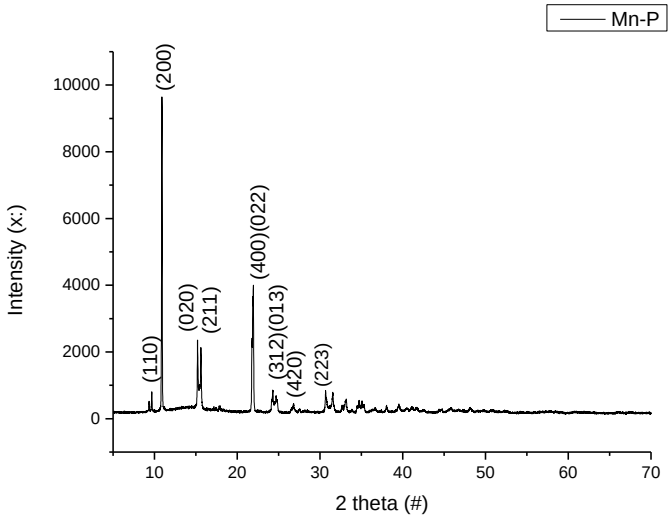

Indexing MnHCF+Ni 10%

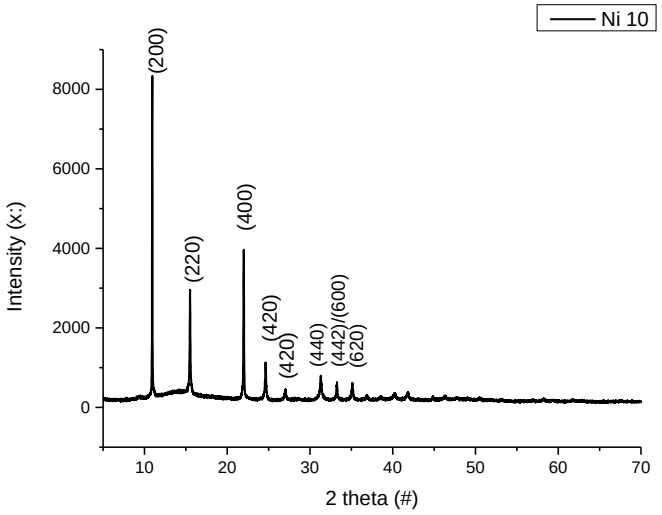

Indexing MnHCF+Ni 30%

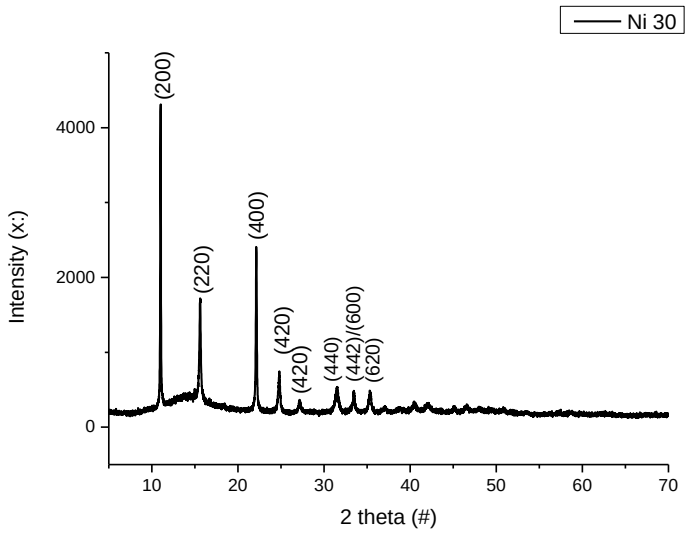

Appendix 2: Extended X-ray Absorption Fine Structure

The χ^2-extracted experimental EXAFS signal pure MnHCF of Fe and Mn and the comparison to the theoretical model:

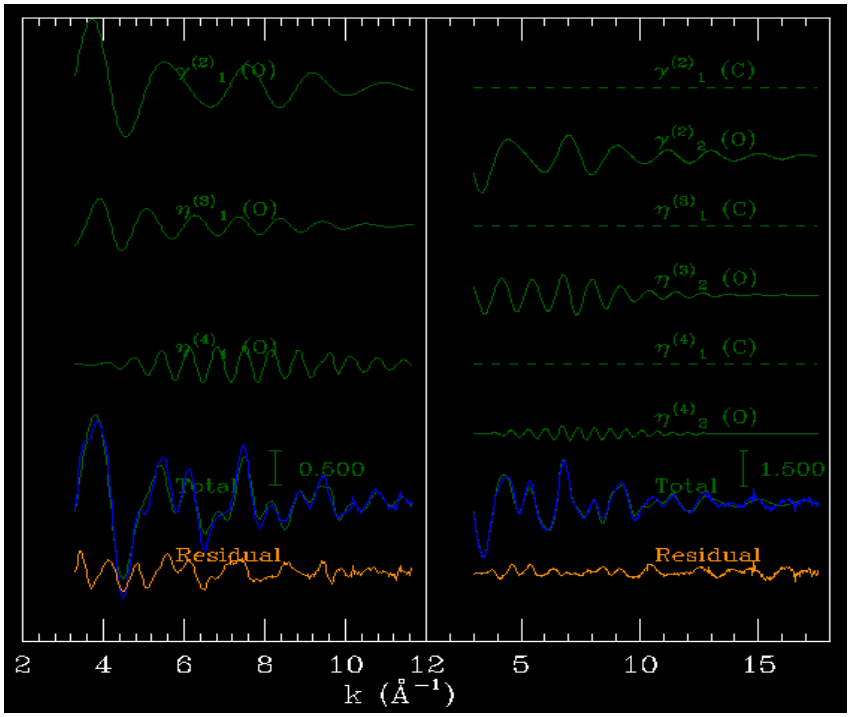

The χ^2-extracted experimental EXAFS signal MnHCF +Ni 10% of Fe and Mn and the comparison to the theoretical model:

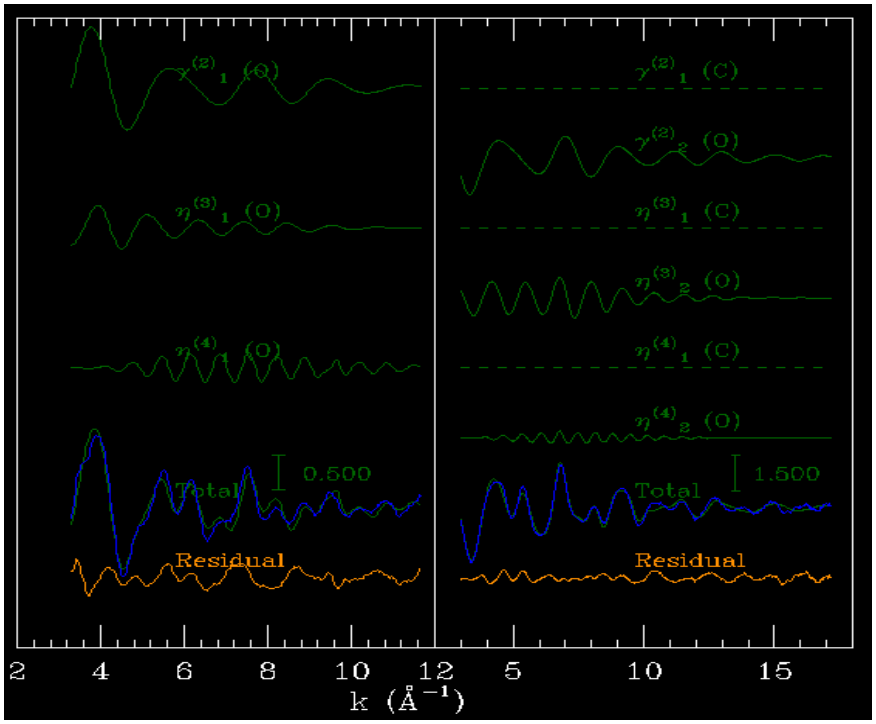

The χ^2-extracted experimental EXAFS signal MnHCF +Ni 10% of Fe and Mn and the comparison to the theoretical model:

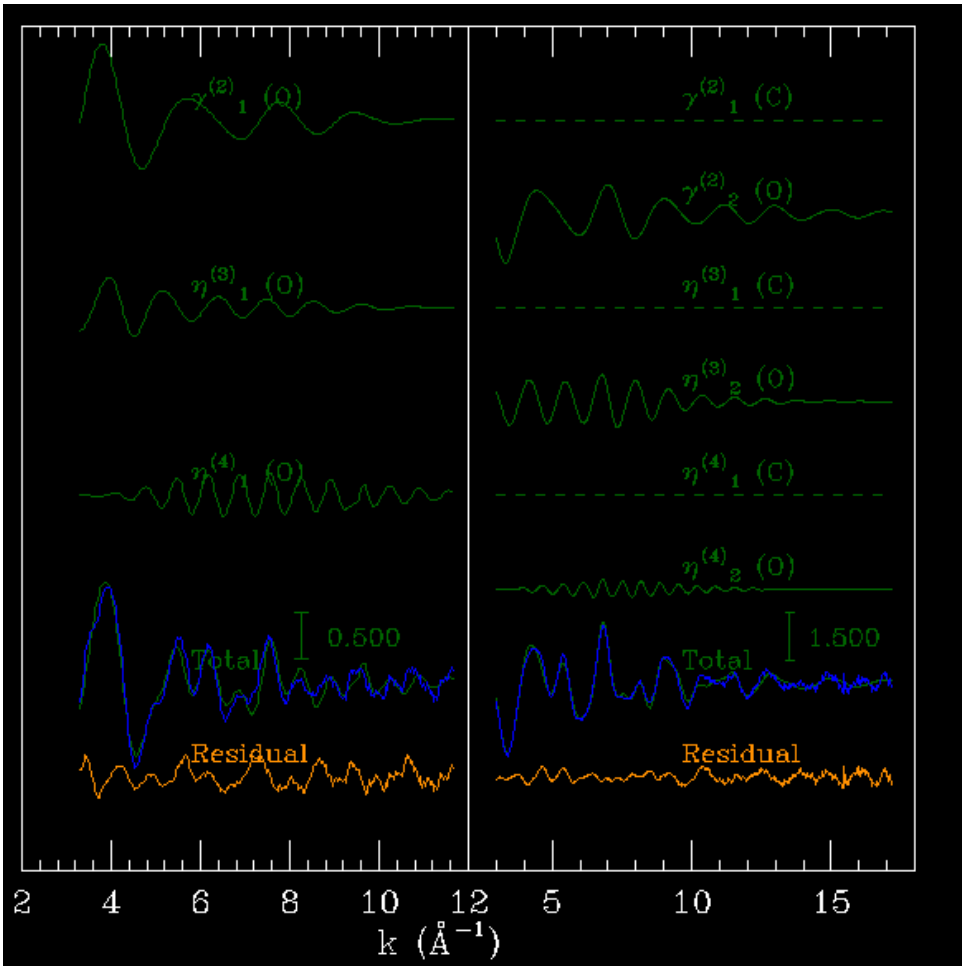

Appendix 3: Transmission X-ray microscopy

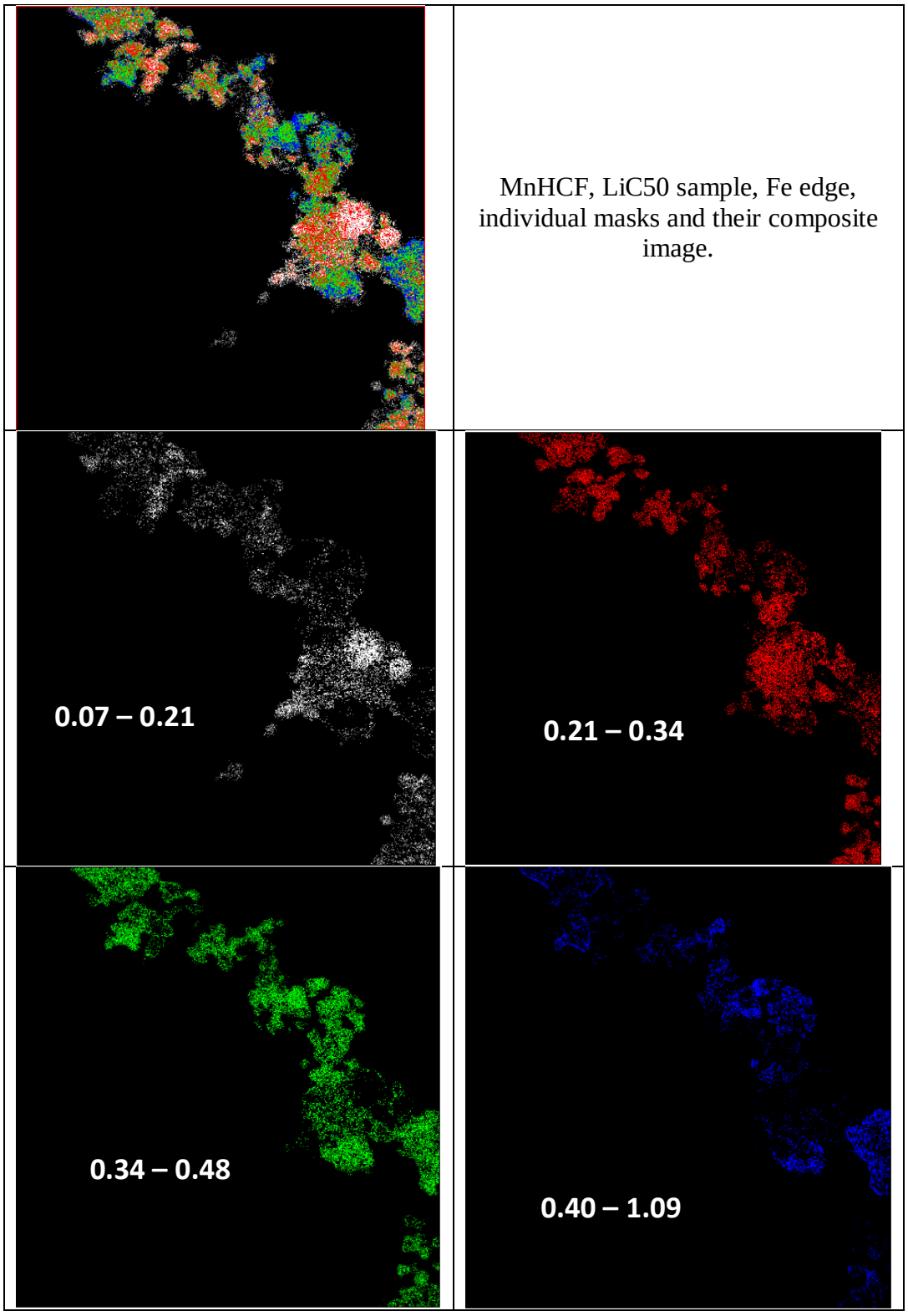

MnHCF, LiC50 sample, Fe edge, individual masks and their composite image.

.t

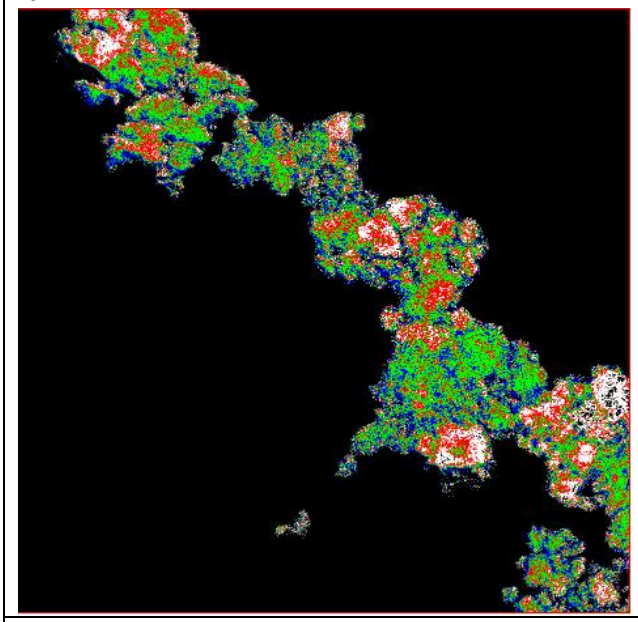

MnHCF, LiC50 sample, Mn edge, individual masks and their composite image.

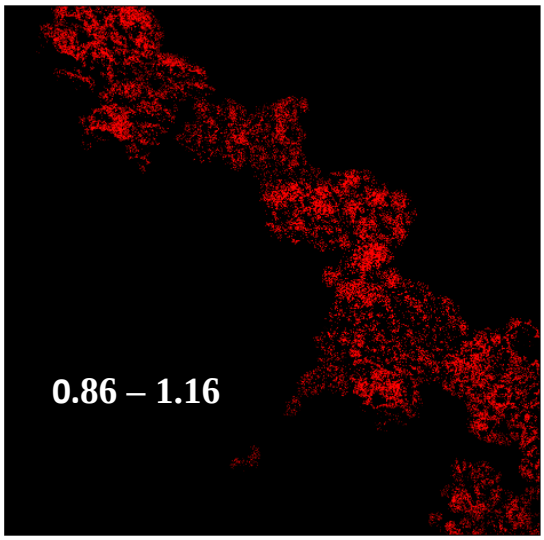

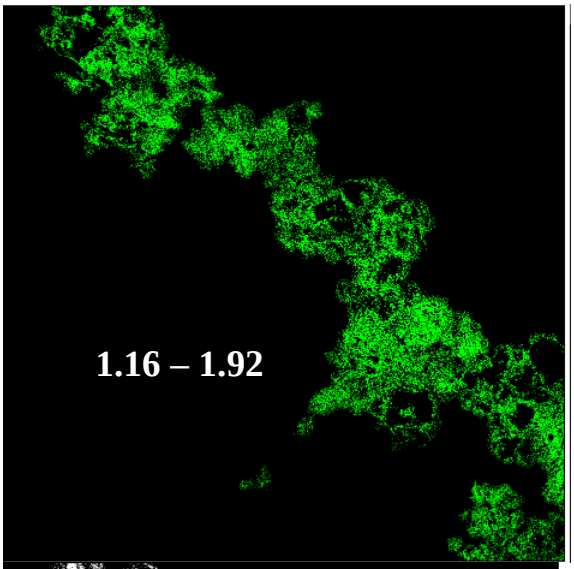

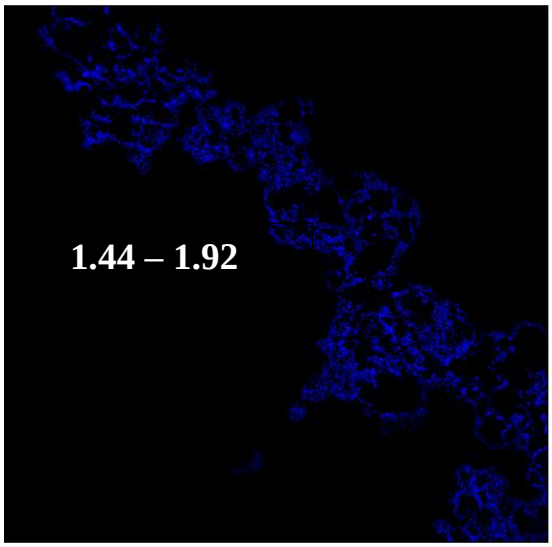

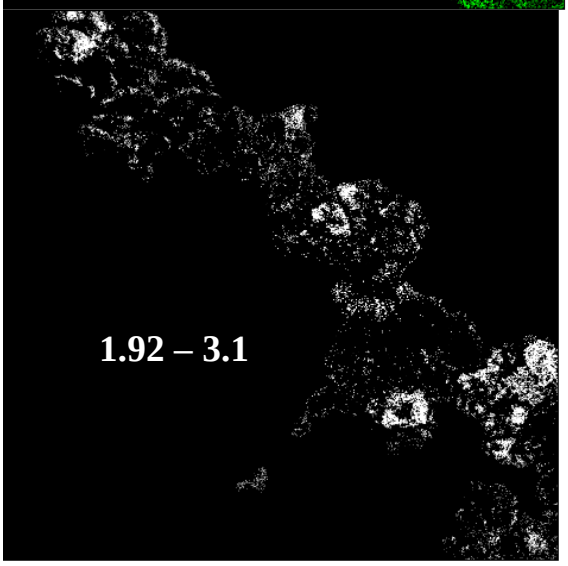

MnHCF, LiC50 sample. N edge individual masks and their composite image.

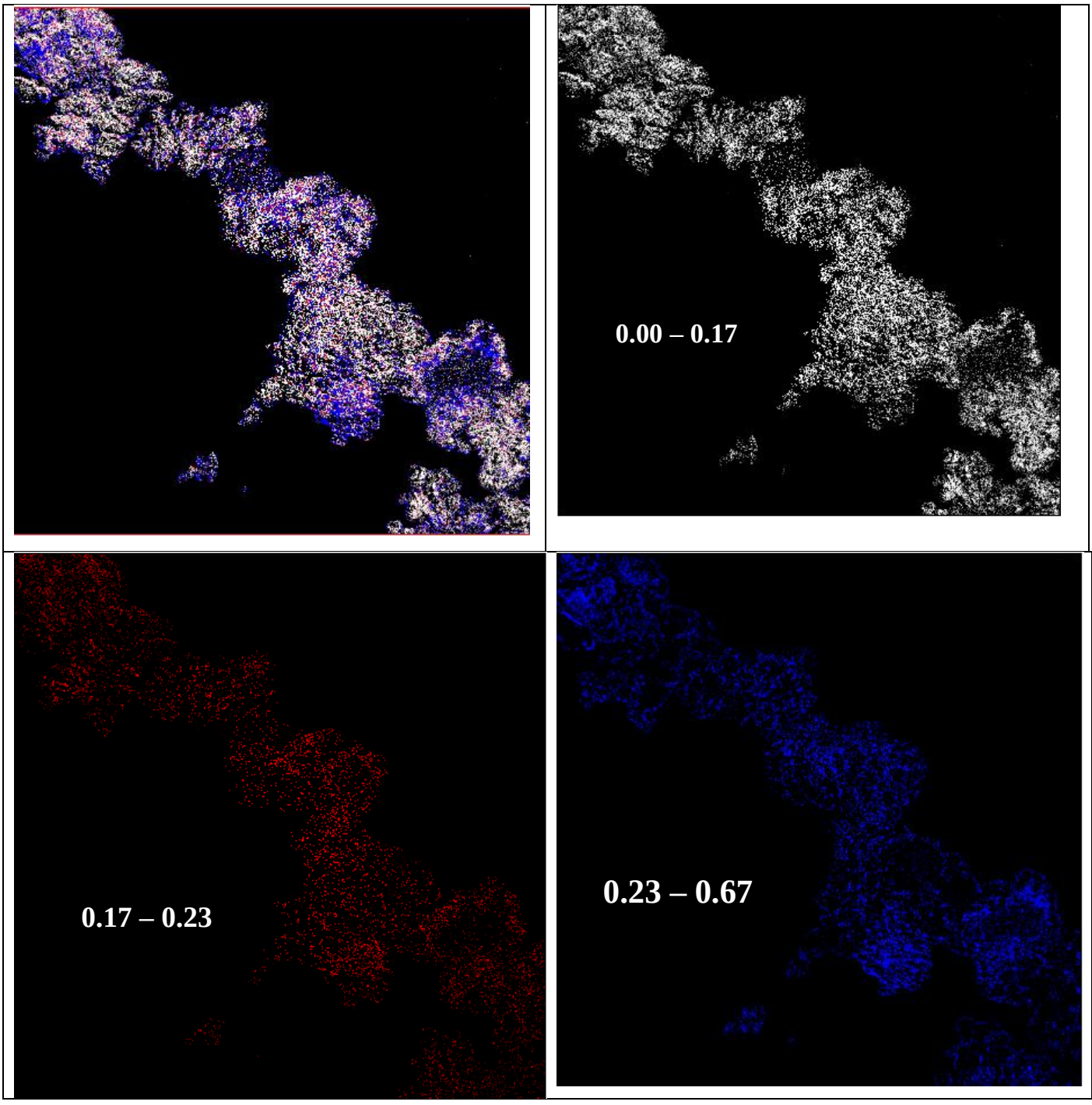

Acknowledgments

First of all. I want to thank the University of Bologna and the Erasmus Mundus joint master degree programme Advanced Spectroscopy in Chemistry (ASC) with all its consortium members, especially University of Lille and University of Leipzig, where I spent my first year of master, for giving me the unique opportunity of studying in several top universities.

I also want to thank my supervisor, Professor Marco Giorgetti, for allowing me to work in his research group, for his patience and encouragements. I am especially grateful, for his flexibility about my master thesis during the situation with COVID-19. He made sure my work was interesting for me and gave me the opportunity to still work with different techniques. I am grateful for his support with not only my current carrier but with my future plans in science.

Additionally, I want to thank Dr. Dino Tonti, for working with me during more than two months online, for his suggestions and explanations.

I am especially grateful to Min Li, who was ready to help me with every small problem I had during this year. For her care and interest towards my work.

I deeply value the experience I had with my fellow ASC student, colleague in the laboratory and my roommate Anastassyia Khan, with whom I spent most of my time, especially during the quarantine. I want to thank her for her support, advices and discussions during my second year of master and my thesis work and mainly for her friendship.

At last, I want to thank all the people who influenced my path in science, my bachelor supervisor and my colleagues and friends from baccalaureate and of course to my family for their trust in me, for their support and encouragements.

Mariam Maisuradze

07/2020